

UNCLASSIFIED

AD NUMBER

AD882535

LIMITATION CHANGES

TO:

Approved for public release; distribution is unlimited.

FROM:

Distribution authorized to U.S. Gov't. agencies and their contractors; Critical Technology; JAN 1971. Other requests shall be referred to Air Force Materials Laboratory, Attn: AFML/LN, Wright-Patterson AFB, OH 45433. This document contains export-controlled technical data.

AUTHORITY

AFML ltr, 7 Dec 1972

THIS PAGE IS UNCLASSIFIED

882535

AFML - TR - 66 - 310
PART V
VOLUME II

20

93

INTEGRATED RESEARCH ON CARBON COMPOSITE MATERIALS

VOLUME II
STRUCTURAL MECHANICS

DDC
RECEIVED
APR 19 1971
A

AD NO. _____
DDC FILE COPY

UNION CARBIDE CORPORATION
CARBON PRODUCTS DIVISION
- IN ASSOCIATION WITH -
CASE WESTERN RESERVE UNIVERSITY
BELL AEROSPACE COMPANY, DIVISION OF TEXTRON

Cleveland Ohio

PROGRAM SUPERVISORS

H.F. VOLK
H.R. NARA
D.P. HANLEY

TECHNICAL REPORT AFML - TR - 66 - 310, PART V, VOLUME II

JANUARY 1971

AIR FORCE MATERIALS LABORATORY
AIR FORCE SYSTEMS COMMAND
WRIGHT - PATTERSON AIR FORCE BASE, OHIO

THIS DOCUMENT IS SUBJECT TO SPECIAL EXPORT CONTROLS AND EACH TRANSMITTAL TO FOREIGN GOVERNMENTS OR FOREIGN NATIONALS MAY BE MADE ONLY WITH PRIOR APPROVAL OF THE NONMETALLIC MATERIALS DIVISION, AFML/LN, AIR FORCE MATERIALS LABORATORY, WRIGHT - PATTERSON AIR FORCE BASE, OHIO 45433

154

**BEST
AVAILABLE COPY**

NOTICES

When Government drawings, specifications, or other data are used for any purpose other than in connection with a definitely related Government procurement operation, the United States Government thereby incurs no responsibility nor any obligation whatsoever; and the fact that the Government may have formulated, furnished, or in any way supplied the said drawings, specifications or other data, is not to be regarded by implication or otherwise as in any manner licensing the holder or any other person or corporation, or conveying any rights or permission to manufacture, use, or sell any patented invention that may in any way be related thereto.

This document is subject to special export controls and each transmittal to foreign Governments or foreign Nationals may be made only with prior approval of the Nonmetallic Materials Division, AFML/LN, Air Force Materials Laboratory, Wright-Patterson Air Force Base, Ohio 45433.

ACCESSION NO.			
CRPT	WHITE SECTION <input checked="" type="checkbox"/>		
DOC	DIFF. SECTION <input type="checkbox"/>		
ORAN.	SEC.		
JUSTIFICATION			
BY			
DISTRIBUTION AVAILABILITY CODES			
DISC.	ATL.	INT'L	RESER.
2			

Copies of this report should not be returned unless return is required by security considerations, contractual obligations or notice on a specific document.

**INTEGRATED RESEARCH ON
CARBON COMPOSITE MATERIALS**

Summary Technical Report

AFML-TR-66-310, Part V

Volume II

Structural Mechanics

Program Supervisors

H. F. Volk

H. R. Nara

D. P. Hanley

January 1971

This document is subject to special export controls and each transmittal to foreign Governments or foreign Nationals may be made only with prior approval of the Nonmetallic Materials Division, AFML/LN, Air Force Materials Laboratory, Wright-Patterson Air Force Base, Ohio 45433.

Distribution of this report is limited for the protection of technology related to critical materials restricted by the Export Control Act.

FOREWORD

The work reported herein was performed under the sponsorship of the Advanced Research Projects Agency, Department of Defense through Contract F33615-68-C-1077, ARPA Order No. 719, Program Code 7D10, with the Air Force Materials Laboratory, LN, Wright-Patterson Air Force Base, Ohio. Mr. H. S. Schwartz is the Air Force Program Manager.

This work is a continuation of the effort under Contract AF 33(615)-3110 which had covered the period 17 May 1965 to 17 June 1969, and which was reported in Parts I through IV of this series.

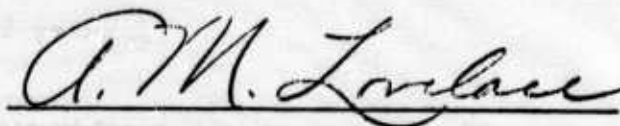
The prime contractor is Union Carbide Corporation, Carbon Products Division with Dr. H. F. Volk (Phone 216-433-8600) as program supervisor. The subcontractors are the Case Western Reserve University with Dr. H. R. Nara (Phone 216-368-4192) as program supervisor and Prof. T. P. Kicher as associate program supervisor and Bell Aerospace Company, a Division of Textron, with Mr. D. P. Hanley (Phone 716-297-1000) as program supervisor.

This is Part V of the report and covers work performed from July 1969 to September 1970. Part V is issued in three volumes. Volume I covers materials research; Volume II, structural mechanics; and Volume III, structural component development.

The authors wish to acknowledge the assistance of Mr. D. C. Watson and Mr. M. Knight of the Air Force Materials Laboratory, who conducted the stressing tests on the specimens used for studying the effect of sustained load on microcracks.

This report was submitted by the authors in January 1971.

This technical report has been reviewed and is approved.



A. M. LOVELACE
Director
Air Force Materials Laboratory

ABSTRACT

The work presented in Volume II is concerned with the structural mechanics and synthesis of graphite-fiber reinforced composite materials. Optimization studies (minimum weight design) of stiffened cylinders similar to the fuselage component were carried out by two different techniques. The behavior of composite structural elements was investigated in plate-buckling and post-buckling studies, buckling of stiffened plates with cutouts, and application of shell theory to anisotropic cylinders. Micromechanics studies of fibrous composites included development of a photoelastic technique for analyzing frozen stresses, a discrete element microstress analysis of unidirectional fiber composites, an application of the theory of physically nonlinear elastic solids to composite materials, and an investigation of the multiple circular inclusion problem in plane elastostatics. Failure of composite structural elements was investigated through studies of the failure mechanism for off-axis composites, the fracture toughness of composites, the effect of fatigue and sustained loads of cross-plyed composites, the notch sensitivity of cross-plyed composites, and the effect of a variety of known intentionally interjected defects on the fracture strength. Further studies were concerned with multiaxial stress testing of composite cylinders. The effects of circular and square cutouts in flat panels and in a stiffened panel, and methods of reinforcement of cutouts were investigated and correlated with predictions based on discrete element analysis.

BLANK PAGE

TABLE OF CONTENTS

<u>Section</u>		<u>Page</u>
I.	INTRODUCTION.	1
II.	SUMMARY	3
III.	COMPOSITE SYNTHESIS.	7
	A. Stiffened Cylinder Optimization (Case)	7
	B. Minimum Weight Design of Composite Structures (Bell)	11
IV.	BEHAVIOR OF COMPOSITE STRUCTURAL ELEMENTS (Case)	22
	A. Post-Buckling of Anisotropic Plates under Axial Compression	22
	B. Post-Buckling Strength of Composite Plates	22
	C. Buckling of Laminated Composite Plates with Cutouts	33
	D. Accuracy Study of Shell Theories for Anisotropic Cylinders.	34
V.	MICROMECHANICS OF FIBER COMPOSITES (Case)	38
	A. Three Dimensional Photoelastic Models of Filamentary Composite Materials	38
	B. Scattered Light Photoelasticity and Holography.	49
	C. Discrete Element Microstress Analysis of Unidirectional Fiber Composites	58
	D. Application of Theory of Physically Nonlinear Elastic Solids to Composite Materials.	59
	E. Multiple Circular Inclusion Problem in Plane Elastostatics	66
	F. Structural Analysis for Laminated Fiber Composite Structures	68
	G. Three-Dimensional Finite Element Analysis-Mixed Stress-Displacement Approach.	71

TABLE OF CONTENTS (CONT'D.)

<u>Section</u>	<u>Page</u>
VI. FAILURE OF COMPOSITE STRUCTURAL ELEMENTS . .	82
A. Interfiber Failure of Composite Materials (Case) . .	82
B. Fracture Toughness of Fiber Composites (Case) . .	82
C. Time Dependent Properties of Fiber Composites . .	95
D. Notch Sensitivity of Fiber Composites	103
E. Influence of Defects on Composite Properties . . .	105
F. Fracture Strength of Composite Cylinders under Combined Stresses	107
VII. REINFORCED CUTOUTS IN COMPOSITE STRUCTURES .	116
A. Objective and Approach	116
B. Fabrication	116
C. Test Results	123
D. Test-Theory Comparisons	135
REFERENCES	138

LIST OF ILLUSTRATIONS

<u>Figure</u>		<u>Page</u>
1	Integrally Stiffened Cylinder with Hat Cross-Section Stiffeners	9
2	Two-Dimensional "Beam" Problem.	12
3	Initial and Optimized Designs	12
4	Original Flat Panel Section	15
5	Stiffened Panel Geometry and Idealization.	15
6	Cylinder Cross-Section	17
7	Detail of Single Skin - Stringer.	20
8	Load-Deflection Curve for (0, 90, 90, 0) "Thornel" 25 Plate Simply Supported and with Unloaded Edges Free to Expand . .	23
9	Effective Width vs. Shortening Curve (0, 90, 90, 0) "Thornel" 25 Plate	24
10	Load Shortening Curve for (0, 90, 90, 0) "Thornel" 25 Plate . .	25
11	Post-buckling Load Distribution	30
12	Post-buckling Analysis Model	30
13	Radial Pressure and Torsion Interaction Curve	37
14	Model Type 1 1/2" Thick	40
15	Model Type 2 1/4" Thick Full Scale	41
16	Preliminary S. F. Test Model Sketches	42
17	Load Test No. 1 Model Sketches	43
18	Thermal Stresses Near a Fiber End in a Dark Field. (1.25 Fringe)	44
19	Thermal Stresses Near a Fiber End in a Light Field. (1.25 Fringes)	45
20	Thermal and Mechanical Stresses Near a Fiber End in a Dark Field. (6.0 Fringes)	46

LIST OF ILLUSTRATIONS (Cont'd)

<u>Figure</u>		<u>Page</u>
21	Thermal and Mechanical Stresses Near a Fiber End in a Light Field. (6.0 Fringes)	47
22	Model Configuration and Load Application.	50
23	Dark Field View of Model Slices.	51
24	Normalized Effective Stress.	52
25	Scattered Light Fringes for Disks of Polyester and Epoxy Under Diametral Compression.	55
26	Homogeneous Unbounded Matrix Containing Circular Inclusion	60
27	Regular Array of Circular Fibers	64
28	Beam Test Case for the Finite Element Analysis	69
29	In Plane Displacement Through Thickness	70
30	Fixed End Prismatic Bar Stretched Under an Axial Load	79
31	Prismatic Bar Divided into Four Finite Elements	81
32	Photo of Fracture Toughness Apparatus	84
33	Photo of Fractured Specimen	85
34	Load-Displacement Record for Specimen 0-1210-E	87
35	Stress in Field vs. Crack Depth Ratio	88
36	Nominal Stress vs. Crack Depth Ratio	89
37	Stress Intensity Factor vs. Crack Depth Ratio.	90
38	Stress Intensity Factor vs. Specimen Width.	91
39	Stress Intensity Factor vs. Crosshead Speed	92
40	Stress Intensity Factor vs. Ply Angle	94
41	Cracks in an "As Fabricated" "Thornel" 50 Plate	95

LIST OF ILLUSTRATIONS (Cont'd)

<u>Figure</u>		<u>Page</u>
42	Cracks in Plate No. 4 Due to One Cycle Stress of 93 Percent UTS	99
43	Crack Density Produced by Various Strain-Time Conditions	100
44	Microstructure of Plate PS-08270	104
45	Combined Stress Test Specimen Assembly	108
46	Fracture Strength Surface for Four-Ply (90°, 0°, 0°, 90°) "Thornel" 50S/ERLB 4617 Composite	109
47	Microphotograph of Pure Torsion Test Cylinder (08100-1), Tangential View. (50X Magnification)	112
48	Microphotograph of Pure Torsion Test Cylinder (08120-1), Longitudinal View. (50X Magnification)	112
49	Microphotograph of Combined Stress Test Cylinder (08260-2), Tangential View. (50X Magnification)	113
50	Microphotograph of 14(0°) Unidirectional Plate (T50S-09100-1). (30X Magnification).	113
51	Fractured Cylindrical Specimens Subjected to Pure Torsion and to Combined Stresses	115
52	Control and Unreinforced Cutout Test Panels	121
53	Externally Bonded Steel Reinforced Cutout Panel	122
54	Reinforced Cutout Panels	124
55	Stiffened Compression Panel with Reinforced Square Cutout.	125
56	Cutout Panels after Test	126
57	Reinforced Cutout Panels after Test	127
58	Typical Strain Responses from Cutout Panel Test	132
59	Comparison of Failure Loads and Reinforcement Weights for "Thornel" 50S/4617 Specimens.	133
60	Typical Edge Delamination	134
61	Normalized Strain ϵ_x/ϵ_n vs. y/a for Unreinforced Cutout Panel.	136
62	Normalized Tangential Stress and Strain vs. Angle at $r=a$	137

LIST OF TABLES

<u>Table</u>		<u>Page</u>
I	Isotropic Beam-Plate Optimization	13
II	Stresses From Bending Theory.	18-19
III	Properties of Photoelastic Matrix Materials	39
IV	Test Results on Various Compatibility Models	39
V	Possible Model Material.	53
VI	Photoelastic Calibration Constants	54
VII	Composition of Epoxy Samples	56
VIII	Composition of Polyester Samples	56
IX	Physical Properties of Plates and Constituents	96
X	Cracking Due to Single Cycle Stress.	98
XI	Cracking Due to Fatigue Cycling at Constant Stress.	101
XII	Modulus and Strength of Fatigued Specimens	101
XIII	Composite Notch Sensitivity	105
XIV	Effect of Known Defect on Composite Strength	106
XV	Combined Stress Test Data on "Thornel" 50S/ERLB 4617 Cylindrical Specimens.	110
XVI	Uniaxial Stress Test Data on "Thornel" 50S/ERLB 4617 Plates.	110
XVII	Test Results of "Thornel" 50S Unidirectional Laminates.	118
XVIII	Bleeder System Investigation.	119
XIX	Comparison of Failure Loads (lb/in.)	128
XX	Control Panel Test Results "Thornel" 50S/4617, (±15, 90, ±15)	129
XXI	Predicted "Thornel" 50S/4617 Properties	131
XXII	Predicted and Measured "Thornel" 50S/4617 Unidirectional Properties	131

SECTION I

INTRODUCTION

The present program is a continuation of the work performed under Contract AF 33(615)-3110 (see References 1 through 6). This report covers the fifth (and final) year's work of a program which represented a novel approach designed to fulfill three different, but clearly interdependent, needs of the Department of Defense: a materials need, a structural design capability need, and a need for more scientists and engineers trained in applied materials problems and advanced design methods. The Carbon Products Division of Union Carbide Corporation, Case Western Reserve University, and Bell Aerospace Company have formed an Association to meet these needs.

The Association has formulated a broad program which includes the development of new materials, generation of advanced analyses and design methods, and education of graduate students. In brief, the major objectives are (1) to develop high modulus graphite fiber composites, (2) to extend the methods of structural mechanics, (3) to identify DOD applications toward which the program efforts should be directed, (4) to educate engineers capable of developing and using modern materials, and (5) to integrate materials research with the needs of the design by extending the technique of structural synthesis to include material variables.

The primary responsibilities of Union Carbide Corporation, Carbon Products Division, are the development and production of composite materials and the measurement of those mechanical and thermal properties needed for the structural design work within the Association. The technical program at Union Carbide consists of: (1) materials research, a basic research program to develop new, improved composites of high modulus graphite fibers in both resin and metal matrices; (2) materials fabrication, an applied research program to produce materials for the joint research programs of the Association and to seek new ways of fabricating components which better utilize the superior properties of composite materials; (3) properties evaluation, the measurement of the mechanical and thermal properties of certain composites to provide data for the joint research programs of the Association; and (4) failure criteria, a basic research program to determine experimentally adequate failure criteria for anisotropic materials under multiaxial stress states and to find ways of representing the failure surface which can be used by the designer in practical calculation.

The work at Case Western Reserve University has two major objectives. The first objective is to advance the basic structural mechanics technology required for rational design with composite materials. Composite materials offer the structural design engineer the prospect of being able ultimately to carry on simultaneously the design of the structural configuration and the material. Achieving this capability will require fundamental advances in structural synthesis as well as a substantially improved understanding of the behavior of composite materials. The goals of the structural mechanics

research program at Case are (1) the quantitative formulation and efficient solution of the structural synthesis problem, including material variables, for elementary, but representative components fabricated from composite materials; (2) experimental stress analysis studies and theoretical investigations in micromechanics with the objective of improving the measurement and calculation of stiffness properties and failure mode criteria for composite materials; and (3) the development of improved analysis methods for anisotropic, nonlinear, and nonconservative materials. The second objective of the work at Case Western Reserve University is to develop new or improved graphite fiber-resin composites through materials research. At present, the knowledge of fiber surface morphology and the relation between fiber surface characteristics and interfacial adhesion to the resin system(s) is incomplete. A better understanding of these interfacial interactions will lead to improvements in presently used fiber-resin composites and will ultimately permit the judicious selection of new resins and new fabrication methods, thus leading to a second generation of advanced composites.

The primary purposes of Bell Aerospace Company's participation in this program are to interject user requirements into the applied materials research efforts; to apply at the prototype design level, the advanced analytical procedures and improved understanding of material behavior which will result from the research; and to establish application-related property specifications for materials research activities. To attain these objectives, a six-part technical program is being performed by Bell: (1) application selection, the objective of which is to define representative configurations and environmental conditions which reflect DOD requirements; (2) recognition of failure modes, a task which involves the overall structural behavior such as elastic instability, deformation limits, and fracture and the material failure modes; (3) determination of the nature of and methods for the application of analytical tools needed to cope with the anisotropic, anelastic, and nonconservative material property behavior and the multiaxial stress distributions anticipated in structural configuration associated with the use of the subject materials; (4) structural synthesis, a task which involves the application of structural synthesis techniques at the practical level to define the most desirable material compositions within a particular class of composites; (5) study of creative design concepts which will be required because of the complex material behavior of composites; (6) testing to verify the value of analysis procedures used to design composite materials and the components made from composite materials.

Although this report of the Association's fifth year activities is the last report of the Association, the Case Western Reserve University will be continuing research on composite materials during the sixth year under sponsorship of the Advanced Research Projects Agency.

This report is divided into three volumes. Volume I covers the effort on materials research; Volume II covers the work on structural mechanics, analysis, and optimization; and Volume III covers the testing, stress analysis, and evaluation of a representative subscale fuselage component. This division was made because particular projects might be of interest to a particular audience; this arrangement also made possible the reduction of the physical size of each volume. However, the following Summary (Section II) also contains a brief outline of the contents of the other two volumes.

SECTION II

SUMMARY

The technique of structural synthesis, or automated optimum design of structural systems, has been extended to include both geometric and material parameters in the minimum weight design of stiffened fiber composite cylindrical shells. A special computation algorithm was developed for dealing with design parameters such as ply angles which do not explicitly appear in the weight function.

Use of finite element methods of analysis in the optimization of composite structures was found a costly procedure. Because each solution is lengthy and numerous solutions are required during the optimization, this approach becomes prohibitive. An alternate method of analysis based on engineering beam theory should afford a more economical solution.

A Ritz method of solution has been applied to the post-buckling analysis of laminated fiber composite plates. Complete post-buckling response curves were obtained for symmetrically and unsymmetrically laminated plates with either clamped or simply supported boundary conditions. The results are used to define an effective width for the post-buckling strength analysis of high performance composite materials. An experimental program to verify the post-buckling capacity of composite plates was initiated. An experimental study of the effects of cutouts on the buckling loads of laminated plates was initiated but a considerable amount of time was spent on the fabrication of quality specimens. The study of the applicability of various shell theories to anisotropic fiber composite cylinders has been completed. The exact solution for the eigenvalue buckling of anisotropic shells subjected to axial compression, lateral pressure, or gross torsion has been obtained and programmed for the computer.

The development of a suitable photoelastic technique for the analysis of filamentary composites using frozen stresses and transmitted light has been completed. The frozen stress technique was also studied for adaptation to scattered light photoelasticity but the low fringe orders of epoxy matrices necessitated the use of the live-load approach.

A special finite element for the microstress analysis of filamentary composites has been developed, verified on problems with known solutions and applied to a variety of common problems in composite materials for which solutions do not exist. The results of this study are used to obtain stress and strain concentration for use in conjunction with a mechanistic failure theory developed under this program. The general solution for the elastic curvilinear inclusion problem has been found in the case of antiplane or longitudinal shear deformation, and has been utilized for the analysis of randomly spaced fibers in a filamentary composite. Plane deformation of a similar model is currently under investigation. Preliminary results on the validity of classical laminate plate and shell theories when applied to fibrous composites have been obtained.

A failure mechanism for off-axis fiber composites has been postulated based on extensive experimental observation. It was observed that the matrix is in the bulk plastic region early in the loading, consequently failure is hypothesized as a critical creep rate. The state of stress in the matrix is calculated using the concentration factors and the Neuber leading function analysis.

The fracture toughness of unidirectional fiber glass composites has been studied. Its dependence on specimen width, crack depth, and strain rate has been determined experimentally. The dependence of fracture toughness on fiber orientation for crossplied specimens is also being studied.

Crack-free, orthogonal, seven-ply "Thornel" 50S, ERLA 4617 composites were tested under tension-tension fatigue and sustained load conditions. The density of cracks resulting from these tests was determined as a function of load, time-at-load and number of fatigue cycles. These cracks were found to be similar to those frequently developed due to thermal stresses on cooling from the curing or pressing temperature and appeared to have little influence on the modulus or ultimate tensile strength of the composites. Crack density determinations as a function of stress during the first load cycle showed the existence of a threshold for crack creation at a strain of approximately 50 percent of the ultimate tensile strain. Fatigue cycling to 10^5 cycles at a load of 85 percent UTS produced no measurable degradation in tensile strength, yet yielded crack densities higher than those found in samples tested to failure in a single cycle. In sustained load tests, cracking was found to vary nearly linearly with stress in samples loaded for 1000 hours. Samples loaded for shorter times showed that the crack density doubles for each increase by a factor of 10 in time at load. No significant creep occurred during the sustained load tests.

Comparative notch sensitivity studies were carried out on orthogonal, seven-ply "Thornel" 50S, ERLA 4617 epoxy and P-1700 polysulfone composites. Since polysulfone resins are tougher and have much higher elongations to failure than the relatively brittle epoxies, it was expected that the polysulfone composites should be less notch sensitive. The experiments confirmed this expectation.

Tensile, flexural, and compression tests were performed on a number of orthogonal "Thornel" 40, ERL 2256 composites containing intentional defects such as mylar and yarn inclusions and butt or lap joints. Reductions in tensile strength were noted, while the effects on flexural and compressive strength were generally minor.

Fracture strengths under uniaxial, torsional, and combined stresses have been determined for "Thornel" 50S/ERLB 4617/MPDA composite cylinders with a four-ply ($90^\circ, 0^\circ, 0^\circ, 90^\circ$) lay-up pattern. The uniaxial tensile and compressive strengths of the same composite were measured using flat coupon specimens, while shear strength was measured by the torsion bar method. The fracture strengths under combined stresses were measured by subjecting cylindrical specimens to combined loadings of internal pressure, axial force, and torque. These data establish

the approximate shape for the fracture strength envelope of the composite encompassing the shear-tensile-tensile stress state.

Effects of circular and square cut-outs in flat panels and in a stiffened panel assembly were investigated. An unreinforced hole in a multidirectional laminate test specimen was shown to reduce load capability by a factor of two. Integral composite reinforcements around holes in several tensile specimens were found to efficiently carry loads, i. e. , develop the strength of the panel without a hole. The latter specimens were lighter in weight than comparable strength specimens with "bonded on" external reinforcements or integral internal metal reinforcements. Strain responses and ultimate loads compared reasonably well with predictions based on discrete element analysis. A technique of lightweight reinforcement for a cut-out in a stiffened compression panel was successfully demonstrated in test.

Contents of Volume I:

The work presented in Volume I is concerned with materials research on graphite-fiber reinforced composites. Graphite-fiber surfaces were characterized by gas phase and solution adsorption experiments and by Raman spectroscopy. The latter technique allows a differentiation between fibers of different origins and heat-treatment temperatures. The fabrication of "Thornel" fiber, polyamide-imide and polysulfone composites was investigated. Fabrication of polyamide-imide composites was very tedious and evaluation was limited to determinations of torsion shear strength. Several plates of polysulfone matrix composites were fabricated; the evaluation of these plates is presented in Volume II of this report. "Thornel" fiber composites were further prepared by in situ polymerization of nylon. The epitaxial crystallization of nylon monomer on graphite fiber surfaces has been investigated. Graphite-fiber, nickel-matrix composites were further characterized at room and at elevated temperatures. Measurements of Young's moduli, tensile strength, stress rupture, thermal expansion, and thermal fatigue are presented. Graphite filament degradation resulting from fabrication (hot-pressing) of nickel matrix composites was also determined.

Contents of Volume III:

The work presented in this volume is concerned with the performance prediction, testing, and post-test evaluation of a representative graphite-fiber, resin-matrix aircraft fuselage component. Additional material properties were determined and structural margins of safety defined by discrete element analysis. After seven response tests under various load combinations, the component was tested to destruction under combined bending and shear loads. Failure occurred at 110 percent of the target design load but below the failure load predicted from tests on flat panels. A weight saving of 27 percent over an aluminum structure of equivalent strength was demonstrated. The component was also three times stiffer than an aluminum structure of the same weight. Performance projections indicate that the same component built with presently available "Thornel" 50S

fibers would offer a weight saving of 49 percent. Post-test evaluations included tensile and compression tests on curved skin panels, on stringers, and on stringer-skin combinations. Optical and electron microscopic examination of the fracture surfaces provided further insight into the failure mechanism.

SECTION III

COMPOSITE SYNTHESIS

A. Stiffened Cylinder Optimization (Professor Kicher and Dr. T. L. Chao)

With the development of new composite materials, a design engineer has the opportunity of ultimately being able to design a structural configuration and material simultaneously. However, to accomplish this task it will require fundamental advances in structural synthesis as well as an improved understanding of the structural behavior of composite structures. This work is aimed at advancing the techniques of structural synthesis in design with fibrous composites. By extending the technique to composition and material variables, it provides a tool to assist the engineer in the intelligent exploitation of the potential offered by composite materials.

The basic concepts of structural synthesis were developed and reported by Schmit and his associates. (7,8) The concepts have been applied successfully to the optimum design of integrally stiffened cylindrical shells by Kicher(9) and Schmit-Morrow-Kicher. (10) In general, structural synthesis, or automated optimum design of structural systems, can be cast into a model of a mathematical programming problem which seeks to maximize or minimize a function of several variables. The variables are subjected to certain constraints which are not amenable to solution by the classical methods of calculus. Composite structures must be designed with an integrated design-analysis approach supported closely by materials and processing criteria. In order to carry out this work successfully, a designer is required to have a comprehensive knowledge of design, manufacturing, and analytical methods. This complicates greatly the design processes. It is hoped, in this respect, that an extended technique of structural synthesis will assist an engineer to achieve an optimum structural design.

The main features of the computer capability developed for finding a minimum weight design of stiffened fiber composite cylinders can be summarized in the following:

1. Multiple load conditions - each load condition composed of axial, radial, and torsional load combinations.
2. Design begins with the elastic properties of the constituent materials, fiber and matrix.
3. Design variables include the material parameters of fiber orientations and fiber content.
4. The buckling analysis of the heterogeneous anisotropic cylindrical shell is based upon the small deflection theory of thin shells. The cylinder is assumed to buckle into a torsional wave-form.

5. Eight sets of boundary conditions are provided
6. bounds on all design variables are permitted.
7. Optimum design is obtained by minimizing the objective function with the design variables subject to side and behavior constraints.

Figure 1 shows a sketch of the shell with stiffeners located inside the cylinder wall. The design variables are the configuration parameters: dimensions and spacings of the stiffeners; and the material parameters: fiber orientations and fiber content. The thickness of the composite is determined from the fiber volume content. The stiffened shell is designed against the following modes of failure.

1. gross buckling
2. panel buckling
3. skin buckling
4. stiffener bucklings
5. combined-stress failure in a ply
6. delamination failure between two adjacent plies.

Behavior constraints are formulated based on the failure stresses and strains. Side constraints are the lower and upper bounds on the design variables, and the limits on the geometric admissibilities among the dimensions and spacings of the stiffeners. Together they form the constraint set. The objective function is the total weight of the cylinder.

If the stiffeners in both the longitudinal and circumferential directions are assumed to be closely spaced, then the elastic properties of the stiffeners may be considered to be smearable in the two directions over the skin. Thus the force-displacement relations are obtained by performing the appropriate integrations of the stresses over the skin and the stiffeners with the mid-surface of the skin taken as the reference surface. Timoshenko's buckling equilibrium equations (11) are used for the buckling analysis of the cylinder. The skin buckling loads are approximated with Donnell's equations. (12) The hat section stiffeners are analyzed as a collection of plate elements. Methods to determine the limiting strength of composite materials are based on the work of Chamis. (13) Material failure modes considered are the individual ply failures and the ply delaminations between two adjacent plies.

The minimum weight design problem is cast into a model of a nonlinear mathematical programming problem. The Fiacco-McCormick penalty function technique is used for solving the programming problem. Since the objective or weight function is independent of the ply orientations, special modifications have been made in the synthesis scheme so that the weight is minimized with respect to all design variables and the strength of the structure is maximized with respect to the ply angles.

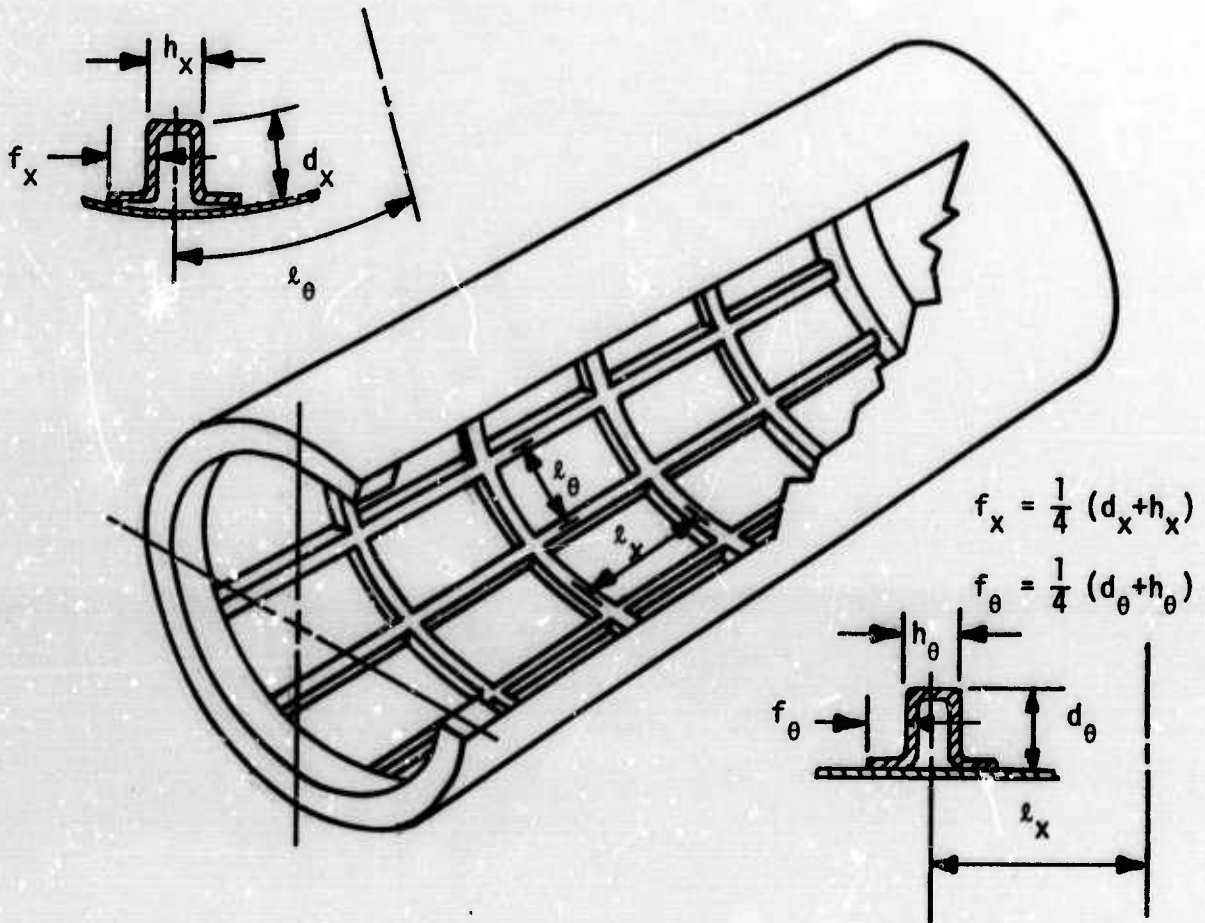


Figure 1. Integrally Stiffened Cylinder with Hat Cross-Section Stiffeners.

A topical report on this subject has been completed by T. L. Chao (14) and submitted to Case Western Reserve University in partial fulfillment of the Ph.D. Degree. That document is also available as an AFML report TR 69-251. The results were summarized and presented at the AIAA/ASME 11th Structures, Structural Dynamics and Materials Conference, Denver, Colorado, April 22-24, 1970.



B. Minimum Weight Design of Composite Structures
(Dr. R.A. Gellatly and D. Dupree, Bell Aerospace)

Development of an automated optimization program for stiffened composite panels was undertaken. The basis for the program was utilization of discrete element structural analysis methods in combination with a mathematical programming penalty function formulation. This approach differs from that of the previous report section which considered a "smeared stringer" model of the fuselage structure. It was recognized from the outset that the introduction of composite materials would raise the level of complexity considerably over an equivalent optimization program operating on conventional metallic structures.

The overall program logic flow was developed and incorporated a streamlined version of an operational Bell General Purpose Analysis Program combined with an unconstrained optimization procedure. Because of the complexity of the resulting large-scale program, development and check-out procedures were conducted in two stages. In the first stage, attention was confined to use of simple isotropic material elements to verify operation of the optimization procedure. In the second stage, analysis procedures were expanded to accommodate anisotropic material.

A sample optimization problem was attempted for the first stage check-out, and significant weight reductions were achieved when geometric variables and member sizes were used as design parameters. The problem consisted of a two-dimensional isotropic membrane panel fixed along one edge and loaded in its own plane. The manner of support and loading was designed to represent a tip-loaded cantilever beam-plate. Figure 2 shows the finite element idealization of the initial design which consisted of 12 rectangular membrane plate elements. The structure was required to be symmetric about its horizontal center line, and analysis was confined to the upper half of the beam with appropriate boundary conditions. Design variables were the y-coordinates of Nodes 1-8 and two thicknesses: the three upper elements of the top beam half were required to have equal thickness t_1 and the three lower elements were required to have equal thickness t_2 . Figure 3 shows the design achieved after three minimizations. The initial and final values of the design variables are given in Table I. The corresponding initial and final weights are 3.030 and 0.216 lb, respectively. The initial design does not represent an efficient starting point such as a fully stressed design; but, nevertheless, the results indicate the apparent effectiveness of the optimization and analysis combination.

TABLE I
ISOTROPIC BEAM-PLATE OPTIMIZATION

Design Variable	Initial Design	Final Design
Y ₁	5.000 in.	1.845 in.
Y ₂	5.000	1.055
Y ₃	5.000	1.053
Y ₄	5.000	0.988
Y ₅	2.500	0.923
Y ₆	2.500	0.527
Y ₇	2.500	0.527
Y ₈	2.500	0.495
t ₁	0.100	0.0289
t ₂	0.100	0.0289

Following successful check-out of the optimization and basic analysis logic, the analysis routine was expanded to include all logic associated with composite structures. Included were the computation of equivalent homogeneous composite properties from the basic layer (the stacking process) and a procedure for transforming gross material stresses into individual layer stresses for determination of failure modes. In addition, and under company support, a rectangular anisotropic finite element was developed for use in the overall analysis procedure.

Program check-out was initiated, but, due to unexpected difficulties and computational expense associated with the finite element analysis routines, verification was not completed, in spite of having introduced a simplified analysis approach. No production executions of the program were therefore accomplished. The following paragraphs describe effort that was completed on the program.

Stress Analysis Procedure

Finite element methods of structural analysis are widely used because of their advantages in generality of application to structural forms. With a large library of element types developed for the analysis of many types of structures, analysis can be readily accomplished in a logical and automated manner. The representation of the full equivalent homogeneous anisotropic material properties for assembled multilayer fiber composites (including effects of membrane-flexural coupling) is carried out using a stacking process. Each layer is modeled by an orthotropic parallelepiped with principal axes corresponding to the fiber direction. By application of the condition of linearity of a surface normal, the resultant multidegree-of-freedom model is condensed to yield a stiffness tensor for the assembled composite material in terms of gross membrane forces and moments.

For the design optimization, a flat panel stiffened by hat-section stringers was selected (Figure 4). The basic repeating section of the panel, after application of symmetry conditions, was modeled for a finite element analysis by 18 rectangular plates as indicated in Figure 5. In order to include full membrane-flexural coupling effects, a new rectangular finite element was developed for use in Bell's General Purpose Analysis Program. The element was a simplification of a cylindrical rectangular element derived initially in Reference 15. Formulation of the element relationships, stiffness, and stress matrices was very complex, even with elimination of terms in the matrices associated with cylindrical curvature. The element was successfully coded, and check-out procedures were initiated. At this stage, it was found that excessively long computer times were required. For the simple generation and assembly of a single element stiffness matrix, not including the stress matrix, approximately 2 minutes of IBM 360/65 computer time were required. For the full 18-element model for the stiffened plate, the assembly time was over 30 minutes. Solution of the resultant equations, assembly of stress matrices and final decomposition of stresses down to layer level increased the total time for a single analysis to over 1 hour on the 360/65 computer. Even for analysis these times and associated costs are excessive, while for an optimization program involving many analyses during the search procedure, the program becomes economically unfeasible.

From the past operational experience with computer-based analyses, the analysis of a large complex structure (e.g. 15,000 degrees-of-freedom) involves approximately 30 hours of computer time. This condition may be regarded as a practical upper limit on a single analysis with current computer capabilities. Larger running times would bring important questions of computer

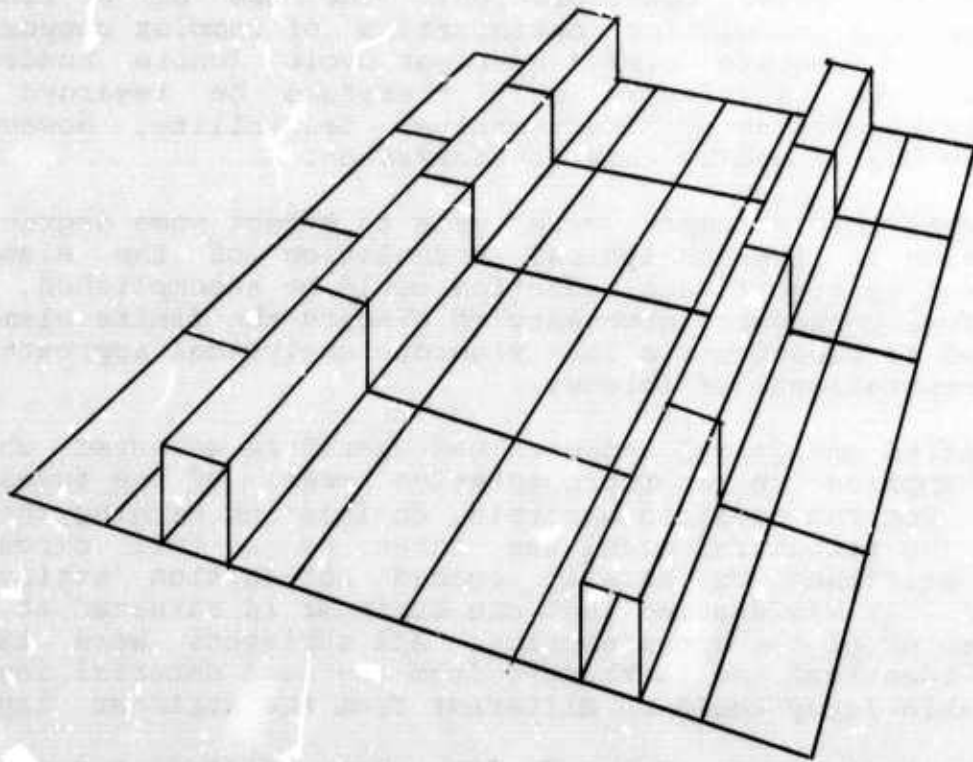


Figure 4. Original Flat Panel Section

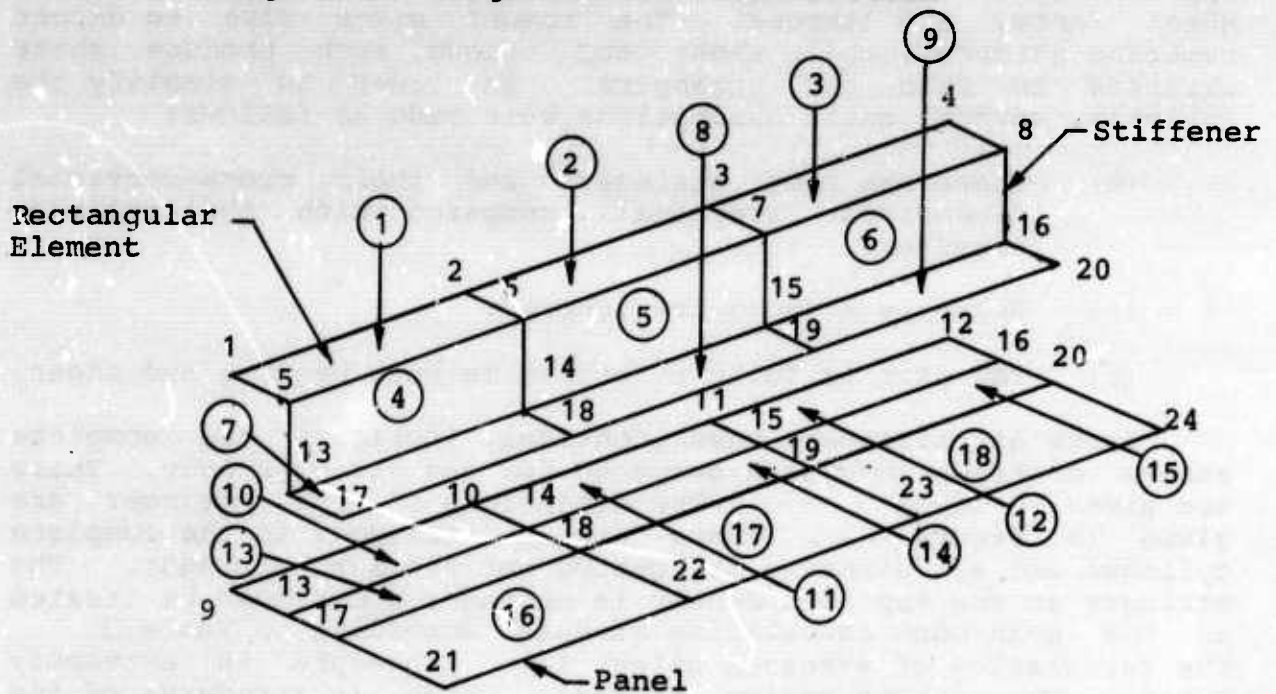


Figure 5. Stiffened Panel Geometry and Idealization

reliability into major consideration. The use of a finite element analysis model for optimization of complex composite structures which require over 1 hour per cycle (where hundreds of cycles are involved) must therefore be regarded as economically unacceptable. The technical feasibility, however, is in no way challenged by this consideration.

A number of attempts were made to effect some degree of simplification in the analytical formulation of the element matrices, but no significant reduction could be accomplished. It was therefore considered necessary to discard the finite element approach and to substitute a less rigorous analytical approach to increase computational efficiency.

A modified analytical approach was therefore selected which could be applied to a representative model of the fuselage component. For the modified analysis, engineering bending theory was used. The structural model was taken as a full circular cylinder stiffened by equally spaced hat-section stringers (Figure 6). It was assumed that one stringer is situated at the top dead center of the cross section. All stringers were taken as being identical and fabricated from the same material layup. The outer skin layup could be different from the stringer layup.

The cylinder was analyzed for three different types of applied loads: bending moment about a horizontal axis, vertical shear force, and torque. The moment gives rise to direct membrane stresses, while shear and torque each produce shear stresses in skin and stringers. In order to simplify the analysis, several basic assumptions were made as follows:

- (a) There are many stringers and their cross-sectional dimensions are small compared with the cylinder diameter.
- (b) Boundary effects are ignored.
- (c) The skin is fully effective in both bending and shear.

Since all stringers have identical sections, the complete stress distributions were computed for one stringer only. These are given in Table II. The dimensions of the stringer are given in Figure 7. There are n stringers in the complete cylinder and all stresses are quoted for the i -th stringer. The stringer at the top dead center is stringer 0 but must be treated as the n -th when calculating stresses according to Table II. The calculation of stresses using this procedure is extremely rapid. The decomposition process, which is a reverse of the stacking procedure, is still applied after calculation of gross

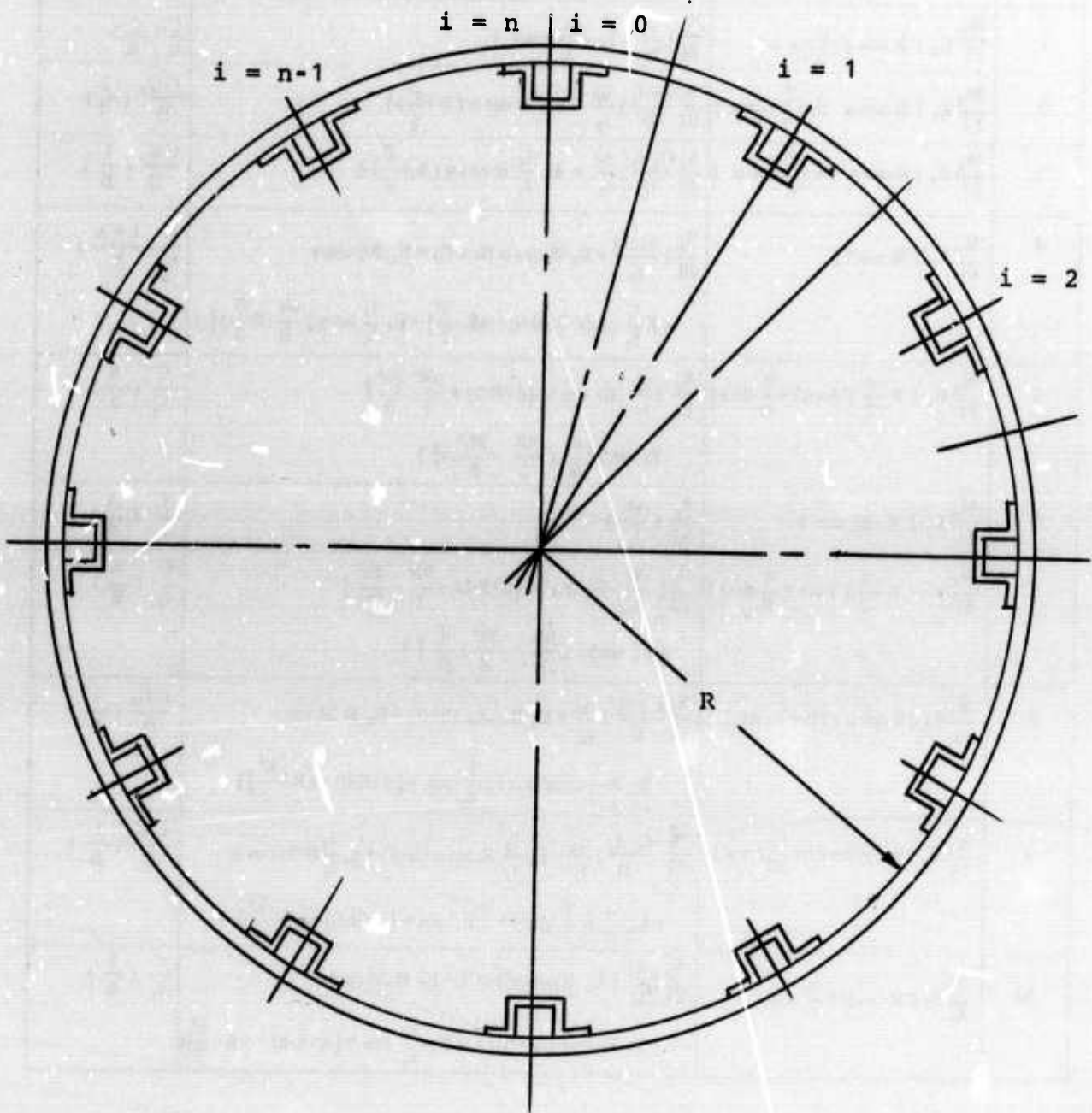


Figure 6. Cylinder Cross Section

TABLE II
STRESSES FROM BENDING THEORY

Zone	Bending	Shear	Torsion
1.	$\frac{M_x}{EI} E_2 [R \cos \alpha - \frac{b}{2} \sin \alpha]$	$\frac{S_z}{EI} [\frac{q_0}{t_2} + E_2 \frac{Rb}{2} \cos \alpha]$	$\frac{C}{t_2} (\frac{1}{B})$
2.	$\frac{M_x}{EI} E_2 [R \cos \alpha - (b + \frac{f}{2}) \sin \alpha]$	$\frac{S_z}{EI} \frac{G_2 t_2}{D} [\frac{q_0}{t_2} + E_2 R \cos \alpha (b + \frac{f}{2})]$	$\frac{CG_2}{D} (\frac{1}{B})$
3.	$\frac{M_x}{EI} E_1 [R \cos \alpha - (b + \frac{f}{2}) \sin \alpha]$	$\frac{S_z}{EI} \frac{G_1 t_1}{D} [\frac{q_0}{t_1} + E_2 \frac{t_2}{t_1} R \cos \alpha (b + \frac{f}{2})]$	$\frac{CG_1}{D} (\frac{1}{B})$
4.	$\frac{M_x}{EI} E_2 [R \cos \gamma]$	$\frac{S_z}{EI} [\frac{q_0}{t_2} Q + E_2 R \cos \alpha (b + f') + E_2 R d \cos \gamma]$ $+ E_1 \frac{t_1}{t_2} \cos \gamma \{ d(Rh) + hR \cdot \frac{h^2}{2} \} + E_1 \frac{t_1}{t_2} \sin \gamma \{ \frac{dh}{R} (R - \frac{h}{2}) \}]$	$\frac{C}{t_2} (\frac{1+A}{B})$
5.	$\frac{M_x}{EI} E_1 [R \cdot \frac{h}{2}] [\cos \gamma + \frac{d}{R} \sin \gamma]$	$\frac{S_z}{EI} [\frac{Q}{t_1} - E_1 \cos \gamma \{ d(R-h) + \frac{hR}{2} - \frac{3h^2}{8} \}]$ $- E_1 \sin \gamma \{ \frac{d}{R} (\frac{hR}{2} - \frac{3h^2}{8}) \}]$	$\frac{C}{t_1} (\frac{A}{B})$
6.	$\frac{M_x}{EI} E_1 [R - h] \cos \gamma$	$\frac{S_z}{EI} [\frac{Q}{t_1}]$	$\frac{C}{t_1} (\frac{A}{B})$
7.	$\frac{M_x}{EI} E_1 [R \cdot \frac{h}{2}] [\cos \gamma - \frac{d}{R} \sin \gamma]$	$\frac{S_z}{EI} [- \frac{Q}{t_1} - E_1 \cos \gamma \{ d(R-h) + \frac{hR}{2} - \frac{3h^2}{8} \}]$ $+ E_1 \sin \gamma (\frac{hR}{2} - \frac{3h^2}{8}) \frac{d}{R} \}]$	$\frac{C}{t_1} (\frac{A}{B})$
8.	$\frac{M_x}{EI} E_2 [R \cos \beta + (b + \frac{f}{2}) \sin \beta]$	$\frac{S_z}{EI} \frac{G_2 t_2}{D} [\frac{q_0}{t_2} + E_2 R \cos \alpha (b + f') + E_2 R 2d \cos \gamma]$ $+ E_2 R \frac{f'}{2} \cos \beta + 2 E_1 \frac{t_1}{t_2} \cos \gamma \{ d(R-h) + hR \cdot \frac{h^2}{2} \}]$	$\frac{CG_2}{D} (\frac{1}{B})$
9.	$\frac{M_x}{EI} E_1 [R \cos \beta + (b + \frac{f}{2}) \sin \beta]$	$\frac{S_z}{EI} \frac{G_1 t_1}{D} [\frac{q_0}{t_1} + E_2 \frac{t_2}{t_1} R \cos \alpha (b + f') + E_2 \frac{t_2}{t_1} R 2d \cos \gamma]$ $+ E_2 \frac{t_2}{t_1} R \frac{f'}{2} \cos \beta + 2 E_1 \cos \gamma \{ d(R-h) + hR \cdot \frac{h^2}{2} \}]$	$\frac{CG_1}{D} (\frac{1}{B})$
10.	$\frac{M_x}{EI} E_2 [R \cos \beta + \frac{b}{2} \sin \beta]$	$\frac{S_z}{EI} [\frac{q_0}{t_2} + E_2 R \cos \alpha (b + f') + E_2 R 2d \cos \gamma]$ $+ E_2 R \cos \beta (\frac{b}{2} + f') + 2 E_1 \frac{t_1}{t_2} \cos \gamma \{ d(R-h) + hR \cdot \frac{h^2}{2} \}]$	$\frac{C}{t_2} (\frac{1}{B})$

TABLE II (CONT)

$$A = \frac{G_1 t_1}{G_1 t_1 + G_2 t_2} \left[\frac{2h-R - \frac{G_1 t_1}{G_2 t_2} \left(\frac{1}{2h} - \frac{\pi R - \pi f}{\pi R^2} \right)}{\frac{d+h}{2dh} + \frac{G_1 t_1}{G_2 t_2} \left(\frac{1}{2h} - \frac{nd}{\pi R^2} \right)} \right]$$

$$B = 1 + \frac{2n dh}{\pi R^2} A$$

$$C = \frac{T}{2\pi R^2}$$

$$D = (G_1 t_1 + G_2 t_2)$$

$$\alpha = \frac{\pi}{n} (2i-1)$$

$$\beta = \frac{\pi}{n} (2i+1)$$

$$EI = \pi R^3 E_2 t_2 + \pi R E_1 t_1 \left[R(d+f+h) - h(2d+h) \right]$$

$$f' = f \left(1 + \frac{E_1 t_1}{E_2 t_2} \right)$$

$$\gamma = 2 \frac{\pi i}{n}$$

$$q_0 = \left[R^2 E_2 t_2 \sin \alpha + E_1 t_1 \left\{ R(d+h+f) - (dh + \frac{h^2}{2}) \right\} \left(1 + 2 \sum_{j=1}^{i-1} \cos \frac{2\pi j}{n} \right) \right]$$

$$Q = \frac{G_1 G_2 t_1 t_2}{(h+d) G_1 t_1 + d G_2 t_2} \left[\sin \gamma \left\{ \frac{dh}{R} \left[\left(\frac{Rh}{2} - \frac{h^2}{3} \right) \frac{E_1 t_1}{G_2 t_2} \right] \right\} + \cos \gamma \left\{ d(dR - dh + Rh - \frac{h^2}{2}) \frac{E_1 t_1}{G_2 t_2} + d^2 R \frac{E_2}{G_2} \right\} \right. \\ \left. + \cos \alpha \left(b + f' \right) d R \frac{E_2}{G_2} + \frac{q_0 d}{G_2 t_2} \right]$$

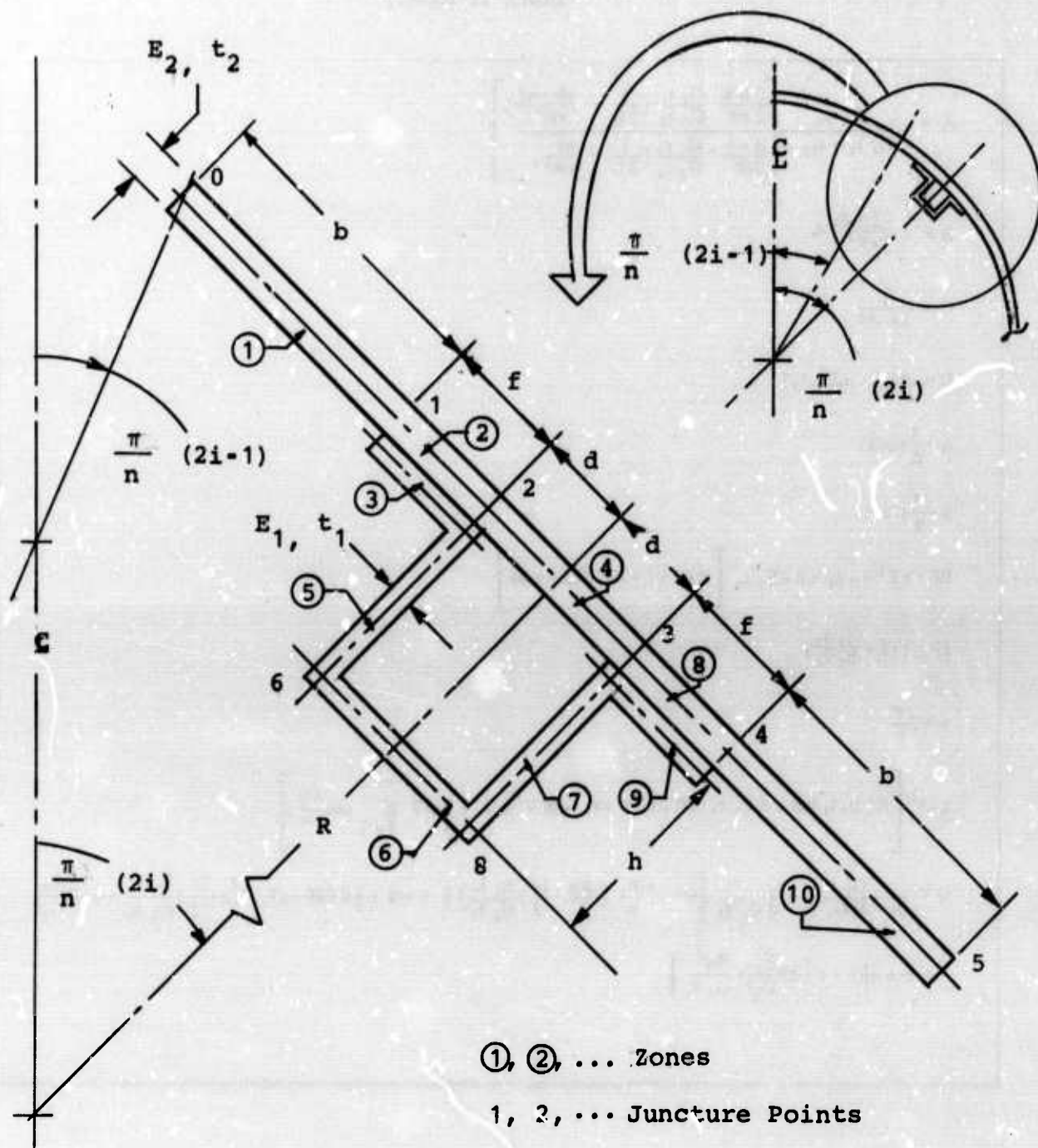


Figure 7. Detail of Single Skin - Stringer

stresses to determine individual layer stresses for use in the failure criteria expression.

The overall program logic presented in Reference 3 remains substantially unaltered by this new formulation. The program modules associated with analysis of the finite element model have been removed completely and replaced by a simple routine which evaluates the overall stresses according to the bending theory analysis of Table II. All logic prior to and following the analysis was effectively unaltered by this substitution.

SECTION IV

BEHAVIOR OF COMPOSITE STRUCTURAL ELEMENTS

A. Post-Buckling of Anisotropic Plates Under Axial Compression (Professor Kicher and Mr. D. Chan)

The post-buckling behavior of laminated, anisotropic plates was investigated. The Love-Kirchoff assumptions for thin plates and Von-Karman's large displacement kinematic relations were used. The potential energy expression was formulated on the basis of an extensional plate theory. Plates treated are rectangular with all four edges either clamped or simply supported. The plates are loaded on two opposite sides with the unloaded edges either laterally restrained or free to expand. The loaded edges are subjected to either uniform force or uniform displacement. All load levels are such that the plate material remains elastic. The solution was carried out along the line of Raleigh-Ritz method with only the transverse displacement mode, w , assumed; the remaining two displacement modes, u and v , being obtained exactly from the two nonlinear membrane equilibrium equations.

The results indicate that uniform force load and uniform displacement load yield exactly the same post-buckling load vs. deflection curve. For most plates, buckling is a bifurcation phenomenon; however, for certain types of plates with certain types of boundary conditions, the plate deflects as soon as the load is applied. Solutions were obtained for simply supported plates with a single transverse mode assumption and with a double transverse mode assumption.

The method of solution has been put into a Fortran program which requires the plate aspect ratio, thickness, material constants and wave numbers as inputs and yields the load vs. deflection, shortening, effective width and resultant force distribution relations as outputs. Average computing time on Univac 1108 for plate analysis is between four to seven seconds.

Figures 8, 9, and 10 present the load deflection curve, effective width versus shortening curve and the load shortening curve for a (0,90,90,0) "Thornel" - 25 plate respectively. This plate was tested earlier in the program by Mandell (3) and analyzed by Monforton. Figure 8 shows that the results compare favorably during the early stages of loading. Improvements in the post-buckling prediction could be achieved by assuming more terms for the w displacement expression.

A topical report on this subject has been completed and submitted to Case Western Reserve University by D. P. Chan as partial completion of the degree requirements.

B. Post-Buckling Strength of Composite Plates (Professor T. P. Kicher and Mr. M. T. Islam)

Recent studies on the buckling and post-buckling of laminated plates indicate that significant loads can be sustained after buckling if the associated

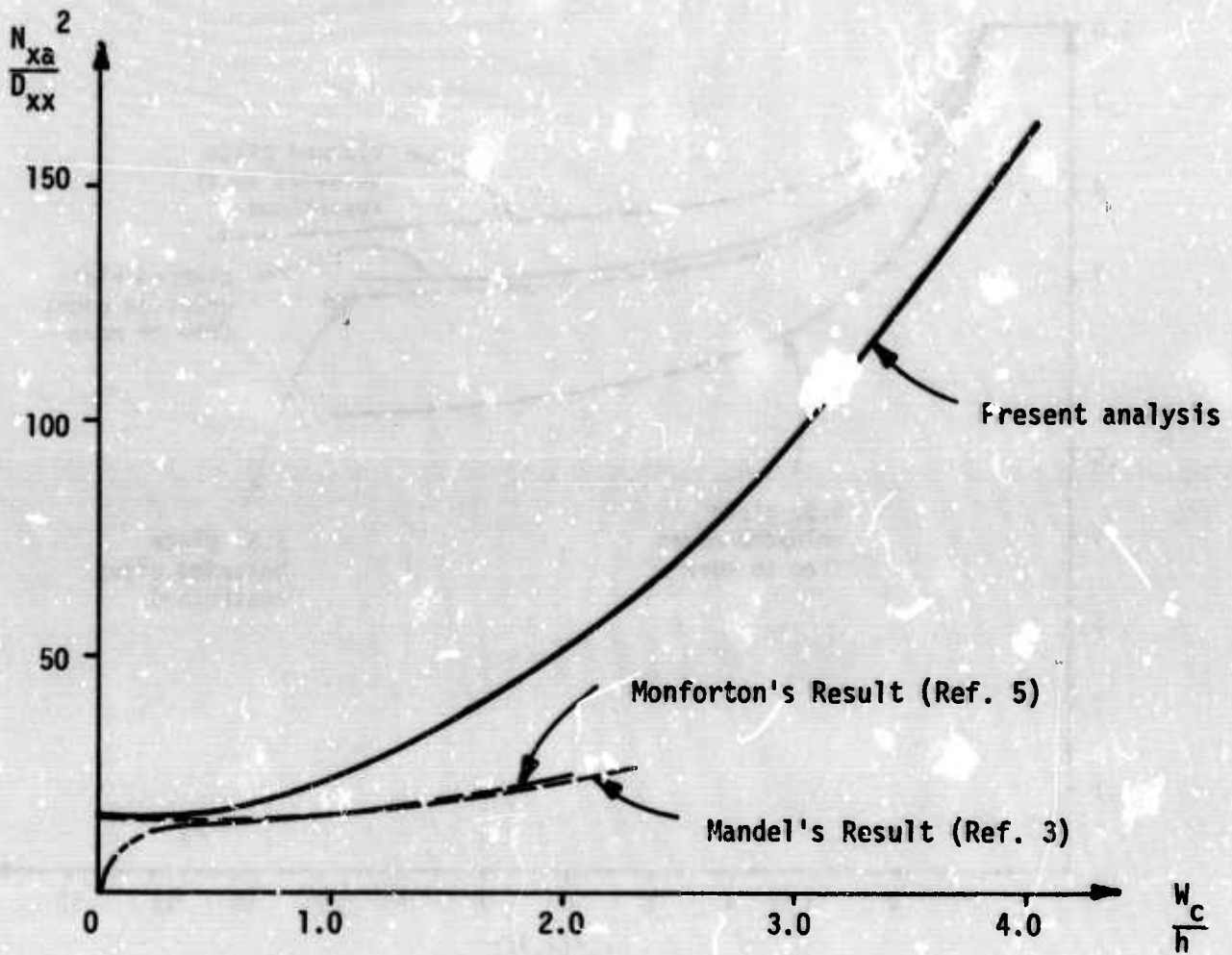


Figure 8. Load-Deflection Curve for (0,90,90,0) "Thorne1" 25 Plate Simply Supported and with Unloaded Edges Free to Expand

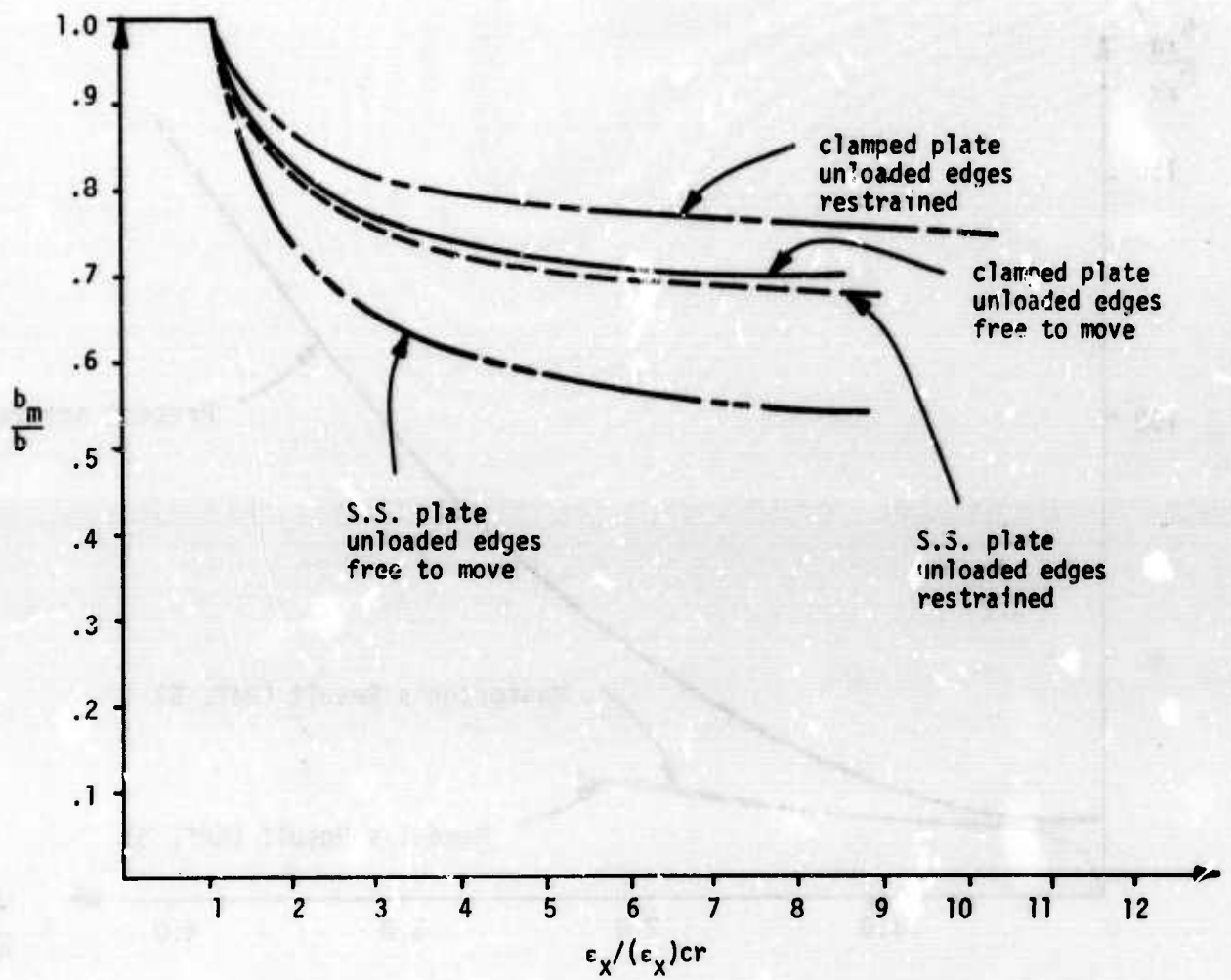


Figure 9. Effective Width vs. Shortening Curve (0,90,90,0) "Thorne1" 25 Plate

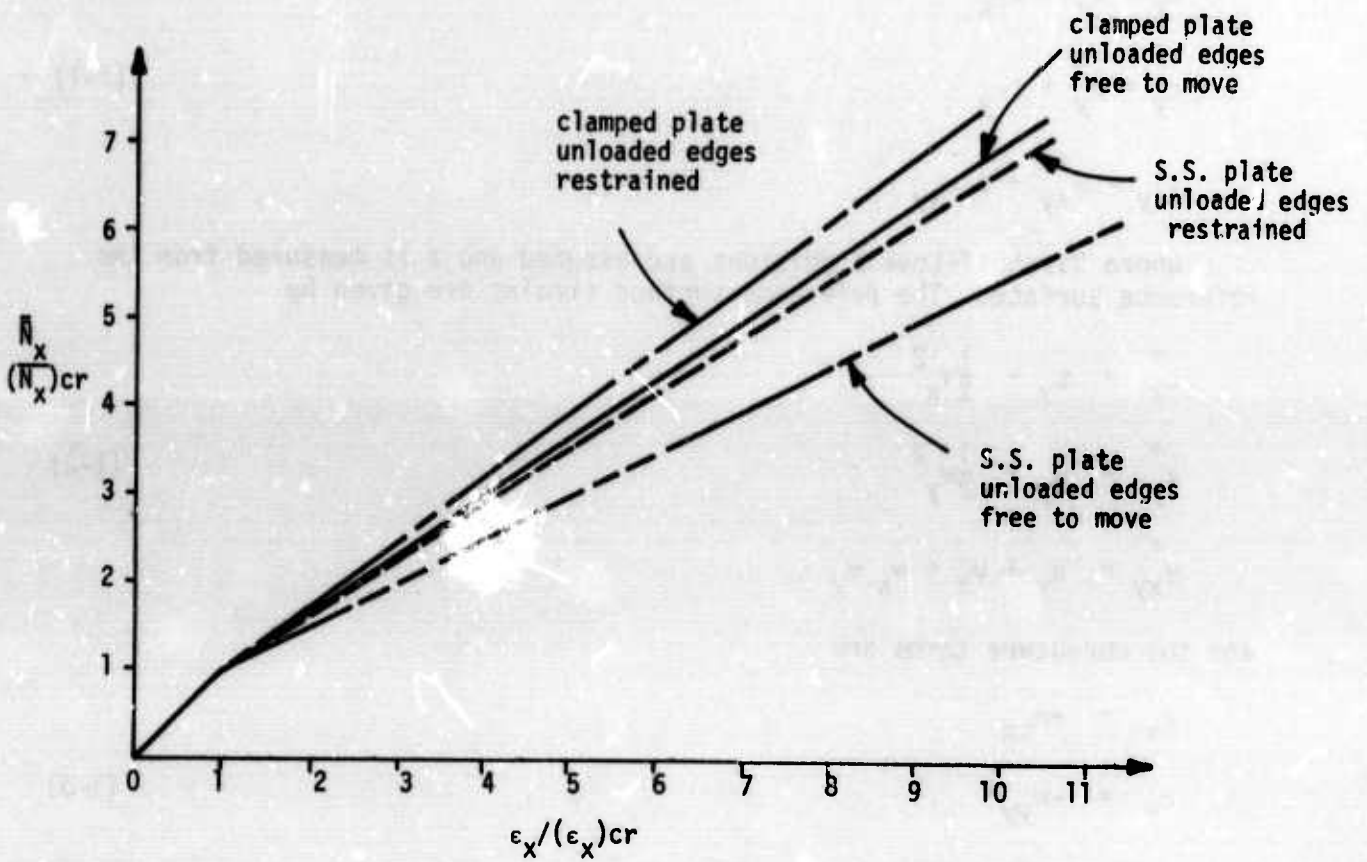


Figure 10. Load Shortening Curve for (0,90,90,0) "Thorne1" 25 Plate

large displacements can be tolerated. The high stiffness of composites leads to thin laminates for lightly loaded structures, consequently, the high strength potential is not utilized. If analytical methods of predicting the post-buckling response and strength were available, designers could utilize the full potential of the post-buckling region. The post-buckling response is reported in the previous section while the strength analysis is reported herein.

1. General Edge Loading

The strain displacement relations for plates under large deflections can be given by

$$\begin{aligned}\epsilon_x &= \epsilon_x^{\circ} + z\kappa_x \\ \epsilon_y &= \epsilon_y^{\circ} + z\kappa_y \\ \gamma_{xy} &= \gamma_{xy}^{\circ} + z\kappa_{xy}\end{aligned}\tag{1-1}$$

where Kirchoff-Love conditions are assumed and z is measured from the reference surface. The reference surface strains are given by

$$\begin{aligned}\epsilon_x^{\circ} &= u_x + \frac{1}{2}w_x^2 \\ \epsilon_y^{\circ} &= u_y + \frac{1}{2}w_y^2 \\ \gamma_{xy}^{\circ} &= u_y + u_x + w_x w_y\end{aligned}\tag{1-2}$$

and the curvature terms are

$$\begin{aligned}\kappa_x &= -w_{xx} \\ \kappa_y &= -w_{yy} \\ \kappa_{xy} &= -2w_{xy}\end{aligned}\tag{1-3}$$

The subscripts of u , v and w terms indicate partial derivatives. The force deformation relationship for the general anisotropic plate is then

$$\begin{Bmatrix} N \\ M \end{Bmatrix} = \begin{bmatrix} A & B \\ B & D \end{bmatrix} \begin{Bmatrix} \epsilon^{\circ} \\ \kappa \end{Bmatrix}\tag{1-4}$$

where

$$N = \left\{ \begin{array}{l} N_x \\ N_y \\ N_{xy} = N_{yx} \end{array} \right\}$$

$$M = \left\{ \begin{array}{l} M_x \\ M_y \\ M_{xy} = M_{yx} \end{array} \right\}$$

$$\varepsilon^o = \left\{ \begin{array}{l} \varepsilon_x^o \\ \varepsilon_y^o \\ \varepsilon_{xy}^o \end{array} \right\}$$

$$\kappa = \left\{ \begin{array}{l} \kappa_x \\ \kappa_y \\ \kappa_{xy} \end{array} \right\}$$

$$A = [a_{ij}]$$

$$B = [b_{ij}] \quad \{i, j = 1, 2, 6\}$$

$$D = [d_{ij}] .$$

Now define

$$U_1 = \frac{1}{2} \int_s \{ [a_{11} u_x^2 + a_{22} v_y^2 + a_{66} (u_y + v_x)^2 + 2a_{12} u_x v_y + 2a_{16} (u_y + v_x) u_x + 2a_{26} (u_y + v_x) v_y] - 2 [b_{11} u_x w_{xx} + b_{22} v_y w_{yy} + 2b_{66} (u_y + v_x) w_{xy} + b_{12} (v_y w_{xx} + u_x w_{yy}) + b_{16} (u_y + v_x) w_{xx} + 2b_{16} u_x w_{xy} + b_{26} (u_y + v_x) w_{yy} + 2b_{26} v_y w_{xy}] + [d_{11} w_{xx}^2 + d_{22} w_{yy}^2 + ed_{66} w_{xy}^2 + 2d_{12} w_{xx} w_{yy} + 4d_{16} w_{xx} w_{xy} + 4d_{26} w_{yy} w_{xy}] \} ds \quad (1-5)$$

and

$$U_2 = \frac{1}{2} \int_s \{ [a_{11} u_x w_x^2 + a_{22} v_y w_y^2 + 2a_{66} (u_y + v_x) w_x w_y + a_{12} (u_x w_y^2 + v_y w_x^2) + a_{16} (u_y + v_x) w_x^2 + a_{16} u_x w_x w_y + a_{26} (u_y + v_x) w_y^2 + a_{26} v_y w_x w_y] - [b_{11} w_{xx} w_x^2 \quad (cont'd)$$

$$+ b_{22} w_{yy} w_y^2 + 4b_{66} w_x w_y w_{xy} + b_{12} (w_{xx} w_y^2 + w_{yy} w_x^2) \quad (1-6)$$

$$+ b_{16} (2w_{xy} w_x^2 + w_x w_y w_{xx}) + b_{26} (2w_{xy} w_y^2 + w_x w_y w_{yy}) \} ds$$

$$U_3 = \frac{1}{2} \int_s \left\{ \frac{1}{4} [a_{11} w_x^4 + a_{22} w_y^4] + [a_{66} + \frac{1}{2} a_{12}] w_x^2 w_y^2 \right. \\ \left. + 2 [a_{16} w_x^3 w_y + a_{26} w_x w_y^3] \right\} ds \quad (1-7)$$

where s indicates the surface of the plate. Then the strain energy of the plate is

$$U = U_1 + U_2 + U_3 \quad (1-8)$$

The potential of the applied loads is

$$W = \oint_y [\bar{N}_x u + \bar{N}_{xy} v + \bar{Q}_{xz} w - \bar{M}_x w_x - \bar{M}_{xy} w_y] dy \\ - \oint_x [\bar{N}_{yx} u + \bar{N}_y v + \bar{Q}_{yz} w - \bar{M}_{yx} w_x - \bar{M}_y w_y] dx \quad (1-9)$$

where $\bar{N}_x, \bar{N}_y, \bar{N}_{xy}, \bar{N}_{yx}, \bar{Q}_{xz}, \bar{Q}_{yz}$ are forces and $\bar{M}_x, \bar{M}_y, \bar{M}_{xy}, \bar{M}_{yx}$ are moments applied on the edges of the plate.

$$\text{The total potential energy } \pi_p \text{ of the plate is: } \pi_p = U - W \quad (1-10)$$

For prescribed kinematical boundary conditions, states of equilibrium of the plate will correspond to stationary values of the elastic energy. Under hinged or built-in edge conditions the elastic energy consists of the energy of the plate only. For elastically restrained plate edge conditions, the elastic energy of the edge stringers must be added to obtain the total elastic energy. In any case, the stationary value of the elastic energy may be calculated as a function of the applied deformation $\bar{\epsilon}$. The approximate solution may be obtained by Rayleigh's or Rayleigh-Ritz's principle. Let the solution obtained by $u(\bar{\epsilon}), v(\bar{\epsilon}), w(\bar{\epsilon})$ for an applied deformation $\bar{\epsilon}$. Call the elastic energy, which is a function of $\bar{\epsilon}$, $U(\bar{\epsilon})$.

Then

$$\frac{\partial \pi_p}{\partial \bar{\epsilon}} = 0 = \frac{\partial}{\partial \bar{\epsilon}} (U - W) \quad (1-11)$$

$$\text{or } \frac{dU}{d\bar{\epsilon}} = \bar{F} \quad (1-12)$$

where \bar{F} is the edge load (vector). The ultimate load capacity is

$$\bar{F}_u = \max_{\bar{\epsilon}} \frac{dU}{d\bar{\epsilon}} \quad (1-13)$$

2. End Compressive Loading

Consider an orthotropic or anisotropic plate of length a and width b under a compressive load P . The load is applied through a rigid bar at the end, and the plate is supported on all sides.

During the fundamental or unbuckled state, the plate suffers uniform compressive strain ϵ across the width, then the load is distributed uniformly along the edge. After buckling, the center of the plate bows out while the sides remain straight. Because of the membrane stretching caused by the deflection at the middle, the compressive stress there is reduced. To support the same applied load, the sides of the plate then carry proportionately greater parts of the total load P . In the far post-buckled state, the load distribution is as shown in Figure 11(a) where the entire load is carried by two strips of width d , one on each side. The loading is considered to be uniformly distributed across these two strips each carrying half the total load P . Let the membrane compressive load on these strips be N_x . Then

$$P = 2dN_x \quad (2-1)$$

The plate is assumed to be simply supported on all sides. The lateral deflection w along the edges is thus zero. For the purpose of analysis, the middle strip without edge loading is ignored. (Fig. 12)

Orthotropic Case

Classical orthotropic buckling theory can now be applied to the orthotropic plate with material axes aligned with structural axes of the plate, and with the plies oriented symmetrically about the mid-plane of the plate. This theory gives the lateral deflection w due to compressive load along the x axis by

$$D_{11} W_{,xxxx} + 2D_3 W_{,xyxy} + D_{22} W_{,yyyy} + N_x W_{,xx} = 0 \quad (2-2)$$

where D_{ij} are flexural stiffnesses and $D_3 = D_{12} + 2D_{66}$

A solution of equation (2-2) is given by

$$W = \bar{w} \sin \frac{\pi x}{\lambda} \sin \frac{\pi y}{2d} \quad (2-3)$$

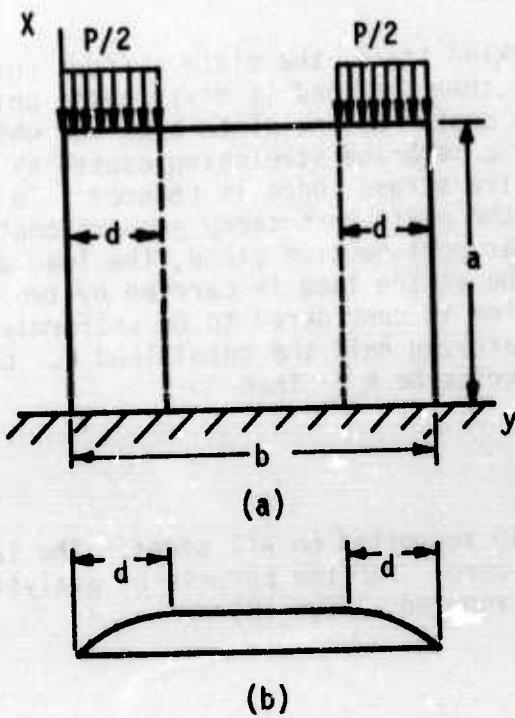


Figure 11
 Post-buckling Load
 Distribution

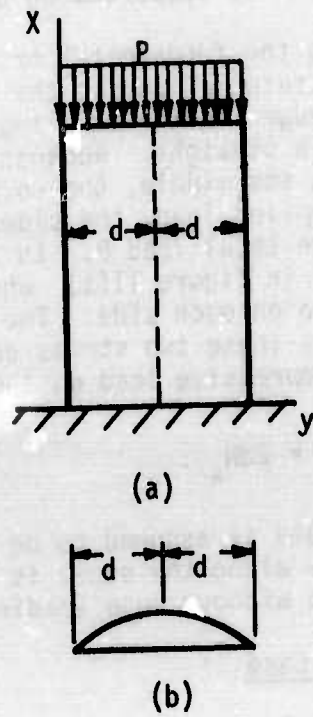


Figure 12
 Post-buckling Analysis
 Model

where λ is the length of a half wave along the x direction. Equation (2-3) satisfies the boundary conditions of the plate i.e., $w = 0$ and $w_{,xx} = 0$ at $x = 0$ or λ and $w = 0$ and $w_{,yy} = 0$ at $y = 0$ or $2d$. Substituting (2-3) into (2-2) and dividing through by $W \sin \frac{\pi x}{\lambda} \sin \frac{\pi y}{2d}$ we get

$$N_x = \pi^2 \left[\frac{D_{11}}{\lambda^2} + \frac{2D_3}{4d^2} + \frac{\lambda^2 D_{22}}{16d^4} \right] \quad (2-4)$$

We assume the two strips carrying the load are at the stability limit corresponding to the critical wave length λ . Differentiating the terms inside the square brackets with respect to λ and equating it to zero

$$\frac{2D_{11}}{\lambda^3} - 2\lambda \frac{D_{22}}{16d^4} = 0$$

$$\lambda = \sqrt[4]{\frac{D_{11}}{D_{22}}} 2d$$

Substituting in (2-4)

$$N_x = \frac{\pi^2}{2d^2} \left[\sqrt{D_{11} D_{22}} + D_3 \right] \quad (2-5)$$

$$d = \frac{\pi}{\sqrt{2N_x}} \left[\sqrt{D_{11} D_{22}} + D_3 \right]^{1/2} \quad (2-6)$$

and

$$P = 2dN_x = \sqrt{2} \pi \left[\left(\sqrt{D_{11} D_{22}} + D_3 \right) N_x \right]^{1/2} \quad (2-7)$$

Replacing N_x by $\sigma_x t$

$$d = \frac{\pi}{\sqrt{2\sigma_x t}} \left[\sqrt{D_{11} D_{22}} + D_3 \right]^{1/2} \quad (2-8)$$

$$P = \sqrt{2} \pi \left[\left(\sqrt{D_{11} D_{22}} + D_3 \right) \sigma_x t \right]^{1/2} \quad (2-9)$$

Equations (2-8 and 2-9) give the relation between effective width and the load. These equations hold up to the elastic limit or yield point for the

material. However, they may be used beyond the elastic limit if D_{11} , D_{22} and D_3 are computed on the basis of the tangent moduli for the material of the plate. For composites where the material is elastic up to the stress corresponding to failure the ultimate load capacity is

$$P_{ult} = \sqrt{2} \pi \left[\left(\sqrt{D_{11} D_{22}} + D_3 \right) \sigma_{xc} t \right]^{1/2} \quad (2-10)$$

where σ_{xc} is the failure stress in longitudinal compression for the composite.

Unbalanced Case

In the case of an orthotropic plate whose laminae are not elastically symmetric with respect to the reference surface, the plate will have bending-membrane coupling. The governing equation for deflection for such a plate is

$$M_{x,xx} + 2M_{xy,xy} + M_{y,yy} + N_x W_{,xx} = 0 \quad (2-11)$$

along with the force deformation relationship

$$\begin{Bmatrix} \{N\} \\ \{M\} \end{Bmatrix} = \begin{bmatrix} [A] & [B] \\ [B] & [D] \end{bmatrix} \begin{Bmatrix} \{\epsilon\} \\ \{\kappa\} \end{Bmatrix} \quad (2-12)$$

The solution for $\{M\}$ from equation (2-12) is

$$\{M\} = [D - BA^{-1}B] \{\kappa\} - [BA^{-1}] \{N\} \quad (2-13)$$

For simplicity neglecting the term $[BA^{-1}] \{N\}$ in equation (2-13) leads to the governing equation

$$D_{11}^* W_{,xxxx} + 2D_3^* W_{,xxyy} + D_{22}^* W_{,yyyy} + N_x W_{,xx} = 0 \quad (2-14)$$

where the D^* terms are elements of the matrix $[D - BA^{-1}B]$.

Equation (2-14) is of the same form as (2-2), and analogous treatment as in the orthotropic case gives

$$d = \frac{\pi}{\sqrt{2\sigma_x t}} \left[\sqrt{D_{11}^* D_{22}^*} + D_3^* \right]^{1/2} \quad (2-15)$$

$$P = \sqrt{2} \pi \left[\left(\sqrt{D_{11}^* D_{22}^*} + D_3^* \right) \sigma_x t \right]^{1/2} \quad (2-16)$$

Equations (2-15 and 2-16) give the relation between the effective width and the load. As in the orthotropic case these equations hold up to the elastic limit if D_{11}^* , D_{22}^* and D_3^* are computed on the basis of tangent moduli. For composite materials which remain elastic up to failure, we obtain the ultimate load capacity

$$P_{ult} = \sqrt{2} \pi \left[\left(\sqrt{D_{11}^* D_{22}^*} + D_3^* \right) \sigma_{xc} t \right]^{1/2} \quad (2-17)$$

where σ_{xc} is the failure stress for the anisotropic composite in longitudinal compression.

Equations (2-10 and 2-17) have been used to compute the ultimate load capacities of various composite plates with different ply lay-ups and thicknesses. Results indicate considerable reserve strength beyond the buckling load. Work is in progress towards verification of the theories through experiment.

C. Buckling of Laminated Composite Plates with Cutouts (Professor T. P. Kicher and Mr. J. Martin)

The purpose of this study is to investigate the buckling of laminated composite plates with cutouts, and to determine the effect of the cutouts on the buckling loads.

A preliminary investigation was made on an 8-ply laminated square plate, 10 in. by 10 in. by .080 in., with 2 in. and 4 in. diameter circular cutouts in the center. The plate was made from "Scotchply" Reinforced Plastic Type 1002, a moldable epoxy-glass laminate. The ply orientations were 0, 45, -45, 90, 90, -45, 45, 0. Buckling loads were found experimentally. The plate was loaded axially and simply-supported on all four edges. Microscopic inspection of the plate revealed large and numerous voids.

In order to produce uniform laminated plates a fabrication process was developed using a Patterson-Kelly autoclave. Two 10-ply unidirectional laminated square plates, 12 in. by 12 in. by .100 in., were fabricated from "Scotchply" Reinforced Plastic Type 1002. A vacuum bag technique was employed: woven glass and Teflon were used between the uncured laminate and a piece of rubber was placed on top of the final layer of woven glass. Gage pressure inside the autoclave was maintained at 18-20 psi, and temperature was maintained at 330-340°F during the 35 minute cure cycle. After the cure cycle had been completed, the plate was allowed to cool very slowly inside the autoclave while the gage pressure and vacuum were still maintained. This procedure produced a plate which was very flat. Fiber wash was found to be negligible, and void content was low. The average cured thickness was .010 in. per ply.

Brittle coating techniques were applied to a laminated plate having a circular cutout in a preliminary investigation of the strain field for the plate under axial load.

A literature search was started pertaining to buckling of laminated composite plates with cutouts; it seems as though the published literature on this topic is very small.

D. Accuracy Study of Shell Theories for Anisotropic Cylinders
(Professor T. P. Kicher and Mr. C. H. Wu)

The major work of the investigation of shell theories for anisotropic cylinders was completed during this report period. The following are brief descriptions of the work done:

(a) Formulation of boundary determinants for buckling: Three sets of differential equations are used for the analysis of shell buckling. They are based on the theories of Flugge, Donnell, and Timoshenko. Eight boundary conditions are considered; four simple support cases and four clamped end cases. For example:

Simple support SS I:

$$w = 0$$

$$M_x = 0$$

$$v \neq 0; \text{ or } T_x + P v_{,x} = 0$$

$$u \neq 0; \text{ or } N_x + \frac{T}{a} u_{,\theta} = 0$$

Clamped End CI:

$$w = 0$$

$$w_{,x} = 0$$

$$v \neq 0; \text{ or } T_x + P v_{,x} = 0$$

$$u \neq 0; \text{ or } N_x + \frac{T}{a} u_{,\theta} = 0$$

where $T_x = N_x + \frac{M_x}{a}$ is the Kirchoff boundary force. The other three cases can be obtained by setting $u = 0$, $v = 0$ or $u = 0$ and $v = 0$.

The following displacement modes are assumed:

$$u = \sum_{k=1}^8 U_k \sin \left(\frac{\lambda_k x}{a} + n\theta \right)$$

$$v = \sum_{k=1}^8 V_k \sin \left(\frac{\lambda_k x}{a} + n\theta \right)$$

$$w = \sum_{k=1}^8 W_k \cos \left(\frac{\lambda_k x}{a} + n\theta \right) \quad (1)$$

where λ_k , U_k , V_k , and W_k are, in general, complex values. The assumed displacement modes satisfy the differential equations but not the boundary conditions. In order to impose the boundary conditions, a special boundary determinant is formulated. This is done by expressing the following quantities in real and imaginary parts:

$$\begin{aligned}\lambda_k &= (\lambda_r + i\lambda_i)_k \\ W_k &= (W_r + iW_i)_k \\ U_k &= (U_r + iU_i)_k = (f_{ur} + if_{ui})_k W_k \\ V_k &= (V_r + iV_i)_k = (f_{vr} + if_{vi})_k W_k\end{aligned}\quad (2)$$

where the subscripts r and i denote the real and the imaginary part of the quantity, respectively.

The boundary determinant can now be obtained by substituting Eqs. (1), Eqs. (2), the strain-displacement relations, and the force-strain relations into the appropriate boundary conditions. For $w = 0$ the corresponding expressions for the boundary determinant are:

$$\sum_{k=1,3}^7 (\omega_k W_{srk} + \omega_{k+1} W_{cik+1}) = 0$$

$$\sum_{k=1,3}^7 (\omega_k W_{srk} + \omega_{k+1} W_{sik+1}) = 0 \text{ if } \lambda \text{ complex,}$$

or
$$\sum_{k=1}^8 \omega_k W_{crk} = 0$$

$$\sum_{k=1}^8 \omega_k W_{srk} = 0 \quad \text{if } \lambda \text{ real.}$$

Similar expressions can be obtained for $u=0$, $v=0$, $w_x=0$, $M_x=0$, $T_x + P v_x = 0$, and $N_x + \frac{T}{a} u_{,\theta} = 0$.

For any one of the eight cases of boundary conditions, a set of eight linear equations can be formed with eight undetermined coefficients, $\omega_1, \dots, \omega_8$. For nontrivial solution of ω_k , the boundary determinant must equal zero. The buckling loads and the corresponding circumferential wave number, n , for a cylinder with given length, geometry and material constants are those values which satisfy the vanishing of the boundary determinant.

(b) Computer programs: The computer programs for all three theories of shell buckling have been completed. After an extensive testing and study of the programs and the numerical results, it is found that the iteration procedures give very good results for the cases of radial pressure, torsion or a combination of both. Figure 13 shows the interaction curve for the combined radial pressure and torsion with 4(0, \bar{t} 22.5, 90) layer configuration, SS4 boundary condition, $L/R=2$ and $R/t=161.6$. Flügge's equations were used in this case. A similar curve was obtained for Donnell's theory. The differences between Flügge and Donnell are, in general, less than 1%. The interaction curve resembles the shape of a parabola. It is observed that the internal pressure tends to strengthen the cylinder while the external pressure tends to weaken the cylinder. Because of the unbalanced layer configuration, 4(0, \bar{t} 22.5, 90), the curve is slightly deviated from symmetry about the horizontal axis.

The results for axial compression obtained by the usual iteration procedures are merely the approximate solutions. The difficulty in obtaining an exact buckling load for the axial compression case comes from the basic characteristic of the critical loads. The critical loads, or the eigenvalues, for the axial compression case lie very closely together. By using the usual iteration procedures with coarse load increments, the computer program might miss the lowest eigenvalue and converge to a higher one. To overcome this difficulty it is necessary to use the approximate buckling load and a very fine load increment to pinpoint the lowest buckling load. This modified iteration procedure has been used with considerable degree of success. One major drawback of the procedure is the enormous amount of computer time consumed.

(c) Static responses: Equations and methods of solution for the static responses due to the surface loading were formulated. Computer programs have been completed. The numerical results are currently under study.

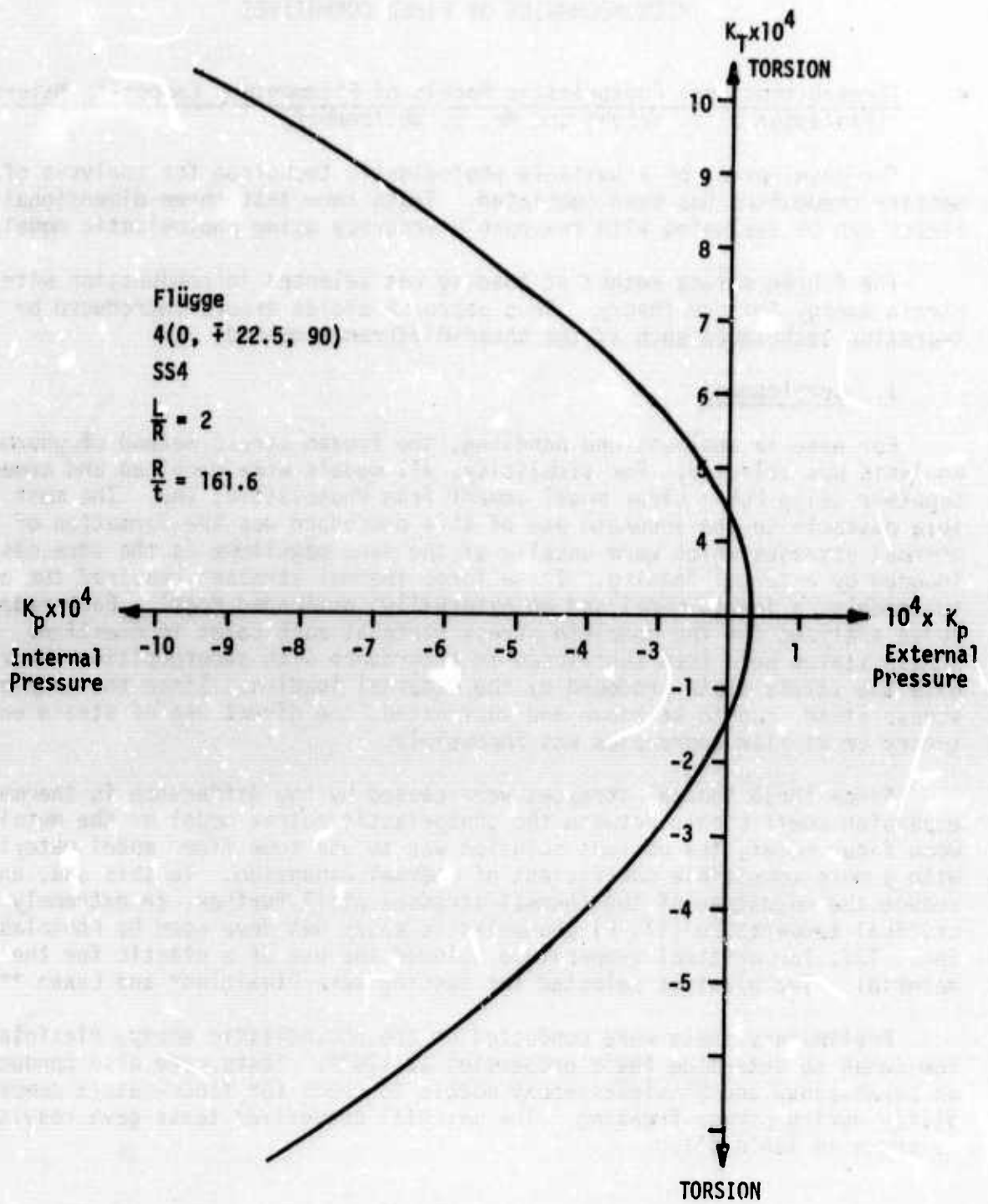


FIGURE 13. Radial Pressure and Torsion Interaction Curve

SECTION V

MICROMECHANICS OF FIBER COMPOSITES

A. Three-Dimensional Photoelastic Models of Filamentary Composite Materials (Professor D. K. Wright and Mr. D. Weitzenhof)

The development of a suitable photoelastic technique for analysis of filamentary composites has been completed. Tests show that three dimensional stress states can be evaluated with reasonable accuracy using photoelastic models.

The frozen stress method of loading was selected in conjunction with a strain energy failure theory. This approach avoids errors introduced by integration techniques such as the shear-difference method.

1. Development

For ease in analysis and handling, the frozen stress method of photoelastic analysis was selected. For simplicity, all models were machined and cemented together using PLM-1 clear model cement from Photolastic, Inc. The most formidable obstacle to the accurate use of this procedure was the formation of large thermal stresses which were usually of the same magnitude as the stresses induced by external loading. These large thermal stresses required the use of two models, a loaded model and an externally nonloaded model. Each model had to be analyzed for the complete stress state at each point in question. These stress states were then subtracted in accordance with superposition theory to give the stress state produced by the external loading. Since the complete stress state had to be known and subtracted, the direct use of strain energy theory or similar approaches was impossible.

Since these thermal stresses were caused by the difference in thermal expansion coefficients between the photoelastic matrix model or the metal or wood fiber model, the obvious solution was to use some fiber model material with a more compatible coefficient of thermal expansion. To this end, and to reduce the magnitude of the thermal stresses still further, an extremely low critical temperature (170°F) photoelastic epoxy was developed by Photolastic, Inc. This low critical temperature allowed the use of a plastic for the fiber material. Two plastics selected for testing were Plexiglas* and Lexan.**

Preliminary tests were conducted on the photoelastic epoxy, Plexiglas, and the Lexan to determine their properties at 170°F. Tests were also conducted on Lexan-epoxy and Plexiglas-epoxy models to check for fiber-matrix compatibility during stress-freezing. The material properties tests gave results as shown in Table III.

* Rohm & Haas Co.

** General Electric Co.

TABLE III
 PROPERTIES OF PHOTOELASTIC MATRIX MATERIALS

MATERIAL	YOUNG'S MODULUS	POISSON'S RATIO	COMMENTS
Photoelastic Epoxy	1890 PSI	.48	Full Deformation Reached In Six Minutes
Lexan	250 KSI	.35	Modulus Measured After 24 Hrs. At 170° F
Plexiglas	5 to 150 KSI	.40-.44	Excessive Creep at 170°F

The compatibility models (Figures 14-16) produced results as shown in Table IV. From these results, Lexan was selected as the fiber model material.

Tests 7 and 8 were then conducted to determine the relative values of the thermal and load-induced stresses. Figures 17-21 show configurations and fringe patterns produced. These tests demonstrated the feasibility of the method discussed.

TABLE IV
 TEST RESULTS ON VARIOUS COMPATIBILITY MODELS

TEST NO.	MODEL TYPE	LOADING	MAXIMUM SHEAR STRESS	COMMENTS
1	2-D LEXAN	THERMAL ONLY	2.9 PSI	FOR CONFIGURATION SEE FIGURE 14
2	2-D PLEXIGLAS	THERMAL ONLY	1.0 PSI	SEE FIGURE 14
3	2-D LEXAN	2.63# TENSILE PLUS THERMAL	8.5 PSI	SEE FIGURE 15
4	2-D PLEXIGLAS	2.63# TENSILE PLUS THERMAL	8.1 PSI	SEE FIGURE 15
5	3-D LEXAN	THERMAL ONLY	5.4 PSI	SEE FIGURE 16
6	3-D PLEXIGLAS	THERMAL ONLY	5.4 PSI	SEE FIGURE 16
7	3-D LEXAN	THERMAL ONLY	12.0 PSI	FOR CONFIGURATION SEE FIGURE 17. FOR FRINGE PATTERNS SEE FIG. 18 & 19
8	3-D PLEXIGLAS	152# COMPRESSIVE PLUS THERMAL	58.8 PSI	FOR CONFIGURATION SEE FIGURE 17. FOR FRINGE PATTERNS SEE FIG. 20 & 21

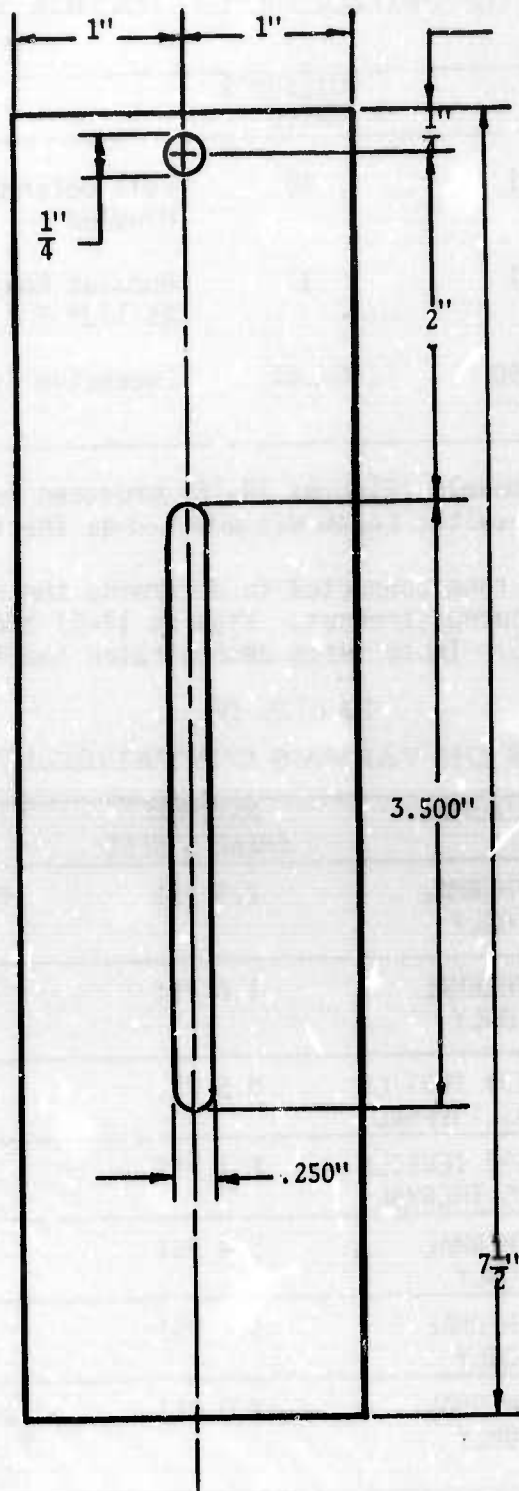


Figure 14. Model Type 1 - $\frac{1}{2}$ " Thick

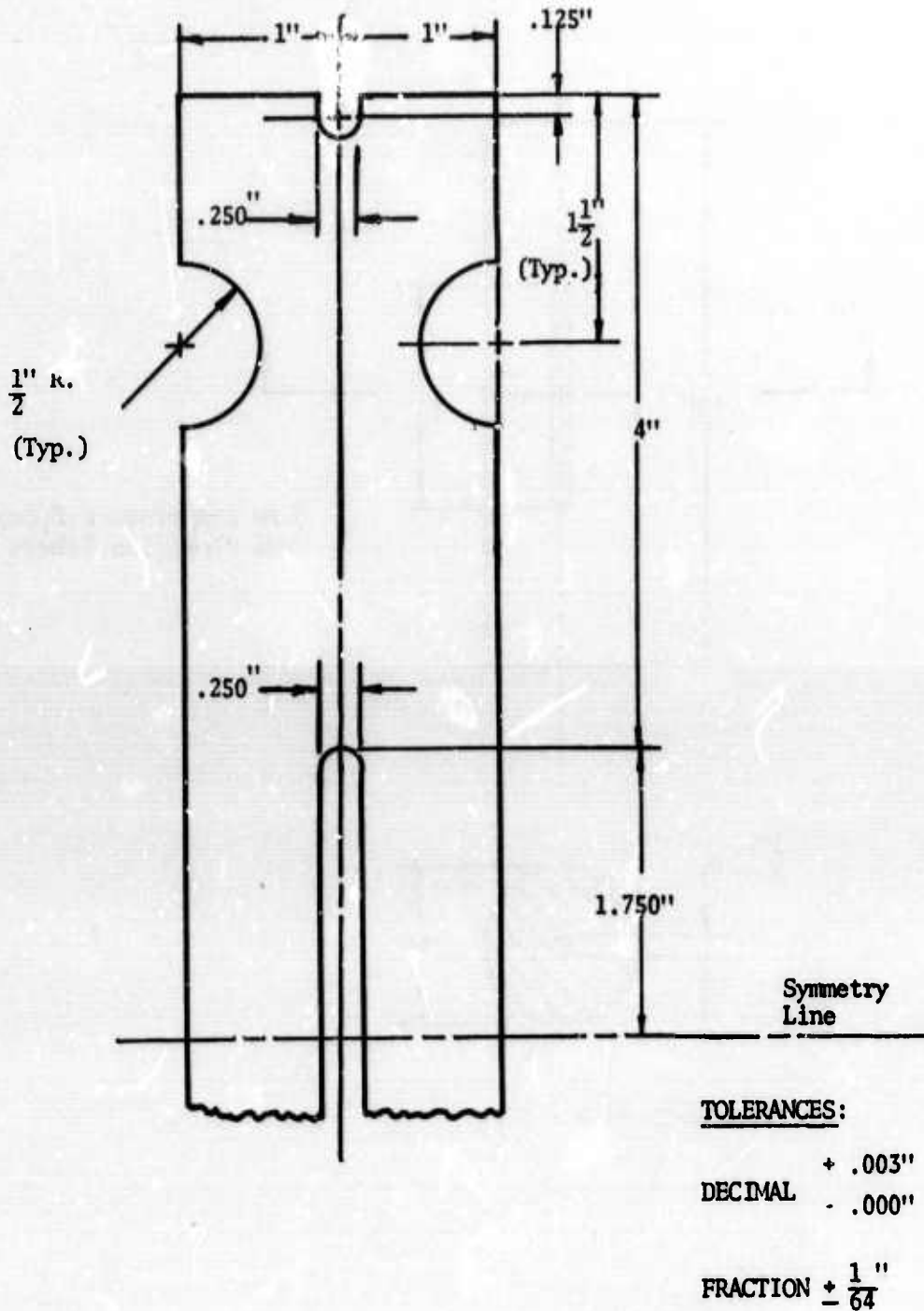
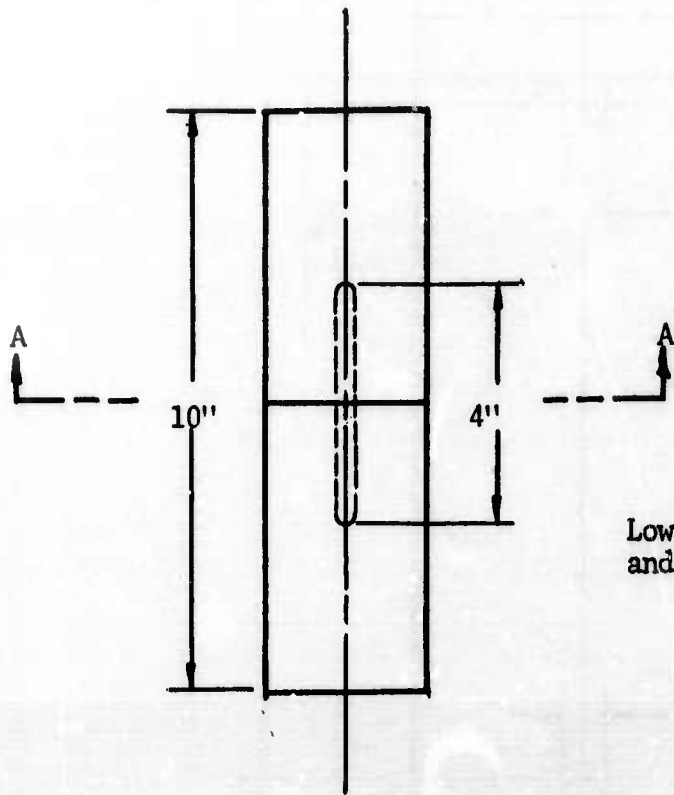
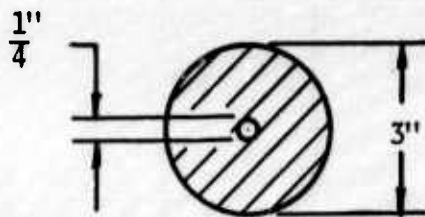


Figure 15. Model Type 2 - $\frac{1}{4}$ " Thick Full Scale

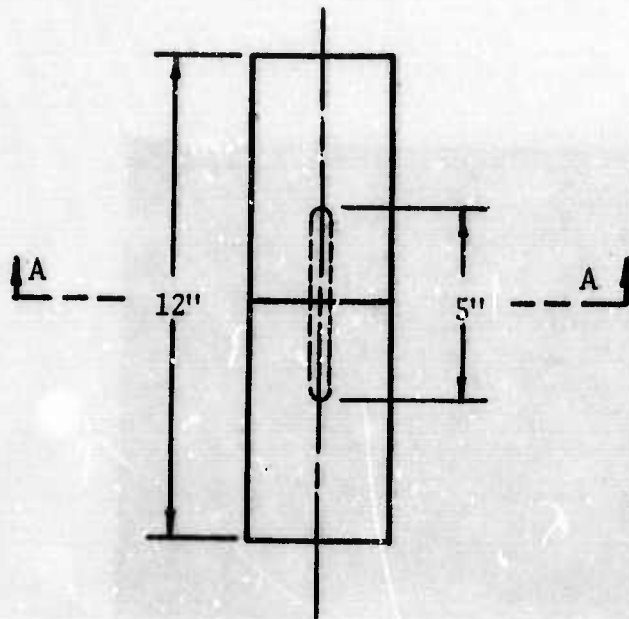


Low Temperature Epoxy, Lexan
and Plexiglas Fibers

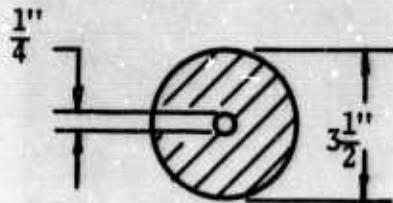


Section A - 4

Figure 16. Preliminary S. F. Test Model Sketches



Low Temperature Epoxy,
 Lexan Fibers



Section A - A

Figure 17. Load Test No. 1 Model Sketches



Figure 18. Thermal Stresses Near a
Fiber End in a Dark Field.
(1.25 Fringe)

N-23037

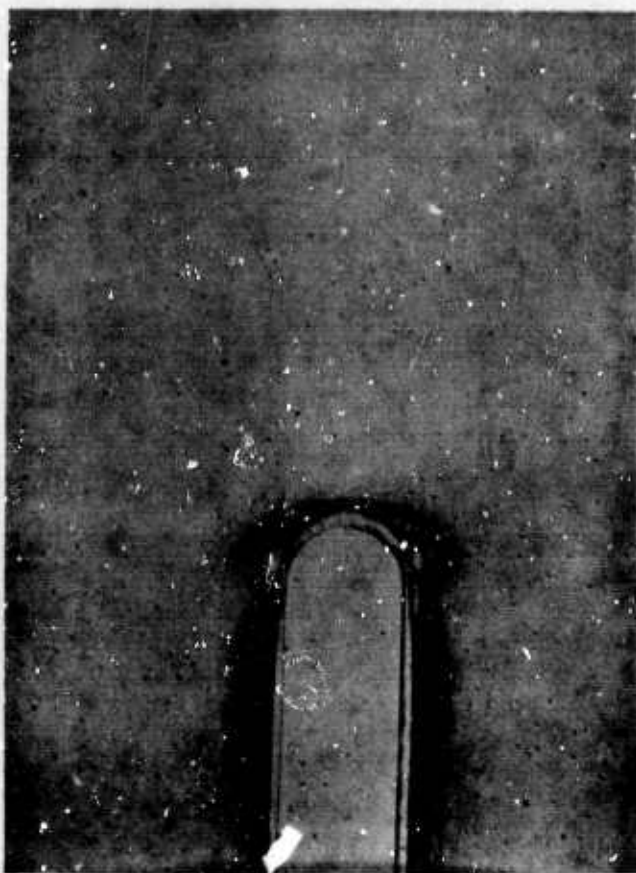


Figure 19. Thermal Stresses Near a
Fiber End in a Light Field.
(1.25 Fringes)

N-23038



Figure 20. Thermal and Mechanical Stresses Near a
Fiber End in a Dark Field.
(6.0 Fringes)

N-23039



Figure 21. Thermal and Mechanical Stresses Near a
Fiber End in a Light Field.
(6.0 Fringes)

N-23040

2. Strain Energy Analysis

The strain energy equations may be stated as follows (15):

$$U = \frac{1}{2} SE \quad \text{where}$$

$$S = \begin{bmatrix} \sigma_A & \tau_{AB} & \tau_{AC} \\ \tau_{BA} & \sigma_B & \tau_{BC} \\ \tau_{CA} & \tau_{CB} & \sigma_C \end{bmatrix}$$

and E is the equivalent strain matrix. Eliminating the hydrostatic stress component which does not contribute to failure, and realizing that

$$E = \frac{S}{E}$$

where E is Young's Modulus we obtain

$$U' = \frac{(\sigma_1 - \sigma_2)^2 + (\sigma_2 - \sigma_3)^2 + (\sigma_3 - \sigma_1)^2}{12G},$$

$$\text{where } G = \frac{E}{2(1+\mu)}.$$

$$\text{In simple tension, } U' = \frac{2\sigma_1^2}{12G} = \frac{\sigma_0^2}{6G}.$$

Thus, failure will occur when

$$(\sigma_1 - \sigma_2)^2 + (\sigma_2 - \sigma_3)^2 + (\sigma_3 - \sigma_1)^2 = 2\sigma_0^2.$$

Using photoelastic relationships, this reduces to

$$\sigma_{\text{eff}}^2 = \frac{1}{2} f^2 \left| \frac{3}{\Sigma} \left(\frac{N}{t} \right)^2 \left(1 + \frac{1}{2} \sin^2 2\phi \right) \right|$$

where f is the stress-fringe constant for the particular material; t is the size of the cube; N is the fringe number in that view of the cube; and ϕ is the isoclinic angle in that view of the cube.

Since $(\sin^2 2\phi)$ is the same for $(+\phi +90^\circ)$, the orientation of the cube need not be known. The only requirement is that all three directions be viewed and the position of the cube in the model be known.

3. Technique Application

To demonstrate the technique developed above, several fiber-fiber and fiber-void interaction models have been fabricated and analyzed. A typical model configuration and load application is shown in Figure 22. Figure 23 shows typical slices from the loaded and unloaded models in the dark field polariscope. As can be seen, the slice from the externally nonloaded model has almost no indication of stress whereas the loaded model slice shows approximately one and one-half fringes. Both slices are 0.100 inches thick. The stresses present in the Lexan fibers are caused by the initial forming process and have no meaning in the model. Thus, the thermal stresses, which were the greatest obstacle to a satisfactory analysis, can now be assumed very small and ignored. The cubes shown were analyzed using the strain energy theory discussed above.

4. Results and Conclusions

The results of the analysis of these cubes according to the strain energy theory are shown in Figure 24. Other configurations including voids will also be analyzed and the values of effective stress compared. These experimental values will also be compared to theoretical values obtained by J. F. Stevenson in his work, Discrete-Element Microstress Analysis of Unidirectional Fiber Composites.

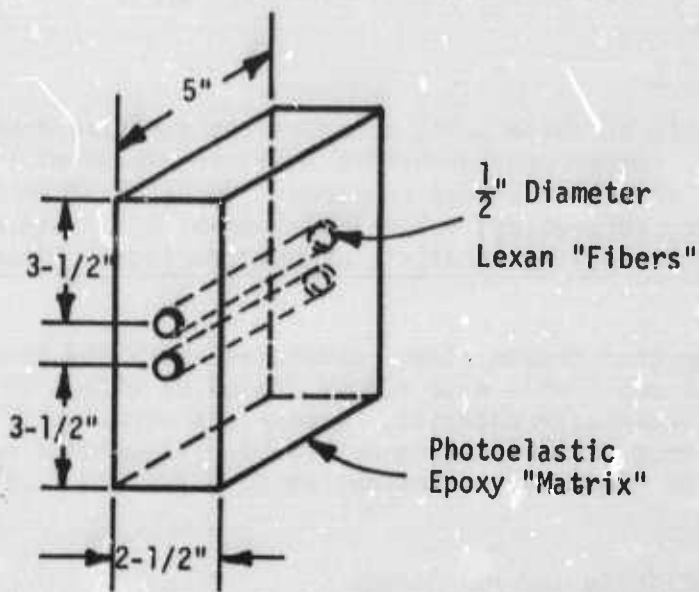
Results thus far indicate that frozen stress photoelasticity may be used successfully to determine with reasonable ease stress states or effective stresses within a filamentary composite material. A complete report will be forthcoming in the form of a thesis submitted in partial fulfillment of the requirements for the degree of Doctor of Philosophy at Case Western Reserve University.

B. Scattered Light Photoelasticity and Holography (Professor J. Cannon, Mr. C. Choi, Mr. P. Shankar)

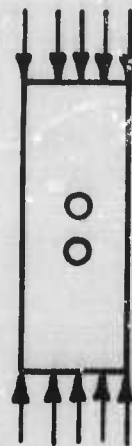
1. Scattered Light Photoelastic Studies

The photoelastic studies of fiber reinforced composite materials to present have been carried out by the frozen stress method with one, two, or few reinforcing fibers. The frozen stress method encounters a serious difficulty of large thermal stress induced in the model due to the mismatch of the thermal properties of matrix and fiber materials during the stress freezing cycle. It is believed that the use of two identical models (one with load stresses, one without) would eliminate this difficulty.

However, there still remains an uncertainty as to the possibility of fabricating two identical models with multiple reinforcing fibers. One other uncertainty is regarding the accuracy of the results with two models when thermally induced stress is much greater than the stresses due to externally applied load.



Configuration



Total Load ~ 250 lb.
Load Application

Figure 22. Model Configuration and Load Application

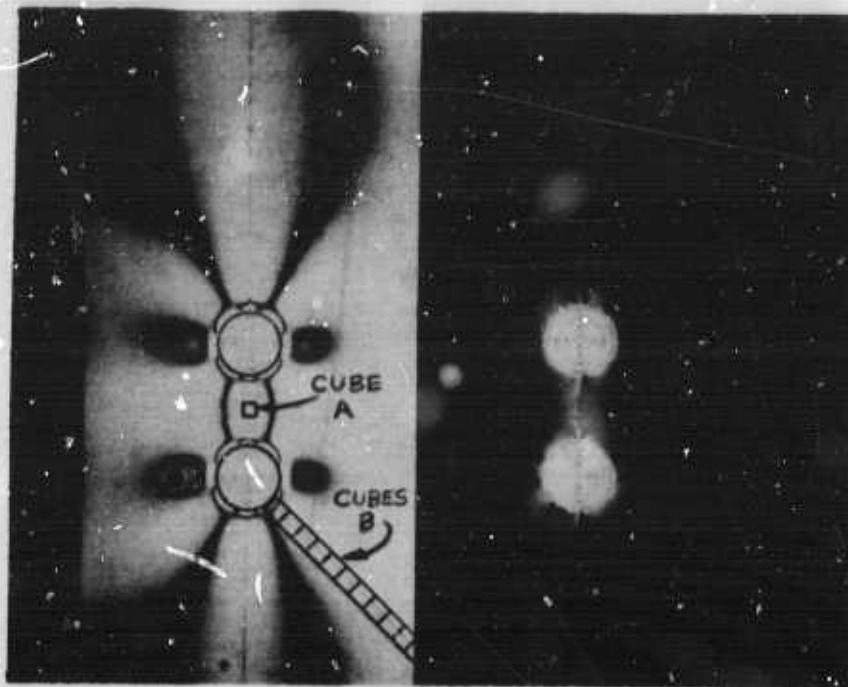


Figure 23. Dark Field View of Model Slices.

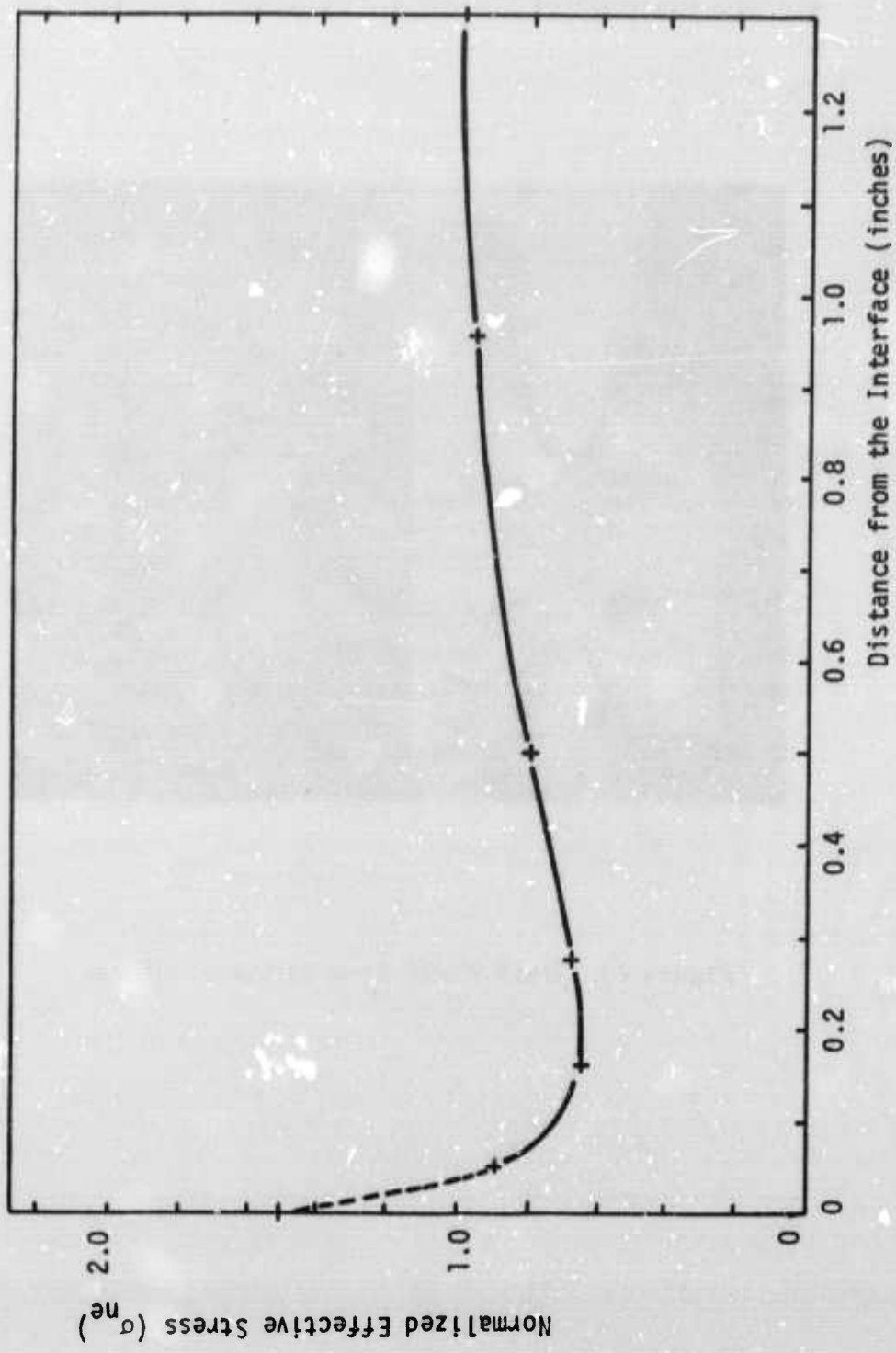


Figure 24. Normalized Effective Stress

An extensive study of the properties of transparent plastics show that it is not feasible to obtain matrix and fiber materials with matching thermal properties and still be able to simulate the ratios of the mechanical properties of fiber to matrix of an actual composite material.

Thus, the live-load approach to the photoelastic analysis of the fiber reinforced composite materials was adopted.

Selection of Photoelastic Model Materials

The materials shown in Table V were selected as possible model materials. An appropriate combination of the matrix and fiber materials from the table can approximate the ratio of the moduli of elasticity of actual fiber reinforced composite material.

TABLE V

Possible Model Material			
Matrix Material	Thermal Expansion Coefficient ($10^{-5}/^{\circ}\text{F}$)	Modulus (10^5 psi)	Strength (10^3 psi)
<u>Polyesters</u>			
Cast Rigid	3.7	1.5 - 6.5	4 - 10
Cast Flexible	2.8 - 5.5	.001 - .10	1 - 8
<u>Epoxy</u>			
Cast Rigid	3.3	4.0 - 5.0	6 - 9
Cast Flexible	3.0 - 10.0	.01 - 3.5	2.10
<u>Ionomers</u>			
	6.7	.2 - .6	3.5 - 5.5
Fiber (or Rod) Material	Thermal Expansion Coefficient ($10^{-5}/^{\circ}\text{F}$)	Modulus (10^5 psi)	Strength (10^3 psi)
Acrylic	5.0 - 9.0	3.5 - 5.0	8 - 11
Polycarbonate	3.75	3.45	9.5
Aluminum	.125	106	60

An attempt was made to determine the fringe definition characteristics of epoxy and polyester resins of varying stiffness, from rigid to flexible. Results of the experiment show that polyesters possess superior fringe definition characteristics for scattered-light compared to epoxy. However, polyesters exhibit considerable amounts of creep. Typical scattered-light

fringes of polyester and epoxy are shown in Figure 25. The model is a disk under diametral compression.

Epoxy and polyester resins used are as follows:

Epoxy

- Araldite 6020 (Resin)*
- Araldite 508 (Resin)
- Araldite 956 (Hardener)

Polyester

- Cadco Resin (Rigid)#
- Laminac EPX-126-3** (Flexible Resin)
- Laminac 4134** (Flexible Resin)
- MEK Peroxide (Hardener)

Compositions and stress fringe values are shown in the following Tables:

TABLE VI

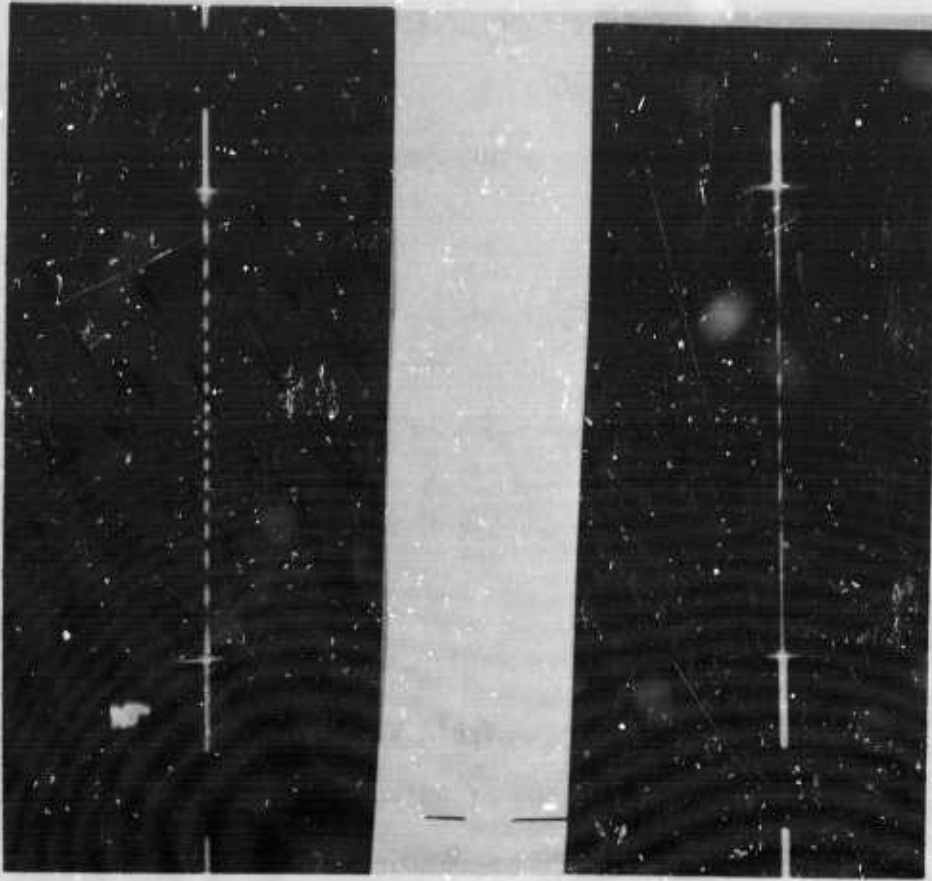
Photoelastic Calibration Constants

Sample	f(lb/fringe-in)	Sample	f(lb/fringe-in)
Epoxy No. 3	93.9	Polyester No. 8	6.6
Epoxy No. 4	28.9	Polyester No. 10	110.9
Epoxy No. 5	109.1	Polyester No. 11	132.2
Epoxy No. 6	100.1	Polyester No. 12	157.0
Epoxy No. 7	109.9	Polyester No. 13	128.7
		Polyester No. 14	176.0
		Polyester No. 15	105.9
		Polyester No. 16	118.7

*Ciba Products Company

**American Cynamid Company

#Cadillac Plastic and Chemical Company



(a) Polyester (#13)

(b) Epoxy (#7)

Figure 25. Scattered Light Fringes for Disks of Polyester and Epoxy Under Diametral Compression.

Table VII

Composition of Epoxy Samples

Sample	Araldite 6020 (pbw) ¹	Araldite 508 (pbw)	Araldite 956 (pbw)
Epoxy No. 3	100	100	78
Epoxy No. 4	100	150	50
Epoxy No. 5	100	50	40
Epoxy No. 6	100		20
Epoxy No. 7	100	33	33

¹ Parts by weight

Table VIII

Composition of Polyester Samples

Sample	Cadillac (pbw)	Laminac EPX-126-3 (pbw)	Laminac 4134 (pbw)	MEK Peroxide (drops/oz)
Polyester No. 8		100		3
Polyester No. 9		100	20	7.5
Polyester No. 10	100			6
Polyester No. 11	100	30		9
Polyester No. 12	100		30	9
Polyester No. 13	100	20		8
Polyester No. 14	100		20	8
Polyester No. 15	100	10		7
Polyester No. 16	100		10	7

Casting of Flat Photoelastic Models

A number of flat fiber (or rod) reinforced models using the materials listed were cast. Two major difficulties encountered in the casting process were voids (or air bubbles) and residual stresses in the model.

The voids problem was solved by following the mixing procedure similar to the method devised by D'Agostino et al. (Proc. SESA V. XII, No. 2, 1955) The procedure involves the following steps:

After weighing (or measuring) the resin it was poured into a rubber sack; if more than one resin was used they were mixed together.

The rubber sack was suspended until the bubbles rose out of the resin. Immersing the rubber sack in hot water to reduce the viscosity of the resin or placing it in a vacuum helps to speed up the process somewhat. It took a minimum of four days for epoxies and one day for the polyester resin.

The hardener for epoxy was similarly prepared in advance in a hypodermic syringe.

The rubber sack was then tied below the liquid level and hardener was injected into the resin using hypodermic syringe and needle. The rubber sack was tied again below the needle hole and mixing was done by kneading the rubber sack until the homogeneous mixture was obtained.

Considerable reduction of residual stress due to casting was obtained by following Edelman's casting procedures. Edelman's procedures are:

- a. Cool the assembled mold to a low temperature (approximately 30°F) and store at that temperature for 24 hours.
- b. Pour the resin and hardener mixture into the mold and cure at the low temperature--for 24 hours.
- c. Raise the temperature at a rate of 5° per hour to room temperature.
- d. Remove the cast model from the mold after a 24-hour cure at room temperature.

A Live-Load Loading Frame Design

The design of a live-load loading frame has been completed and fabrication is proceeding. The loading-frame as designed will have the following capabilities:

- a. Maximum axial force (tension or compression) 2,000 pound and maximum torque of 3,000 inch-pound. The axial force and torque can be applied independently or simultaneously through an Axial-Force-Torque Hydraulic Actuator.
- b. Maximum size of model which can be accommodated is 10-inch diameter by 12-inch length.

- c. Model can be rotated about two axes and translated along two perpendicular directions.
- d. Two directions of observation are possible.

2. Holography Studies

Holographic techniques provide a very sensitive means of measuring displacements and stresses. In the field of Applied Mechanics this opens up the possibility of experimental means to directly support or contradict various hypotheses. Efforts were started to set up a system to produce holograms which are intended to supplement the scattered light effort.

- a. Optical Fixtures: To hold various optical elements like lenses, beam splitters etc. optical fixtures were designed and machined. Each was provided with various motions for positioning and a heavy base for stability.
- b. Holographic Table: This is a heavy base on which the entire set-up rests. This should have good damping characteristics and rigidity with respect to bending to avoid modal vibrations. For these reasons a steel table was bypassed in favor of a 7' x 4' x 0.5' reinforced concrete table which was designed and fabricated.
- c. Table Suspension: Various means of supporting the 1600 lb. concrete table to isolate it from building vibrations were experimentally evaluated. These included heavy steel springs and cement blocks followed by air tubes. Each was studied for frequency response and finally air tube suspension was found adequate.
- d. Light Source: For reasons of intensity and purity of wavelength a laser is the most suitable light source. The assembly of a laser starting from the 50 mw plasma tube and associated high quality optical elements is almost complete. Various precision mounts for the mirrors, prisms and different clamps for support and precision alignment of the plasma tube have been machined and mounted on a heavy I beam. A six kilovolt power supply with a laser self-starting feature has also been assembled. Work is in progress, with the help of a small laser, to get precision alignment and lasing action.

C. Discrete-Element Microstress Analysis of Unidirectional Fiber Composites (Professor T. P. Kicher and Dr. J. F. Stevenson)

A formulation for a displacement-method discrete element for use in two-dimensional, linear microstress analyses of unidirectional fiber composite materials that experience deformation in a plane normal to the direction of the fibers has been completed. The discrete element itself is capable of modeling a rectangular region of matrix that contains the entire cross section of a fiber. The displacement state within an element is expressed in terms of nodal displacement parameters and local coordinate functions which are defined to satisfy the displacement-equilibrium equations and stress-matching conditions

at the fiber-matrix interface. Displacement boundary conditions that the local coordinate functions must satisfy are chosen in such a manner that inter-element displacement continuity at the common edge of contiguous elements can be assured. Numerical solutions were obtained for ten problems that consist of assemblages of one or more of the following plane strain elements: square element with a centered circular fiber, square element with an off-centered circular fiber, square element with no fiber, and square element with a centered circular "hole" (i.e., a highly flexible fiber). The solution for each problem is generated by direct minimization of the potential energy of the assemblage. The Fletcher-Reeves algorithm coupled with a scaling transformation is used to carry out the minimization.

Details of this work can be found in the Ph.D. thesis of J. F. Stevenson submitted to Case Western Reserve University. A separate topical report will not be issued but a condensed version of the paper has been submitted for publication in an archive journal.

D. Application of the Theory of Physically Nonlinear Elastic Solids to Composite Materials
(Professor Sendeckyj)

The investigation of stress and strain concentration factors due to inclusions of various shapes in a physically nonlinear matrix, reported in Reference 5, has been continued with emphasis being placed on developing an analysis method that may be extended to nonlinear solids for solving linearly elastic inclusion problems. Considerable success has been achieved in this respect. The general solution of the elastic curvilinear inclusion problem has been found in the case of antiplane, or longitudinal, shear deformation. This result has been used to discuss the longitudinal shear behavior of filamentary composites in References 5 and 16. The general solution has also been used to solve the antiplane deformation problem of a filamentary composite with randomly spaced fibers (summarized in Sections 1 and 2 below). In the case of plane deformation, the general functional form of the solution for an elastic curvilinear inclusion has been found (summarized in Section 3). The multiple circular inclusion problem in plane elastostatics is presently being worked on, with limited results being presented in the next chapter (Section V E of this report). Finally, the solution methods for nonlinear problems have been reconsidered and apparently a promising approach has been found (Section 4 below).

1. Multiple Circular Inclusion Problems in Longitudinal Shear Deformation

Consider a homogeneous unbounded matrix containing N circular cylindrical inclusions with centers at $z = a_j$ (see Figure 26). Let the radius of the i^{th} inclusion be R_i and assume that all the inclusions have the same shear modulus. Let subscripts 1 and 2 on elastic field quantities refer to the matrix and inclusions, respectively. Let the stress state at infinity be $\sigma_{xz}^{\infty} = 1$, $\sigma_{yz}^{\infty} = 0$. It is required to determine the elastic fields near the inclusion.

Using the notation of Reference 5, it is readily established that the

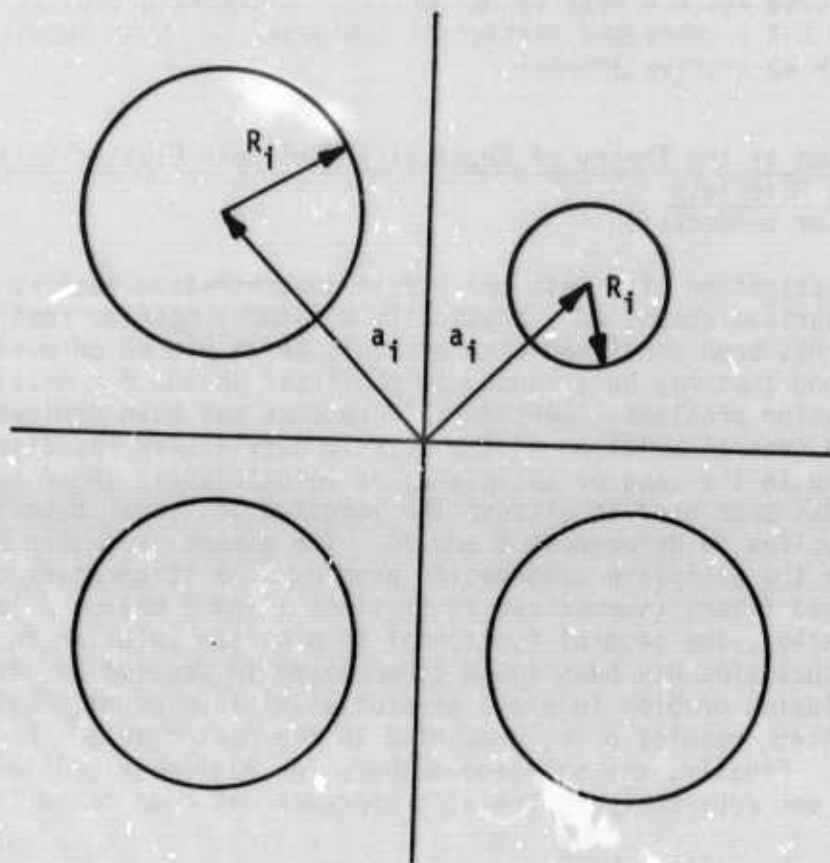


Figure 26. Homogeneous Unbounded Matrix Containing Circular Inclusion

complex potentials for the problem are

$$F_1(z) = z - \sum_{m=1}^{\infty} K^m \sum_{n=1}^{P_m} \frac{C_{m,n}}{z - \zeta_{m,n}}, \quad (1)$$

$$F_2(z) = (1+K) \left\{ z - \sum_{m=1}^{\infty} K^m \sum_{n=1}^{P_m} \frac{C_{m,n}}{z - \zeta_{m,n}} \right\} \quad (2)$$

where

$$P_m = N(N-1)^{m-1} \quad (3)$$

$$C_{1,n} = R_n^2, \quad \zeta_{1,n} = a_n \quad (n = 1, 2, \dots, N) \quad (4)$$

and, in general,

$$\zeta_{m,n} = a_i + R_i^2 [\bar{\zeta}_{m-1,k} - \bar{a}_i]^{-2} \quad (5)$$

$$C_{m,n} = \bar{C}_{m-1,k} R_i^2 [\bar{\zeta}_{m-1,k} - \bar{a}_i]^{-2} \quad (6)$$

if $|\zeta_{m-1,k} - a_i| \geq R_i$; otherwise the terms are not computed. The calculations indicated by (5) and (6) are to be carried out for all $m; k=1, 2, \dots, P_{m-1}; n = 1, 2, \dots, P_m$; and $i = 1, 2, \dots, N$. The prime on the summation symbols in (2) denotes that terms that are singular within the inclusion under consideration are to be omitted from the sum. A detailed derivation of this result is given in Ref. 17. The stresses may be computed from (1) and (2) by using

$$\sigma_{zx} - i\sigma_{yz} = \frac{dF}{dz}$$

The structure of the solution is surprisingly simple. The complex potentials $F_i(z)$ are singular at the points $z = \zeta_{m,n}$. The points $z = \zeta_{1,n}$ are the positions of the centers of the inclusions; while, the points $z = \zeta_{m,n}$ ($m \geq 2$) are the result of successive inversions of $z = \zeta_{1,n}$ with respect to the inclusion boundaries, which is the operation indicated by (5). The coefficients $C_{m,n}$ ($m \geq 2$) are products of squares of distances from the singular points to the centers of the inclusions in which the singularities occur.

The general solution, eqs. (1) and (2), can be used to develop estimates of the effective moduli of filamentary composites. This is done in the next section.

2. Effective Shear Modulus

In a fundamental paper, Hill (18) developed exact expressions for the effective moduli of multiphase composites. In the case under consideration, the pertinent expression may be written as

$$\mu = \mu_1 + v B(\mu_2 - \mu_1) \quad (7)$$

where μ is the longitudinal shear modulus; v is the concentration, or volume fraction, of the fibers; and B is the average strain concentration in the fiber. The use of (7) requires knowledge of the average strain concentration factor in the fiber, which may be obtained from (2) as follows: the stresses within the typical inclusion being considered are

$$\sigma_{xz} - i\sigma_{yz} = (1+K) \left\{ 1 + \sum_{n=1}^{\infty} K^n \frac{P_m}{\Sigma'} \frac{C_{m,n}}{[z - \zeta_{m,n}]^2} \right\} \quad (8)$$

Since the singularities are outside the inclusion, the stresses can be expanded in a Laurent series about the center of the inclusion to give

$$\sigma_{xz} - i\sigma_{yz} = (1+K) \left\{ 1 + \sum_{m=1}^{\infty} K^m \frac{P_m}{\Sigma'} \frac{C_{m,n}}{\zeta_{m,n}^2} \left[1 + \frac{2z}{\zeta_{m,n}} + \dots \right] \right\}.$$

The terms with z^k yield stresses that depend on cosine and sine of $k\theta$. Upon averaging, these give a zero contribution. Thus, we get

$$\tau_{xz} - i\tau_{yz} = (1+k) \left\{ 1 + \sum_{m=1}^{\infty} K^m \frac{P_m}{\Sigma'} \frac{C_{m,n}}{\zeta_{m,n}^2} \right\} \quad (9)$$

for the averaged complex stress combination.

For a regular array of fibers, it can be shown after some rather tedious computations that

$$\tau_{xz} = (1+K) \left\{ \frac{1}{1-KS_2} + \frac{3K^2S_4^2}{(1-KS_2)^2 [(4a^2)^2 - S_4^2 K^2]} \right\} \quad (\text{cont'd})$$

$$\begin{aligned}
& + \frac{5K^2 S_6^2}{(1-KS_2)^2 [(4a^2)^4 - \zeta_6^2 K^2]} \\
& + \frac{7K^2 S_8^2}{(1-KS_2)^2 [(4a^2)^6 - S_3^2 K^2]} + \dots \} , = (1+K) A \quad (10)
\end{aligned}$$

where

$$S_n = \sigma_n / 4a^2 \quad (11)$$

and

$$\sigma_{2k} = \sum_{\substack{n=-\infty \\ m=-\infty}}^{\infty} \frac{1}{[m+n c e^{i\alpha}]^{2k}} \quad (12)$$

where c and α are parameters defining the regular array. These are defined in Figure 27. The prime denotes that the summation is to be carried out for all integer values of n and m with the exclusion of $n=m=0$.

Using (1) to estimate the average strain concentration factor for the fibers, we get

$$u = u_1 \{1 + 2\nu KA\} \quad (13)$$

for the effective shear modulus. This expression yields results in excellent agreement with numerically obtained graphs given in References 19 and 20.

3. Plane Deformation - Curvilinear Inclusion Problem

Some preliminary results on the curvilinear inclusion problem in plane elastostatics were presented in Reference 5. The present section deals briefly with results generated since Reference 5. Since the notation that is used can be found in any modern text on the theory of elasticity, it will not be given here.

Consider an elastic matrix containing a single curvilinear inclusion whose boundary is given parametrically by

$$z = \omega(\zeta) , \quad |\zeta| = 1. \quad (14)$$

Letting subscripts 1 and 2 on elastic quantities refer to the matrix and inclusion respectively, the boundary conditions corresponding to a perfect bond at the interface are

$$u_1 + iv_1 = u_2 + iv_2 \quad \text{for } |\zeta| = 1. \quad (15)$$

$$\sigma_{\rho\rho 1} - i\sigma_{\rho\theta 1} = \sigma_{\rho\rho 2} - i\sigma_{\rho\theta 2}$$

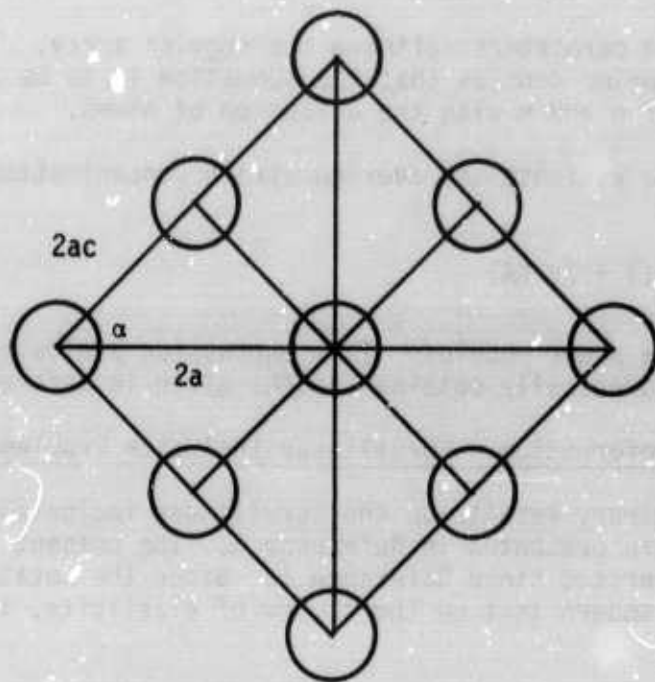


Figure 27. Regular Array of Circular Fibers

The complex potentials $\phi(z)$ and $\psi(z)$ satisfying (15) are

$$\begin{aligned} \phi_1(z) = \phi_1(\zeta) = f(z) - \frac{\beta - \alpha}{1 - \beta} \frac{\omega(\zeta)}{\omega'(\zeta)} \frac{d}{d\zeta} \bar{f}[\Omega(\zeta)] \\ - \frac{\beta - \alpha}{1 + \beta} \bar{h}[\Omega(\zeta)] , \end{aligned} \quad (16)$$

$$\begin{aligned} \psi_1(z) = \psi_1(\zeta) = \frac{2\beta}{1 - \beta} \frac{\Omega(\zeta)}{\omega'(\zeta)} \frac{d}{d\zeta} f[\omega(\zeta)] \\ + \frac{\beta - \alpha}{1 - \beta} \frac{\Omega(\zeta)}{\omega'(\zeta)} \frac{d}{d\zeta} \frac{\omega(\zeta)}{\Omega'(\zeta)} \bar{f}[\Omega(\zeta)] \\ + \frac{\alpha + \beta}{1 - \beta} \bar{f}[\Omega(\zeta)] + \frac{\beta - \alpha}{1 + \beta} \frac{\Omega(\zeta)}{\omega'(\zeta)} \frac{d}{d\zeta} \bar{h}[\Omega(\zeta)] , \end{aligned} \quad (17)$$

$$\phi_2(z) = \frac{1 + \alpha}{1 - \beta} f(z) , \quad (18)$$

$$\psi_2(z) = \frac{1 + \alpha}{1 + \beta} h(z) , \quad (19)$$

where

$$\begin{aligned} \alpha &= [i(\kappa_1 + 1) - (\kappa_2 + 1)] / [\Gamma(\kappa_1 + 1) + \kappa_2 + 1] , \\ \beta &= [\Gamma(\kappa_1 - 1) - (\kappa_2 - 1)] / [\Gamma(\kappa_1 + 1) + \kappa_2 + 1] , \end{aligned} \quad (20)$$

$$\Gamma = \mu_2 / \mu_1$$

and

$$\Omega(\zeta) = \omega(1/\zeta) . \quad (21)$$

General solution (16-19) can be readily specialized for particular combinations of material properties. For a cavity or an inclusion of vanishing rigidity, one gets

$$\begin{aligned} \phi(z) &= f(z) - \bar{h}(1/\zeta) , \\ \psi(z) &= h(z) - \bar{f}(1/\zeta) + \frac{\Omega(\zeta)}{\omega'(\zeta)} \left[\frac{d}{d\zeta} \bar{h}(1/\zeta) - f'(\zeta) \right] . \end{aligned} \quad (22)$$

For a rigid curvilinear inclusion, $\Gamma = \infty$ and the general solution reduces to

$$\phi(\zeta) = f(\zeta) + \frac{1}{\kappa} \bar{h}(1/\zeta) ,$$

$$\psi(\zeta) = h(\zeta) + \bar{f}(1/\zeta) - \frac{\Omega(\zeta)}{\omega^*(\zeta)} \left[\frac{1}{\kappa} \frac{d}{d\zeta} \bar{h}(1/\zeta) + f'(\zeta) \right] . \quad (23)$$

A more detailed treatment of these results can be found in Reference 21.

Some preliminary results on the application of the general solution to composites are reported in the section by G. P. Sendeckyj and I. W. Yu in this report.

4. Nonlinear Antiplane Deformation

During the period covered by this report, four methods of solving physically nonlinear elasticity problems were examined, namely,

- 1) successive approximations,
- 2) perturbation series,
- 3) series in terms of trigonometric functions, and

4) series in terms of inverse powers of the radial coordinate. Of these methods, the fourth seems most promising; but only partial results are available at this time. Of the other three methods, expansion of the displacements in terms of trigonometric series in the θ direction, with unknown coefficients depending on the radial variable, leads to an infinite system of badly coupled nonlinear differential equations, which cannot be solved. The successive approximations technique is extremely tedious to use, while the perturbation series approach is not much better. Future work in this area will be centered on use of the fourth method.

E. Multiple Circular Inclusion Problem in Plane Elastostatics (Professor G. P. Sendeckyj and Mr. I. W. Yu)

Recent technical literature abounds with solutions of problems of plane elastostatics for regions with circular boundaries. Yet, upon scanning the literature, it is readily seen that very few solutions are available for the case of more than one elastic inclusion. These solutions are restricted to special geometric configurations of the inclusions. The present work is an attempt to generate analytical solutions for the case of randomly spaced elastic circular inclusion in a solid undergoing plane deformation. The approach used to solve the corresponding problem for antiplane deformation (see Section V D in this report) is being used. At present only limited preliminary results are available. These are summarized below.

1. Two Circular Cavities on x-axis

Consider an elastic slice weakened by two circular cavities of unit radius. Let the centers of the cavities be put at the points $x = \pm a$, $y = 0$ ($a > 1$). Let the applied stresses at infinity be specified as

$$\sigma_{xx}^{\infty} = -1, \sigma_{yy}^{\infty} = 1, \sigma_{xy}^{\infty} = 0. \quad (1)$$

It is required to determine the elastic fields in the vicinity of the cavities.

Using the standard notation of elasticity theory, the complex potentials corresponding to (1) are

$$\phi_{\infty}(z) = 0, \quad \psi_{\infty}(z) = z. \quad (2)$$

Upon using (2) as the input to the general form of the solution of a circular cavity (see Section V D in this report), it follows that

$$\phi(z) = -\frac{1}{z-a} + \frac{1}{z+a}, \quad (3)$$

$$\psi(z) = z - a \left[\frac{1}{(z-a)^2} - \frac{1}{(z+a)^2} \right] - \left[\frac{1}{(z-a)^3} + \frac{1}{(z+a)^3} \right]. \quad (4)$$

Equations (3) and (4) constitute the first approximation of the desired solution. The stresses due to these potentials satisfy the boundary conditions only approximately. An improved approximation follows upon connecting (3) and (4) by using the general form of the solution. The second approximation can be written as

$$\begin{aligned} \phi(z) = & -\frac{1}{z-a} - \frac{1}{z+a} + \left[\frac{1}{b_0^2} - \frac{3}{b_0^4} \right] \left[\frac{1}{(z-a+1/b_0)} + \frac{1}{(z+a-1/b_0)} \right] \\ & + \left[-\frac{a}{b_0^4} + \frac{3}{b_0^5} \right] \frac{1}{(z-a+1/b_0)^2} + \frac{1}{(z+a+1/b_0)^2} \\ & - \frac{1}{b_0^6} \frac{1}{(z-a+1/b_0)^3} + \frac{1}{(z+a-1/b_0)^3}, \end{aligned} \quad (5)$$

$$\begin{aligned} \psi(z) = & z - a \frac{1}{(z-a)^2} - \frac{1}{(z+a)^2} - \frac{1}{(z-a)^3} + \frac{1}{(z+a)^3} \\ & + \frac{1}{b_0^2} \frac{1}{(z-a+1/b_0)^2} - \frac{1}{(z+a-b_0)^2} \\ & - \frac{1}{b_0^2} \frac{1}{(z-a+1/b_0)} + \frac{1}{(z+a-1/b_0)} \end{aligned}$$

(cont'd)

$$\begin{aligned}
& + \frac{1}{b_0^2} - \frac{3a}{b_0^4} \frac{1}{(z+a-1/b_0)^2} + \frac{1}{(z-a+1/b_0)^2} \\
& + \frac{1}{2b_0^2} \frac{1}{(z-a+1/b_0)^3} + \frac{1}{(z+a-1/b_0)^3} \\
& + \frac{3}{2b_0^4} \frac{1}{(z-a+1/b_0)^4} - \frac{1}{(z+a-1/b_0)^4} \tag{6}
\end{aligned}$$

where

$$b_0 = 2a . \tag{7}$$

The third approximation was also generated; but the structure of the general solution is still not clear. A fourth approximation is being generated at the present time. This should make it possible to guess the structure of the general solution. Once this solution is known, generalization to a randomly perforated slice is expected to be straightforward.

F. Structural Analysis for Laminated Fiber Composite Structures (Prof. L. A. Schmit and Mr. S. N. Patnaik)

Laminated fiber composite plates and shells composed of a collection of highly orthotropic lamina with noncoincident laminate axis make the total structure anisotropic and heterogeneous through the thickness. Current analysis of fiber composite plates and shells are based on several basic simplifying assumptions taken from isotropic plate and shell theory. Since the behavior of isotropic and heterogeneous anisotropic materials differ to a great extent, it is but logical to question the validity of the isotropic plate and shell assumptions where applied to laminated systems.

The goal of the present research is to assess the validity of the basic assumptions presently used in the analysis of laminated plates and shells and to propose an improved set of hypothesis. The structure is discretized by three-dimensional elements. An element stiffness matrix with linear anisotropic material properties is generated using the theorems of potential energy and trivariant linear Hermite displacement functions developed. Since the thickness of laminated structures is usually small compared to the other two dimensions, to avoid ill conditioning of the stiffness matrix the aspect ratio has to be kept small. That is, the mesh points of the finite element grid must be close together and hence linear interpolation for displacements would serve the purpose. This results in 24 degrees of freedom per element.

Basic stiffness matrix is generated and numerical verification is completed using various simple test cases. To verify the extent to which strain variations through the thickness of laminated structures deviate from the usual linear assumption, a beam shown in Figure 28 with four layers through the thickness is analyzed.

Figure 29 shows that along x-direction the displacement is linear, but

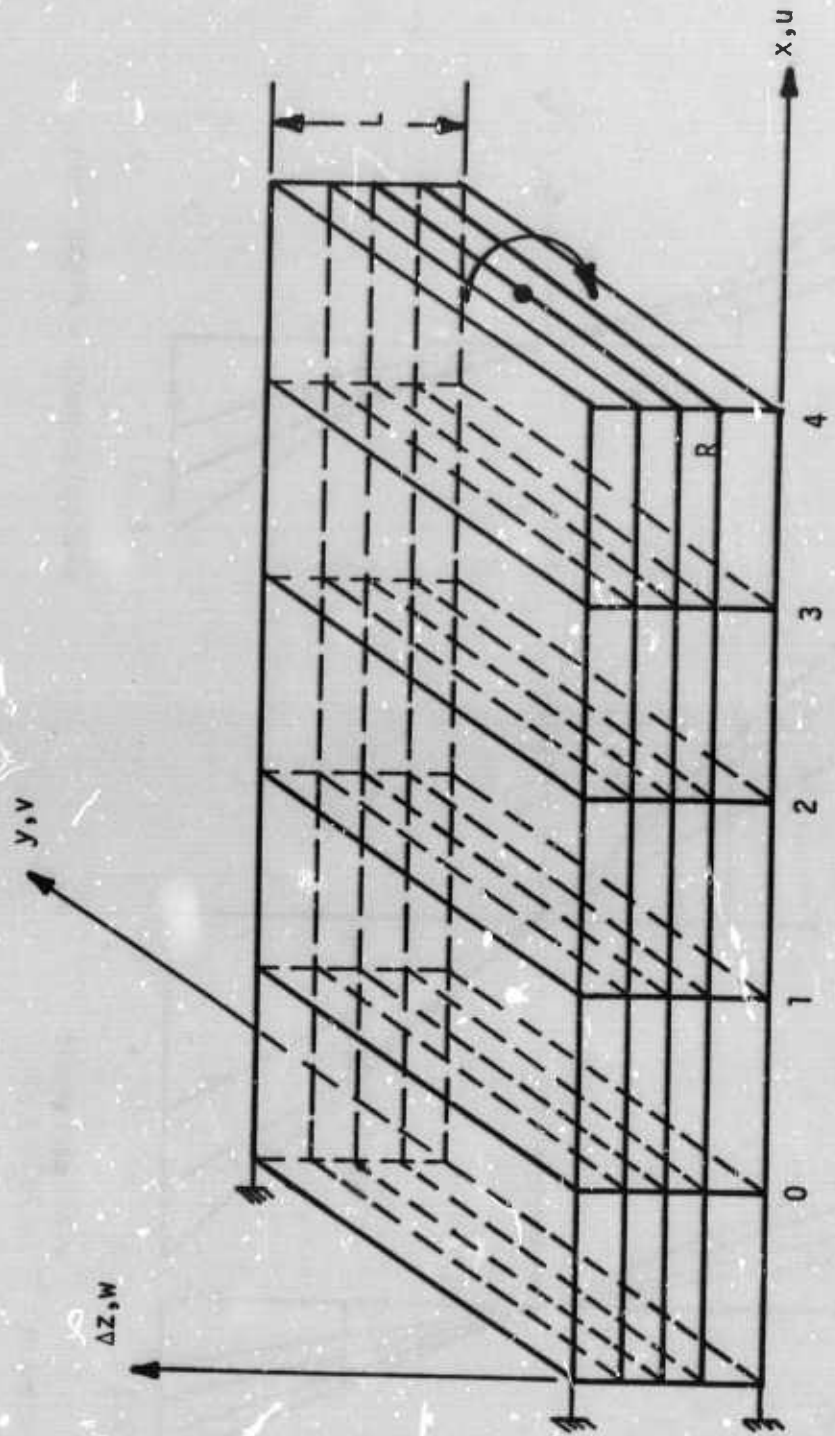


Figure 28. Beam Test Case for the Finite Element Analysis

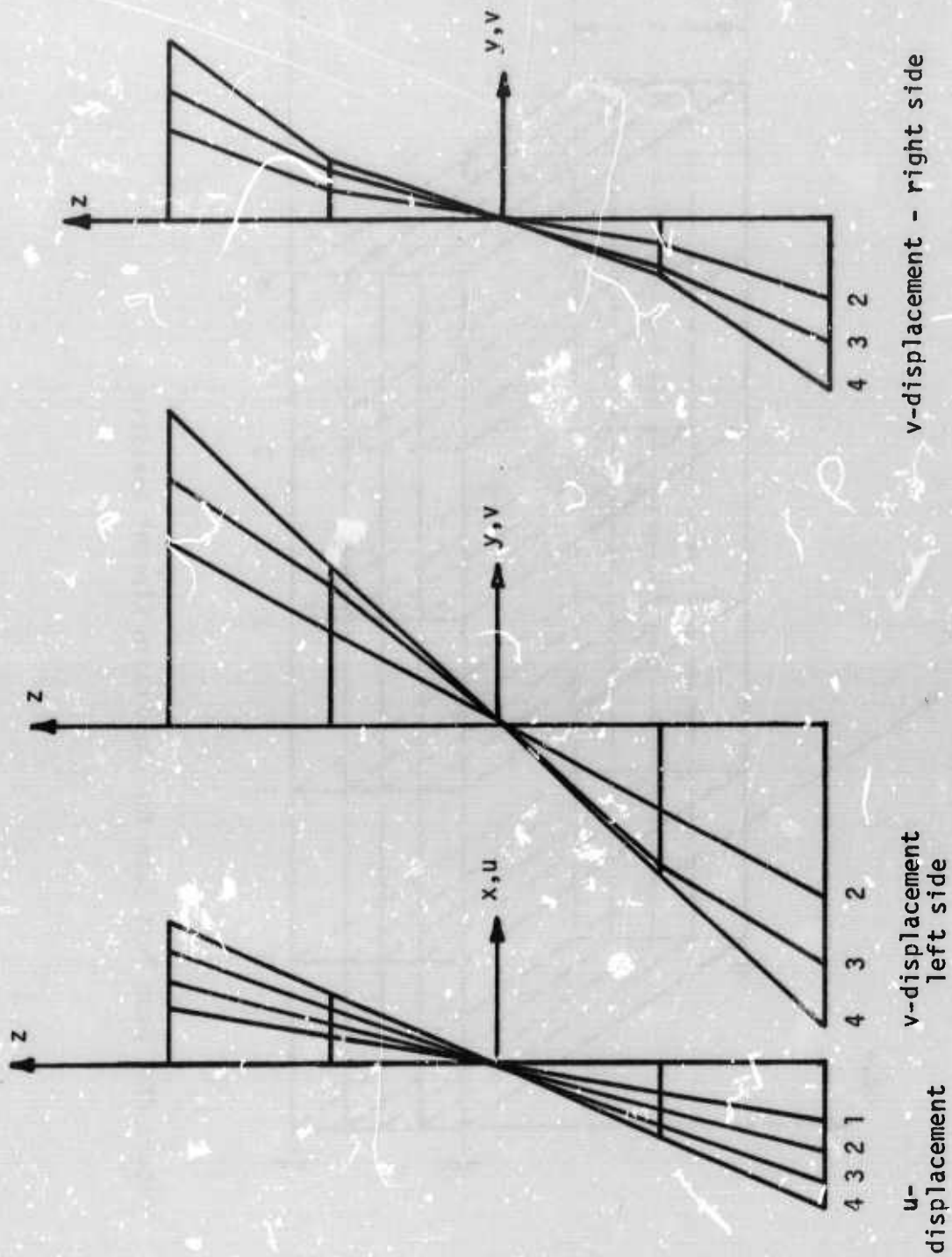


Figure 29. In Plane Displacement Through Thickness

the displacements along y-direction are nonlinear. The displacement in y-direction suggest that there is an inplane unbalanced shear force, and this staggers the laminas. This is due to the fact that the stiffness along the y-direction is much less and antielastic curvature cannot be represented adequately by the model, as we have only one element along the y-direction. The analysis of a plate is underway.

G. Three-Dimensional Finite Element Analysis - Mixed Stress-Displacement Approach
(Professor Schmit and Mr. P. Obaid)

This report contains the analytical investigation carried out in order to examine the validity of basic assumptions upon which the current analysis methods for laminated fiber composite plates and shells rest. Laminated fiber composite plate and shell configurations may be viewed as a collection of highly orthotropic lamina and, in general, assuming the configuration is not unidirectional, the structure is highly heterogeneous through the thickness. The stress-strain characteristics of the orthotropic lamina tend to be linear in the fiber direction, somewhat nonlinear transverse to the fibers, and highly nonlinear under inplane shear. A useful advance in behavior predictions might be achieved by introducing shear nonlinearity while retaining the assumption of linear stress-strain behavior in the longitudinal and transverse directions.

After assessing the validity of basic assumptions of laminated plate and shell analyses, the task will be set forth to find an improved hypothesis and to generate the general capabilities so as to analyze such plate and shell configurations.

Analysis is based on the mixed stress-displacement approach. This formulation corresponds to the Reissner energy principal (Ref. 22). Reissner's variational principal states that of all possible states of stress, that which makes the Reissner energy stationary satisfies the equilibrium equations and force displacement relations as well as the natural boundary conditions (both displacement and force) and is therefore the actual state of stress and displacement.

Formulation of a three-dimensional rectangular parallelepiped element is pursued to begin with. The Reissner energy Π_R of a typical interior discrete element is given as

$$\begin{aligned} \Pi_R = & \int_0^a \int_0^b \int_0^h \left[\sigma_x \frac{\partial u}{\partial x} + \sigma_y \frac{\partial v}{\partial y} + \sigma_z \frac{\partial w}{\partial z} + \tau_{xy} \left(\frac{\partial u}{\partial y} + \frac{\partial v}{\partial x} \right) \right. \\ & \left. + \tau_{yz} \left(\frac{\partial v}{\partial z} + \frac{\partial w}{\partial y} \right) + \tau_{zx} \left(\frac{\partial u}{\partial z} + \frac{\partial w}{\partial x} \right) \right] dx dy dz - \int_0^a \int_0^b \int_0^h u_c dx dy dz \end{aligned} \quad (1)$$

where assumed nodal displacements and stresses consist of triple products of zeroth order Hermite interpolation polynomials.

$$u(x,y,z) = \sum_{i=1}^2 \sum_{j=1}^2 \sum_{k=1}^2 H_{oi}^{(0)}(x) H_{oj}^{(0)}(y) H_{ok}^{(0)}(z) u_{ijk} \quad (2)$$

$$\sigma_x(x,y,z) = \sum_{i=1}^2 \sum_{j=1}^2 \sum_{k=1}^2 H_{oi}^{(0)}(x) H_{oj}^{(0)}(y) H_{ok}^{(0)}(z) \sigma_{xijk} \quad (3)$$

In the above equations u and σ_x represent the displacement and stress respectively in the x direction. Zeroth order Hermitian polynomials are defined as

$$H_{01}(x) = 1 - \frac{x}{a} \quad (4)$$

$$H_{02}(x) = \frac{x}{a} \text{ etc.} \quad (5)$$

a being the distance between two interpolation stations. u_{ijk} and σ_{xijk} represent the nodal displacement and nodal stress along x -axis.

For a general homogeneous anisotropic elastic body, stress-strain relations including thermal contributions can be written as

$$\begin{Bmatrix} \epsilon_x \\ \epsilon_y \\ \epsilon_z \\ \gamma_{xy} \\ \gamma_{yz} \\ \gamma_{zx} \end{Bmatrix} = \begin{bmatrix} b_{11} & b_{12} & \cdot & \cdot & \cdot & \cdot & b_{16} \\ b_{21} & b_{22} & \cdot & \cdot & \cdot & \cdot & b_{26} \\ \cdot & \cdot & \cdot & \cdot & \cdot & \cdot & \cdot \\ \cdot & \cdot & \cdot & \cdot & \cdot & \cdot & \cdot \\ \cdot & \cdot & \cdot & \cdot & \cdot & \cdot & \cdot \\ b_{61} & b_{62} & \cdot & \cdot & \cdot & \cdot & \cdot \end{bmatrix} \begin{Bmatrix} \sigma_x \\ \sigma_y \\ \sigma_z \\ \tau_{xy} \\ \tau_{yz} \\ \tau_{zx} \end{Bmatrix} + \begin{Bmatrix} \alpha_x \\ \alpha_y \\ \alpha_z \\ \alpha_{xy} \\ \alpha_{yz} \\ \alpha_{zx} \end{Bmatrix} \Delta T(x,y,z) \quad (6)$$

$$\text{or } \vec{\epsilon} = [b] \vec{\sigma} + \vec{\alpha} \Delta T \quad (7)$$

where $\vec{\epsilon}$ and $\vec{\sigma}$ represent the strain and stress vectors respectively. $\vec{\alpha}$

contains the thermal contribution and [b] contains the generalized 36 elastic coefficients out of which only 21 are independent due to the symmetry of matrix [b].

The elastic coefficients or so-called stiffness coefficients are reduced from 21 to 9 independent constants for an orthotropic body and to only 2 independent constants for the case of an isotropic body. These elastic constants are given in reference (23). However, it must be recognized that shearing strains and shearing stresses are expressed in different order in equation (6) than in reference (23) due to which position of various rows and columns in matrix [b] and in vector $\vec{\alpha}$ are also changed. Hence, to avoid any confusion the expressions for various elastic coefficients are given as

$$\begin{aligned}
 b_{11} &= \frac{1}{E_{xx}} , & b_{22} &= \frac{1}{E_{yy}} , & b_{33} &= \frac{1}{E_{zz}} \\
 b_{12} &= -\frac{\nu_{yx}}{E_{xx}} = -\frac{\nu_{xy}}{E_{yy}} , & b_{23} &= -\frac{\nu_{zy}}{E_{yy}} = -\frac{\nu_{yz}}{E_{zz}} , & b_{13} &= -\frac{\nu_{xz}}{E_{zz}} = -\frac{\nu_{zx}}{E_{xx}} \\
 b_{44} &= \frac{1}{G_{xy}} , & b_{55} &= \frac{1}{G_{yz}} , & b_{66} &= \frac{1}{G_{zx}} \\
 b_{14} &= \frac{\eta_{xy,x}}{E_{xx}} = \frac{\eta_{x,xy}}{G_{xy}} , & b_{24} &= \frac{\eta_{xy,y}}{E_{yy}} = \frac{\eta_{y,xy}}{G_{xy}} \\
 b_{34} &= \frac{\eta_{xy,z}}{E_{xx}} = \frac{\eta_{z,xy}}{G_{xy}} , & b_{15} &= \frac{\eta_{yz,x}}{E_{xx}} = \frac{\eta_{x,yz}}{G_{xy}} \\
 b_{25} &= \frac{\eta_{yz,y}}{E_{yy}} = \frac{\eta_{y,yz}}{G_{yz}} , & b_{35} &= \frac{\eta_{yz,z}}{E_{zz}} = \frac{\eta_{z,yz}}{G_{yz}} \\
 b_{16} &= \frac{\eta_{zx,x}}{E_{xx}} = \frac{\eta_{x,zx}}{G_{zx}} , & b_{26} &= \frac{\eta_{zx,y}}{E_{yy}} = \frac{\eta_{y,zx}}{G_{zx}} \\
 & & b_{36} &= \frac{\eta_{zx,z}}{E_{zz}} = \frac{\eta_{z,zx}}{G_{zx}} \\
 b_{45} &= \frac{\mu_{yz,xy}}{G_{xy}} = \frac{\mu_{xy,yz}}{G_{yz}} , & b_{46} &= \frac{\mu_{zx,xy}}{G_{xy}} = \frac{\mu_{xy,zx}}{G_{zx}} \\
 & & b_{56} &= \frac{\mu_{zx,yz}}{G_{yz}} = \frac{\mu_{yz,zx}}{G_{zx}}
 \end{aligned} \tag{8}$$

where E_{xx} , E_{yy} and E_{zz} are Young's moduli corresponding to X, Y and Z axes respectively. G_{xy} , G_{yz} and G_{zx} are shear moduli corresponding to planes xy, yz and zx respectively. ν_{yx} , ν_{xy} , ..., ν_{zx} are the Poisson's coefficients which characterize transverse compression or tension in the direction of coordinate axes. Coefficients of mutual influence $\eta_{xy,x}$, $\eta_{x,xy}$, ..., $\eta_{z,zx}$ are shears in the planes parallel to the coordinates under the influence of normal stresses. Chentsov's coefficients $\mu_{yz,xy}$, $\mu_{xy,yz}$, ..., $\mu_{yz,zx}$ characterize the shear in the plane which are parallel to the coordinates and which include the tangential stresses parallel to other coordinate planes.

Complementary strain energy density u_c is given as

$$u_c = \int_0^{\sigma_x} \epsilon_x d\sigma_x + \int_0^{\sigma_y} \epsilon_y d\sigma_y + \dots + \int_0^{\tau_{zx}} \gamma_{zx} d\tau_{zx} \quad (9)$$

Substituting equation (6) into equation (9) we get

$$\begin{aligned} u_c = & \frac{1}{2} \{ (b_{11} \sigma_x^2 + b_{22} \sigma_y^2 + b_{33} \sigma_z^2 + b_{44} \tau_{xy}^2 + b_{55} \tau_{yz}^2 + b_{66} \tau_{zx}^2) \\ & + 2(b_{12} \sigma_x \sigma_y + b_{13} \sigma_x \sigma_z + b_{14} \sigma_x \tau_{xy} + b_{15} \sigma_x \tau_{yz} + b_{16} \sigma_x \tau_{zx} \\ & + b_{23} \sigma_y \sigma_z + b_{24} \sigma_y \tau_{xy} + b_{25} \sigma_y \tau_{yz} + b_{26} \sigma_y \tau_{zx} + b_{34} \sigma_z \tau_{xy} \\ & + b_{35} \sigma_z \tau_{yz} + b_{36} \sigma_z \tau_{zx} + b_{45} \tau_{xy} \tau_{yz} + b_{46} \tau_{xy} \tau_{zx} + b_{56} \tau_{yz} \tau_{zx}) \} \\ & + \Delta T (\alpha_x \sigma_x + \alpha_y \sigma_y + \alpha_z \sigma_z + \alpha_{xy} \tau_{xy} + \alpha_{yz} \tau_{yz} + \alpha_{zx} \tau_{zx}) \quad (10) \end{aligned}$$

By substituting equations (2), (3) and (10) into equation (1), the following expression is obtained after integration over the volume of a discrete element.

$$\Pi_R = \vec{\chi}^T \begin{bmatrix} [C] \\ 1 \times 24 & 24 \times 48 & 48 \times 1 \end{bmatrix} \vec{\sigma} - \frac{1}{2} \vec{\sigma}^T \begin{bmatrix} [D] \\ 1 \times 48 & 48 \times 48 & 48 \times 1 \end{bmatrix} \vec{\sigma} + \vec{\sigma}^T \begin{bmatrix} \vec{Q} \\ 1 \times 48 & 48 \times 1 \end{bmatrix} \dots \quad (11)$$

where

$$\vec{\chi}^T = L \begin{bmatrix} U_{111}, U_{112}, U_{121}, U_{122}, U_{211}, U_{212}, U_{221}, U_{222}, \nu_{111}, \nu_{112}, \dots \\ \dots, \nu_{222}, w_{111}, w_{112}, \dots, w_{222} \end{bmatrix} \quad (12)$$

$$\vec{\sigma}^T = [\sigma_{x_{111}}, \sigma_{x_{112}}, \sigma_{x_{i21}}, \sigma_{x_{122}}, \sigma_{x_{211}}, \sigma_{x_{212}}, \sigma_{x_{221}}, \sigma_{x_{222}}, \sigma_{y_{111}}, \sigma_{y_{112}}, \dots, \sigma_{y_{222}}, \sigma_{z_{111}}, \sigma_{z_{112}}, \dots, \sigma_{z_{222}}, \tau_{xy_{111}}, \tau_{xy_{112}}, \dots, \tau_{xy_{222}}, \tau_{yz_{111}}, \tau_{yz_{112}}, \dots, \tau_{yz_{222}}, \tau_{zx_{111}}, \tau_{zx_{112}}, \dots, \tau_{zx_{222}}] \quad (13)$$

and define column vectors $\vec{P}(x)$, $\vec{P}'(x)$, $\vec{Q}(y)$, $\vec{Q}'(y)$, $\vec{R}(z)$ and $\vec{R}'(z)$ as

$$\begin{aligned} \vec{P}^T(x) &= [H_{01}^{(0)}(x), H_{01}^{(0)}(x), H_{01}^{(0)}(x), H_{01}^{(0)}(x), H_{02}^{(0)}(x), H_{02}^{(0)}(x), H_{02}^{(0)}(x), H_{02}^{(0)}(x)] \\ \vec{Q}^T(y) &= [H_{01}^{(0)}(y), H_{01}^{(0)}(y), H_{02}^{(0)}(y), H_{02}^{(0)}(y), H_{01}^{(0)}(y), H_{01}^{(0)}(y), H_{02}^{(0)}(y), H_{02}^{(0)}(y)] \\ \vec{R}^T(z) &= [H_{01}^{(0)}(z), H_{02}^{(0)}(z), H_{01}^{(0)}(z), H_{02}^{(0)}(z), H_{01}^{(0)}(z), H_{02}^{(0)}(z), H_{01}^{(0)}(z), H_{02}^{(0)}(z)] \\ &\dots (14) \end{aligned}$$

$\vec{P}'(x)$, $\vec{Q}'(y)$ and $\vec{R}'(z)$ are the first derivatives of $\vec{P}(x)$, $\vec{Q}(y)$ and $\vec{R}(z)$ respectively. Now displacements and stresses can be expressed in the form

$$\begin{aligned} u(x,y,z) &= \sum_{i=1}^8 X_i P_i(x) Q_i(y) R_i(z) \\ v(x,y,z) &= \sum_{i=9}^{16} X_i P_{i-8}(x) Q_{i-8}(y) R_{i-8}(z) \\ w(x,y,z) &= \sum_{i=17}^{24} X_i P_{i-16}(x) Q_{i-16}(y) R_{i-16}(z) \\ \sigma_x(x,y,z) &= \sum_{i=1}^8 \sigma_i P_i(x) Q_i(y) R_i(z) \\ \sigma_y(x,y,z) &= \sum_{i=9}^{16} \sigma_i P_{i-8}(x) Q_{i-8}(y) R_{i-8}(z) \quad \dots (15) \\ \sigma_z(x,y,z) &= \sum_{i=17}^{24} \sigma_i P_{i-16}(x) Q_{i-16}(y) R_{i-16}(z) \end{aligned}$$

$$\tau_{xy}(x,y,z) = \sum_{i=25}^{32} \sigma_i P_{i-24}(x) Q_{i-24}(y) R_{i-24}(z)$$

$$\tau_{yz}(x,y,z) = \sum_{i=33}^{40} \sigma_i P_{i-32}(x) Q_{i-32}(y) R_{i-32}(z)$$

$$\tau_{zx}(x,y,z) = \sum_{i=41}^{48} \sigma_i P_{i-40}(x) Q_{i-40}(y) R_{i-40}(z)$$

where subscripts $i, i-8$ etc. represent the particular elements of vectors \vec{P} , \vec{Q} and \vec{R} . Matrix $[C]$ is partitioned as follows

$$[C] = \left[\begin{array}{ccc|ccc} c^{(11)} & 0 & 0 & c^{(14)} & 0 & c^{(16)} \\ 0 & c^{(22)} & 0 & c^{(24)} & c^{(25)} & 0 \\ 0 & 0 & c^{(33)} & 0 & c^{(35)} & c^{(36)} \end{array} \right] \dots (16)$$

where all of the submatrices are 8x8 dimensional arrays. Elements of each submatrix are given as

$$c_{ij}^{(11)} = \int_0^a P_i P_j' dx \int_0^b Q_i Q_j dy \int_0^h R_i R_j dz$$

$$c_{ij}^{(22)} = \int_0^a P_i P_j dx \int_0^b Q_i Q_j' dy \int_0^h R_i R_j dz$$

$$c_{ij}^{(33)} = \int_0^a P_i P_j dx \int_0^b Q_i Q_j dy \int_0^h R_i R_j' dz \quad (17)$$

$$c_{ij}^{(24)} = c_{ij}^{(36)} = c_{ij}^{(11)}$$

$$c_{ij}^{(14)} = c_{ij}^{(35)} = c_{ij}^{(22)}$$

$$c_{ij}^{(25)} = c_{ij}^{(16)} = c_{ij}^{(33)}$$

The range of subscripts i and j is from 1 to 8. Now $[D]$ can be partitioned as

$$[D] = \begin{bmatrix} D^{(11)} & D^{(12)} & \cdot & \cdot & \cdot & D^{(16)} \\ D^{(21)} & D^{(22)} & \cdot & \cdot & \cdot & D^{(26)} \\ \cdot & \cdot & \cdot & \cdot & \cdot & \cdot \\ \cdot & \cdot & \cdot & \cdot & \cdot & \cdot \\ D^{(61)} & \cdot & \cdot & \cdot & \cdot & D^{(66)} \end{bmatrix}$$

[D] is a symmetric matrix and all the submatrices such as $D^{(11)}$, $D^{(12)}$... etc. are 8×8 dimensional arrays. The elements of these matrices can be defined as

$$D_{ij}^{(k1)} = b_{k1} \int_0^a P_i P_j dx \int_0^b Q_i Q_j dy \int_0^h R_i R_j dz \quad \dots (19)$$

where subscripts i and j both vary from 1 to 8. In equation (19) b_{k1} represents the stiffness coefficients which have already been defined in equation (8).

The column vector \bar{Q} is the thermal contribution and is given in the form

$$\bar{Q} = \begin{Bmatrix} \bar{Q}^{(1)} \\ \bar{Q}^{(2)} \\ \cdot \\ \cdot \\ \cdot \\ \bar{Q}^{(6)} \end{Bmatrix} \quad (20)$$

in which $\bar{Q}^{(1)}$, $\bar{Q}^{(2)}$,, $\bar{Q}^{(6)}$ are all 8×1 dimensional arrays and are defined as

$$Q_i^{(1)} = \int_0^a \int_0^b \int_0^h (\alpha_x \Delta T P_i Q_i R_i) dx dy dz$$

$$Q_i^{(2)} = \int_0^a \int_0^b \int_0^h (\alpha_y \Delta T P_i Q_i R_i) dx dy dz$$

$$Q_i^{(3)} = \int_0^a \int_0^b \int_0^h (\alpha_z \Delta T P_i Q_i R_i) dx dy dz \quad (21)$$

$$Q_i^{(4)} = \int_0^a \int_0^b \int_0^h (\alpha_{xy} \Delta T P_i Q_i R_i) dx dy dz$$

$$Q_i^{(5)} = \int_0^a \int_0^b \int_0^h (\alpha_{yz} \Delta T P_i Q_i R_i) dx dy dz$$

$$Q_i^{(6)} = \int_0^a \int_0^b \int_0^h (\alpha_{zx} \Delta T P_i Q_i R_i) dx dy dz$$

Range of subscripts is from 1 to 8.

A simple three-dimensional elasticity problem was solved using the Reissner variational principal. The test problem consisted of a prismatic bar stretched by an axial force P applied at one end. Dimensions of the bar and other necessary details are given in Figure 30. One end of the bar was fixed. Reissner energy for this problem is given as

$$\Pi_R = \bar{X} [C] \bar{\sigma} - \frac{1}{2} \bar{\sigma}^T [D] \bar{\sigma} + \bar{\sigma}^T \bar{Q} - \bar{X}^T \bar{P} \quad (22)$$

where \bar{P} is a vector containing 24 generalized loads associated with each of the 24 nodal degrees of freedom contained in \bar{X} . Other notations have been defined earlier.

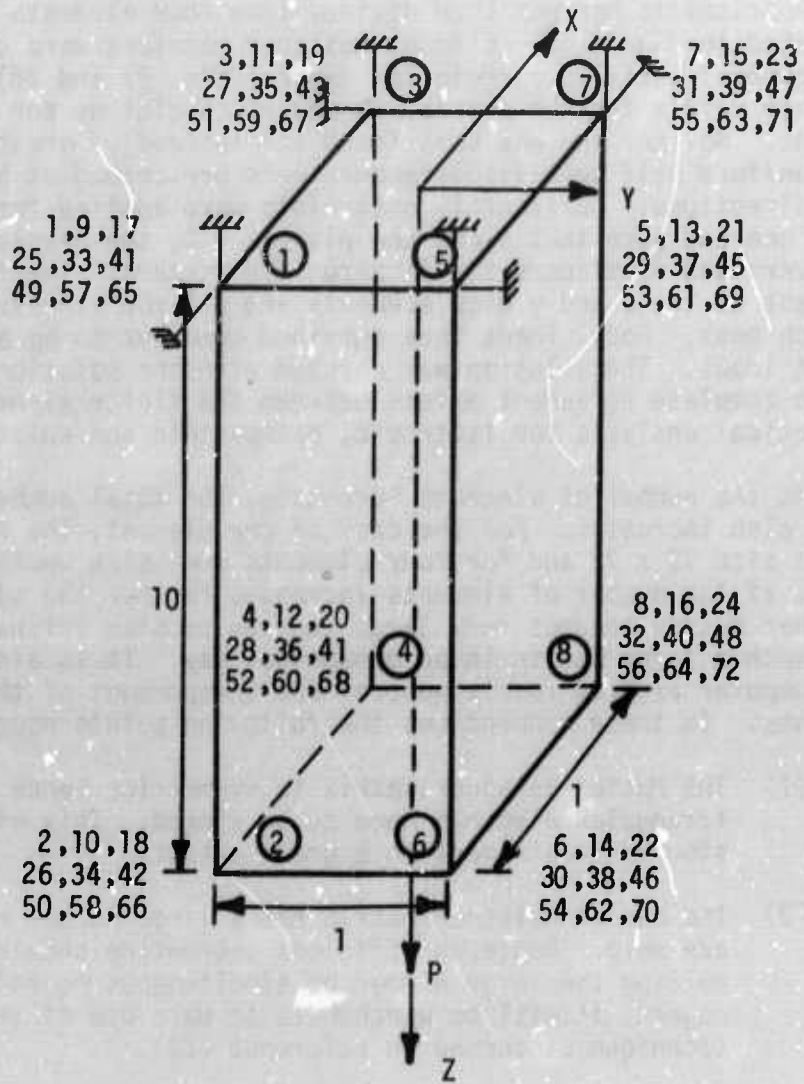
Take the variation of Reissner energy Π_R (Refs. 24 and 25) and define:

$$\begin{matrix} (11) & (12) & (21) & (22) \\ [R] = - [D] & , & [R] = [C] & , & [R] = [C]^T & \text{and} & [R] = [0] \end{matrix} \quad \dots \quad (23)$$

Hence

$$\begin{bmatrix} R^{(11)} & R^{(12)} \\ 48 \times 48 & 48 \times 24 \end{bmatrix} \begin{Bmatrix} \bar{\sigma} \\ 48 \times 1 \end{Bmatrix} = \begin{Bmatrix} -\bar{Q} \\ 48 \times 1 \end{Bmatrix} \\ \hline \begin{bmatrix} R^{(21)} & R^{(22)} \\ 24 \times 48 & 24 \times 24 \end{bmatrix} \begin{Bmatrix} \bar{X} \\ 24 \times 1 \end{Bmatrix} = \begin{Bmatrix} \bar{P} \\ 24 \times 1 \end{Bmatrix} \quad (24)$$

$R^{(11)}$, $R^{(12)}$, $R^{(21)}$, and $R^{(22)}$ are called as Reissner submatrices. Equation



$$\begin{matrix}
 x & x & x \\
 x & x & x \\
 x & x & x
 \end{matrix}
 \left. \vphantom{\begin{matrix} x \\ x \\ x \end{matrix}} \right\} = \begin{cases}
 \sigma_x & \sigma_y & \sigma_z \\
 \tau_{xy} & \tau_{yz} & \tau_{zx} \\
 u & v & w
 \end{cases}$$

Figure 30. Fixed End Prismatic Bar Stretched Under an Axial Load.

(24) was successfully solved using computer technique and results showed excellent agreement with the theoretical analysis (Ref.23) for isotropic, orthotropic and anisotropic cases.

A prismatic bar was then divided into four elements in the xy plane as indicated in Figure 31. Element Reissner matrices were combined with the help of a general variable correlation table (Refs. 27 and 28) to give the master Reissner matrix for the system. Boundary conditions for this case were slightly altered. Neither end was kept fixed and instead of prescribing the load at one end, uniform half unit displacements were prescribed at both ends in the opposite directions. Horizontal constraints were applied for displacements u and v at one end such that along the plane $z = 0$, the displacement u is zero if x is zero and displacement v is zero if y is zero. The final analysis gives the rest of the u and v displacements and all the stresses and applied loads at each node. Nodal loads thus obtained come out to be equal to the work equivalent loads. The solution was checked with the solution given in reference 23 and complete agreement exists between the finite element analysis and the theoretical analysis for isotropic, orthotropic and anisotropic cases.

As the number of elements increases, the total number of unknown variables also increases. For the case of one element, the Reissner matrix was of the size 72×72 and for four elements its size increases to 162×162 . Hence, if the number of elements increases further, the size of the master Reissner matrix becomes very large and the problem arises as to how to deal with such a large matrix in an economical way. It is also desirable to make the computer program fairly general and independent of the total number of elements. In these connections the following points need to be considered:

- (1) The Master Reissner matrix is symmetric; hence, only the upper triangular elements need to be stored. This will cut down the storage requirement to a great extent.
- (2) The Master Reissner matrix has a large number of elements which are zero. Hence, an efficient subroutine should be used for solving the large number of simultaneous equations. In this regard, it will be worthwhile to make use of the wave front technique discussed in reference (28).
- (3) Maximum possible use will be made of extra storage capacity of the computer in order to handle very large matrices.

Further effort is now directed toward writing a general program based on the above considerations, which will facilitate assessment of the basis assumptions on which current laminated plate and shell theory rests.

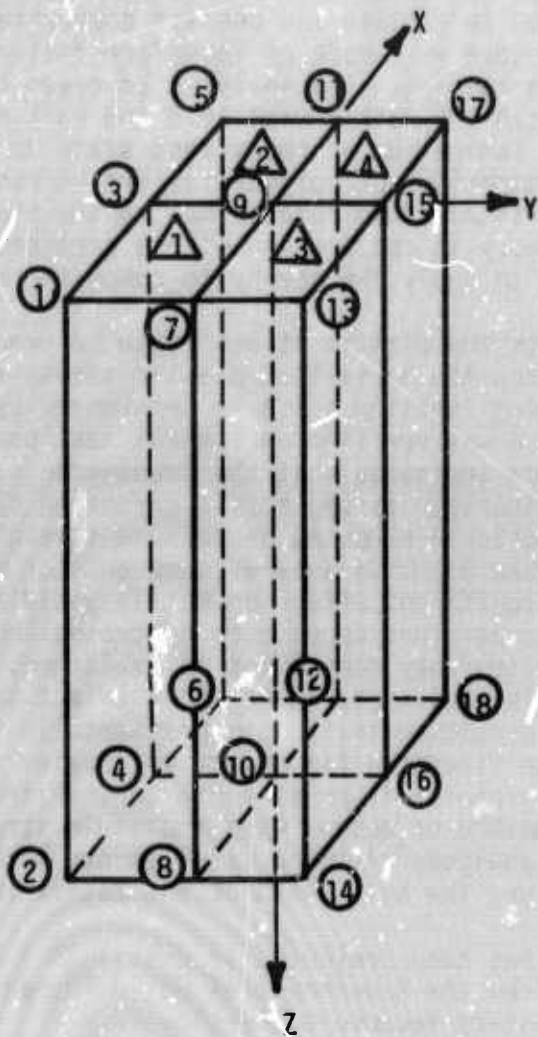


Figure 31. Prismatic Bar Divided into Four Finite Elements.

SECTION VI

FAILURE OF COMPOSITE STRUCTURAL ELEMENTS

A. Interfiber Failure of Composite Materials

(Professor T. P. Kicher and Dr. J. B. Koeneman)

The conditions which exist at failure of unidirectional, continuous fiber, off-axis epoxy matrix composite materials were investigated. A micromechanic failure criterion was established which reflected these conditions, and the results were used to explain and predict composite behavior. Observations through a microscope were made of interface failure of single fiber inclusion specimens during loading. The analysis of creep tests was used to determine the point at which the matrix went into the bulk plastic region, and this was used to give an indication of the stress state in the matrix. Based on these results and a comparison of polymer failure characteristics, the failure criterion chosen was a critical creep rate normal to the plane of fracture. The Eyring rate process theory in conjunction with a combined stress, nonlinear creep theory was used to apply the theory to composite materials.

To calculate the plastic stress state, a procedure proposed by Neuber was used which relates the equivalent plastic stress to the elastic solution by means of a leading function which is determined by the nonlinear stress-strain law. This method was verified on several test problems. Applications of the failure criterion indicates that the transverse strength of unidirectional composites should increase as the strain hardening of this type matrix increases. The effect of residual stresses on failure strength is predicted to be minimal. The shear stresses existing around fiber ends or where a fiber passes through a void have a significant effect on matrix yield and composite failure. The difference in temperature dependence of crossplied strength between glass-fiber and graphite-fiber composites is explained. The width effect of crossplied strength is explained, and a width effect and layer effect on crossplied creep rate was predicted and then experimentally verified. An explanation is provided for the strengthening effect on epoxies of elastomer inclusions. The sensitivity of graphite-fiber strength to the stress state in the matrix is predicted. A method of determining the yield stress of high strain hardening epoxies by the analysis of creep data was developed. This technique was also adapted to measure the bulk yield of the matrix in a unidirectional composite.

This work has been presented in detail in a Topical Report (29). Copies are available from the Department of Solid Mechanics, Structures and Mechanical Design, Case Western Reserve University.

B. Fracture Toughness of Fiber Composites

(Professor T. P. Kicher and Mr. T. C. Esselman)

In the past year, many tests have been conducted to determine the nature of the stress intensity factor and the plane strain fracture toughness of fiber composites. An effort has been made to adapt the ASTM Standard (30) for fracture toughness testing of metals to an orthotropic or anisotropic body. The specimens are tested in three point bending (Figure 32). A chevron notch is machined into the specimens and a crack is fatigued in this notch. A

solution of black India ink and ethylene glycol is injected into the crack as it is being fatigued so that its progress may be followed visually and so that, after fracture, the initial crack length can be easily measured by the extension of the ink solution (Figure 33). Since the ink is allowed to dry before the test, this assumes that there is no slow crack growth during the prefracture loading. Visual observations during the test justify this assumption.

During the test, a continuous record is kept on an x-y recorder of the applied load and the separation displacement, the displacement apart at the sides of the crack. The separation displacement is measured using a double cantilever beam transducer with strain gages. Knife edges are clamped to both sides of the crack and the transducer is attached to these. The load is measured with a load cell. These transducers can be seen in position in Figure 32.

The tests were conducted on an Instron at a loading rate of .100 inches per minute. The strain rate was varied only for a series of tests where effect of variation with strain rate was of interest. The Instron's compression load cell was also used as a check of the load measured on the x-y recorder.

Both unidirectional and crossplied fiber glass were tested.

1. Unidirectional specimens

The unidirectional specimens were chosen with the crack running parallel to the fibers since it has been shown by a number of authors (31,32) that the value of the stress intensity factor for an orthotropic plate with the crack propagating in one of the material principal directions can be found by using the isotropic analysis. The isotropic analysis used by the ASTM is, for the stress intensity factor,

$$K_I = Y \frac{3 P L a^{1/2}}{B W^2}$$

for the three point bend test. Y is found by boundary collocation (33) and is given by

$$y = 1.93 - 3.07(a/W) + 14.53(a/W)^2 - 25.11(a/W)^3 - 25.80(a/W)^4$$

In order to make the tests completely meaningful, a state of plane strain should exist in the specimen. However, several things indicate that for specimen thicknesses less than one inch (the maximum thickness tested in these experiments) a state of plane strain is not present. The load-displacement curves show this. Figure 34 is an example of a load-displacement curve. This curve was chosen as an example since the change in slope was so pronounced. In most others, the change in slope is more subtle but nevertheless, present.

The nominal stress at the crack tip was found using a simple $\frac{M C}{I}$ relation which gives

$$\sigma_N = \frac{3 P L}{B (W-a)^2}$$

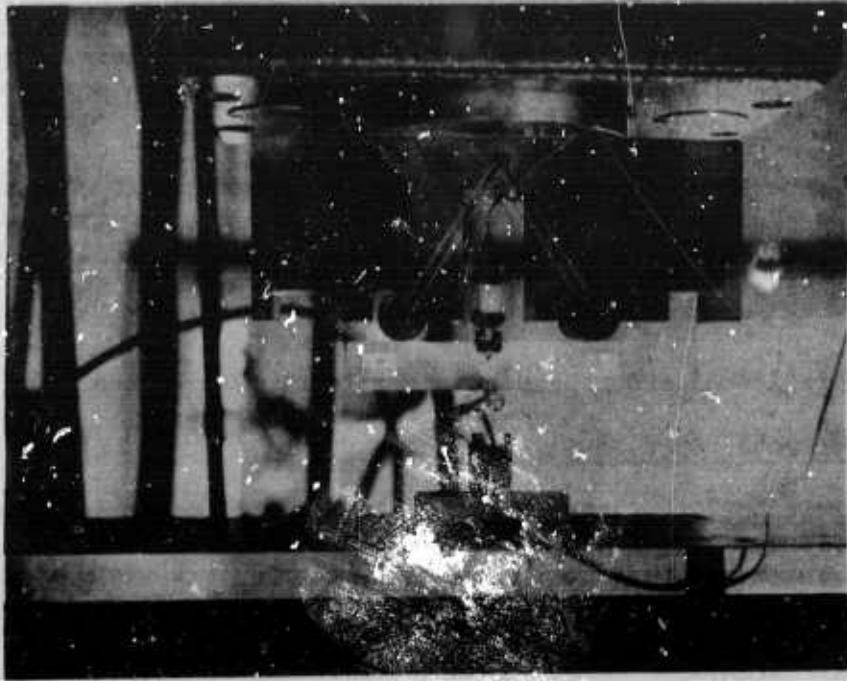


Figure 32. Photo of Fracture Toughness Apparatus.

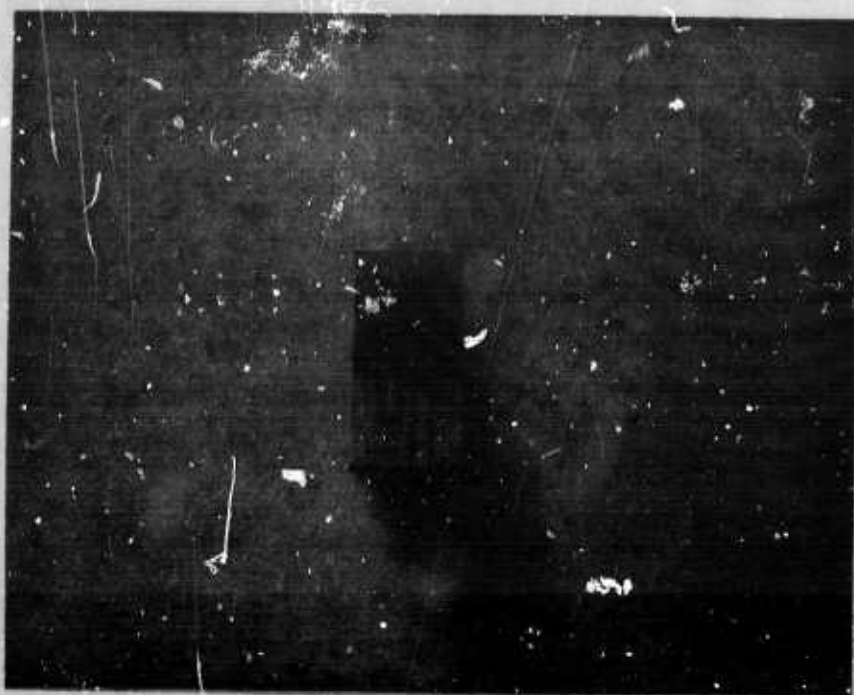


Figure 33. Photo of Fractured Specimen.

For the specimen whose load-displacement curve is given in Figure 34, the nominal stress at fracture was 6154 psi and the nominal stress at the break in slope is approximately 1170 psi. It has been found by Koenemari (29) that the yield stress for unidirectional fiber glass composites with the fibers perpendicular to the tensile loading direction is 1800 psi. Considering that the nominal stress includes no stress concentration factors, the break in the slope corresponds to yielding in the material. The region above the yield point, which is fairly linear over most of its range, can be attributed to either slow crack growth or gross plastic deformation. If it is gross plastic deformation the tip of the crack would be blunted by the plastic zone.

A plot of the field stress vs. the crack depth, shown in Figure 35, also indicates that plane stress does not exist in the specimen. The basis of the linear elastic plane strain fracture toughness is that $\sigma_f(a)^{1/2}$ is constant, where σ_f is the stress in the field without the crack and a is the crack length. Thus, a plot of $\log \sigma_f$ vs. $\log a$ should have a slope of $-.5$. Figure 35 shows a slope of -1.44 which indicates that linear elasticity does not apply. The nominal stress at the crack tip is plotted in Figure 36 as a function of crack depth, and the value of K as a function of crack depth is plotted in Figure 37.

The value of K vs. the thickness of the specimen is shown in Figure 38. Each point on the graph represents a series of six to fifteen specimens which were normalized with respect to the crack depth ratio. Therefore, the value of K at each thickness corresponds to the value of K at a constant crack depth ratio, chosen arbitrarily as 5. The trend that this curve takes is opposite to what is expected from metals. The plane strain fracture toughness is generally accepted as a conservative value, i.e., it is lower than the stress intensity at a state of plane stress. Therefore, the slope in the transition region from plane stress (thin specimens) to plane strain (thick specimens) should be negative. The reason for this discrepancy has not been found yet but is probably in the nature of the plastic zones for composite specimens.

The variation of K with respect to the rate of loading was also studied. The results, plotted on semi-log paper, are shown in Figure 39. The trend is as it was expected to appear.

The variation of K with respect to void content of the material is also being studied but only preliminary results are now available. This data will appear in a later report.

The data presented for the unidirectional specimens should not be taken as values of plane strain fracture toughness. As was pointed out, the specimens were in a transition region between plane stress and plane strain. The ASTM suggests for metals that specimen thickness should be greater than $2.5(K_I / \sigma_{ys})^2$ for a condition of plane strain to exist. Assuming this to be true for composites also would indicate that specimen thickness of approximately 2.5 inches or greater are necessary. The difficulties in fabricating

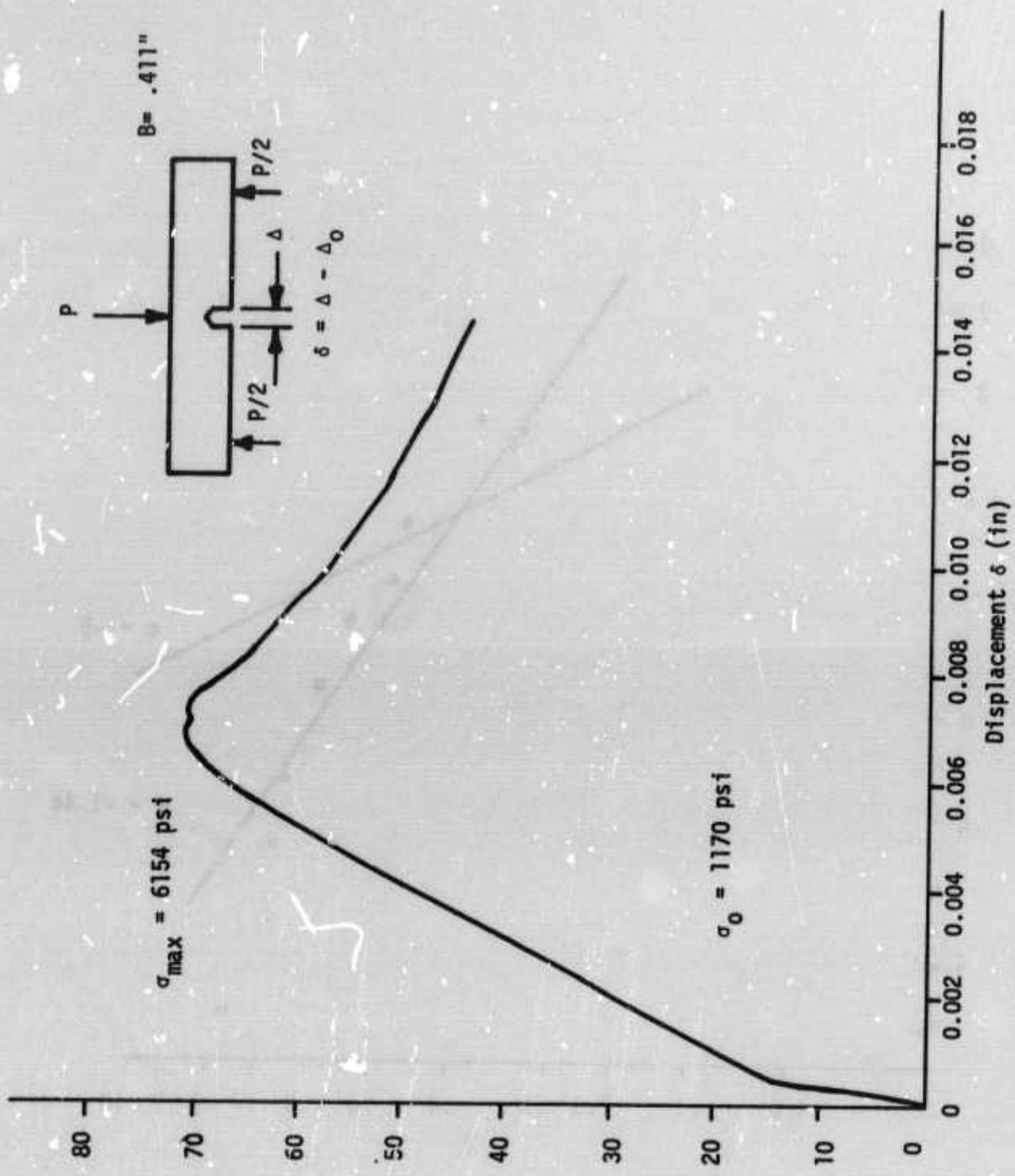


Figure 34. Load-Displacement Record for Specimen 0-1210-E.

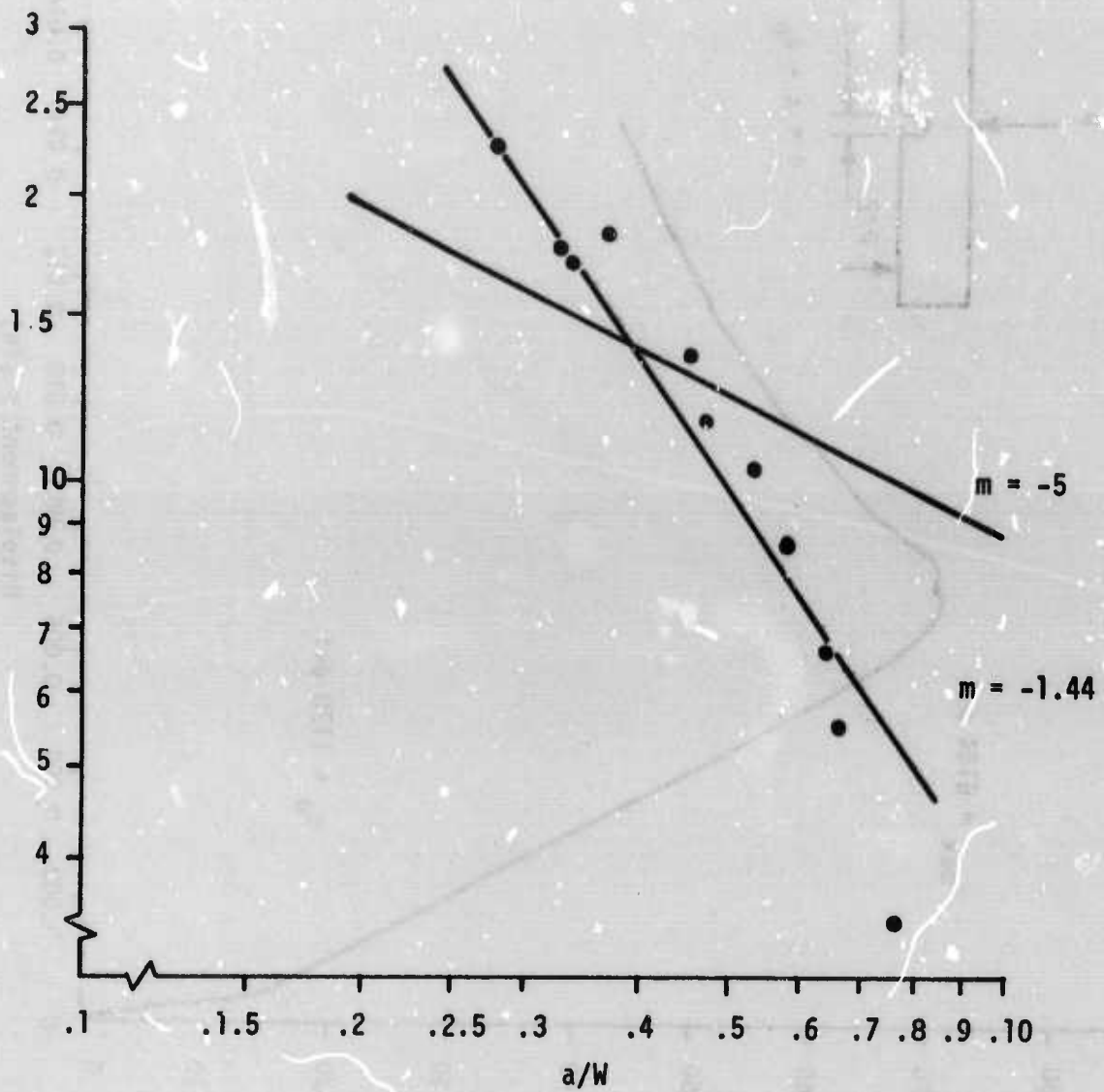


Figure 35. Stress in Field vs. Crack Depth Ratio

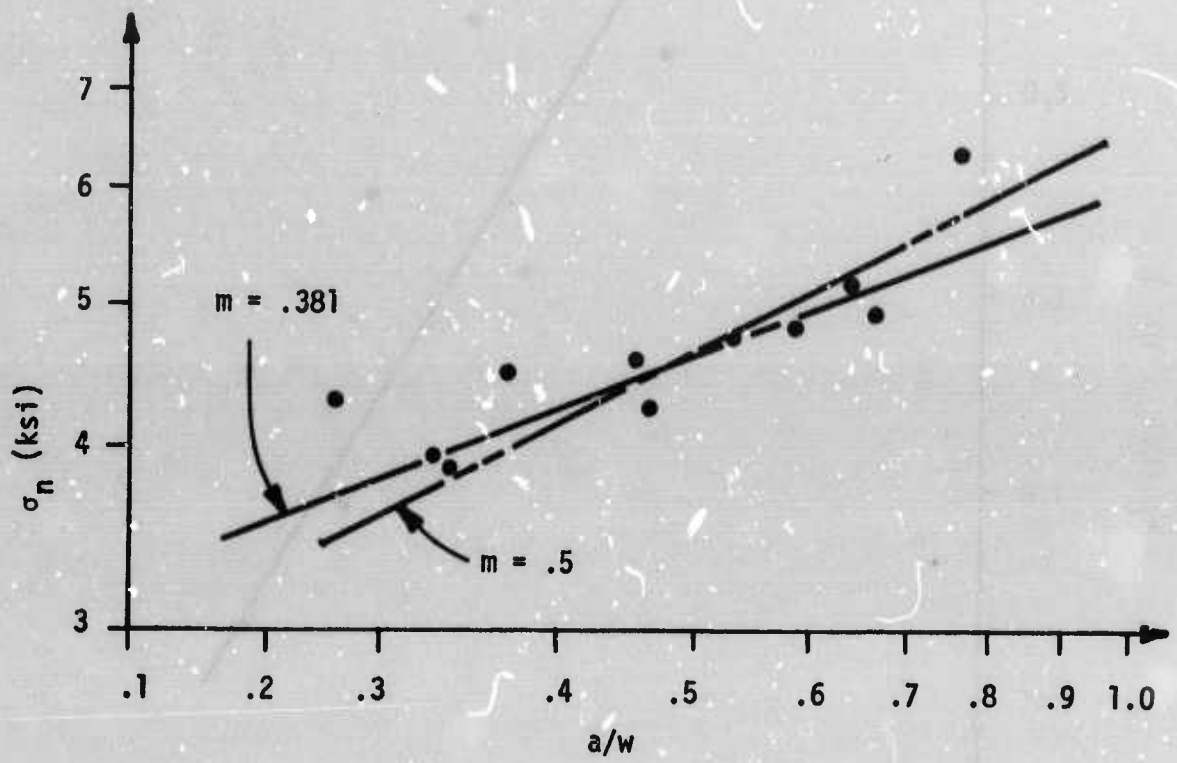


Figure 36. Nominal Stress vs. Crack Depth Ratio

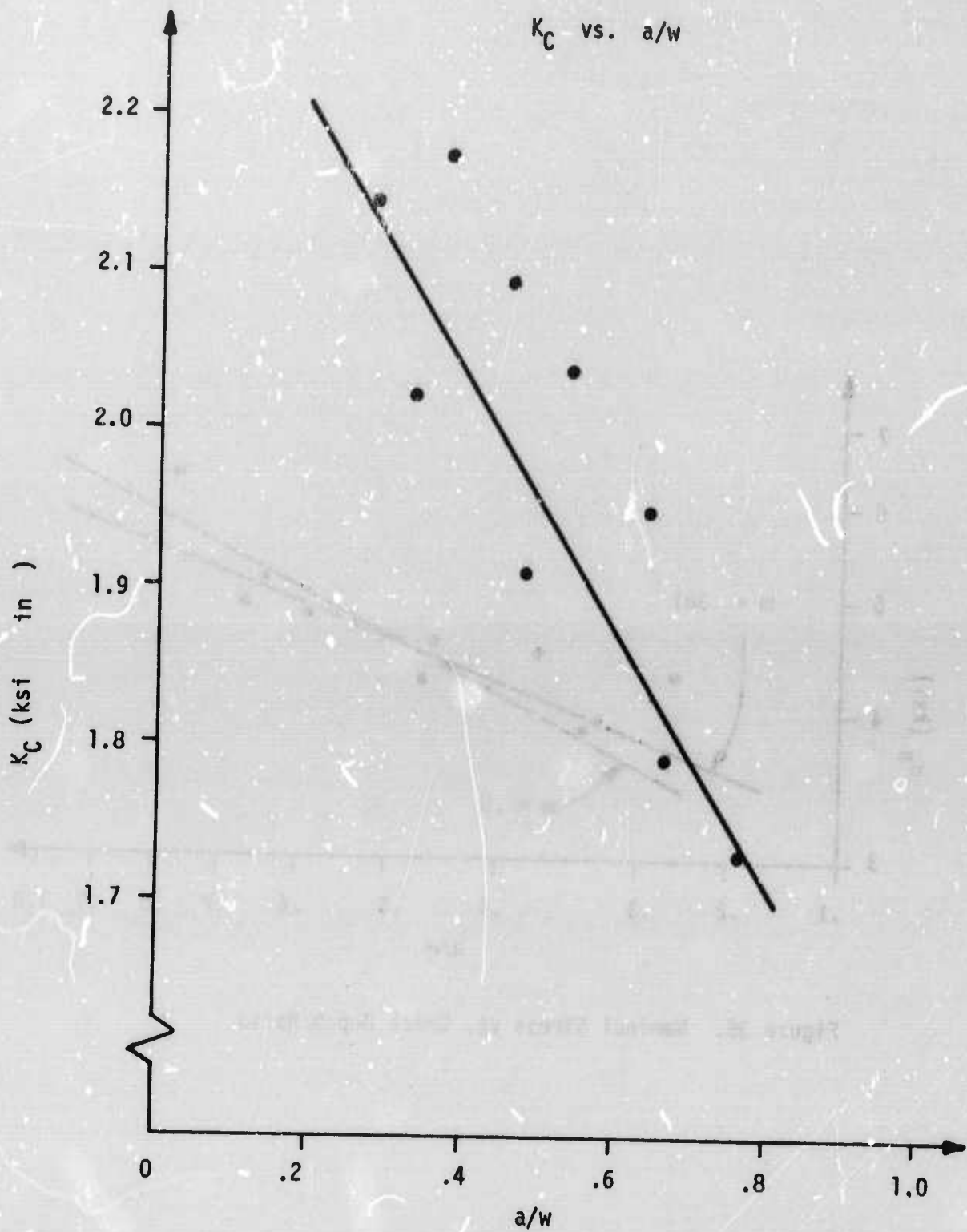


Figure 37. Stress Intensity Factor vs. Crack Depth Ratio

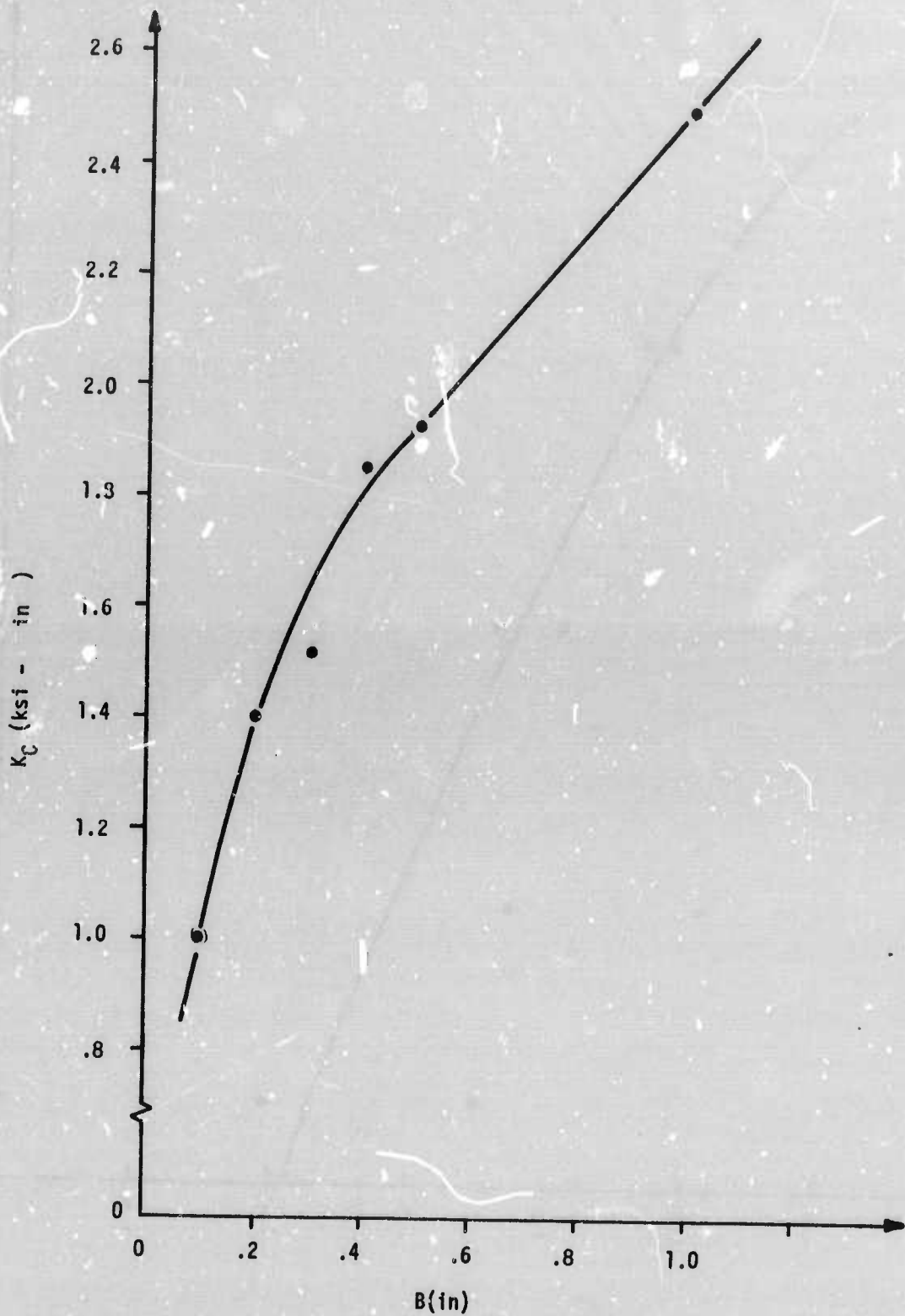
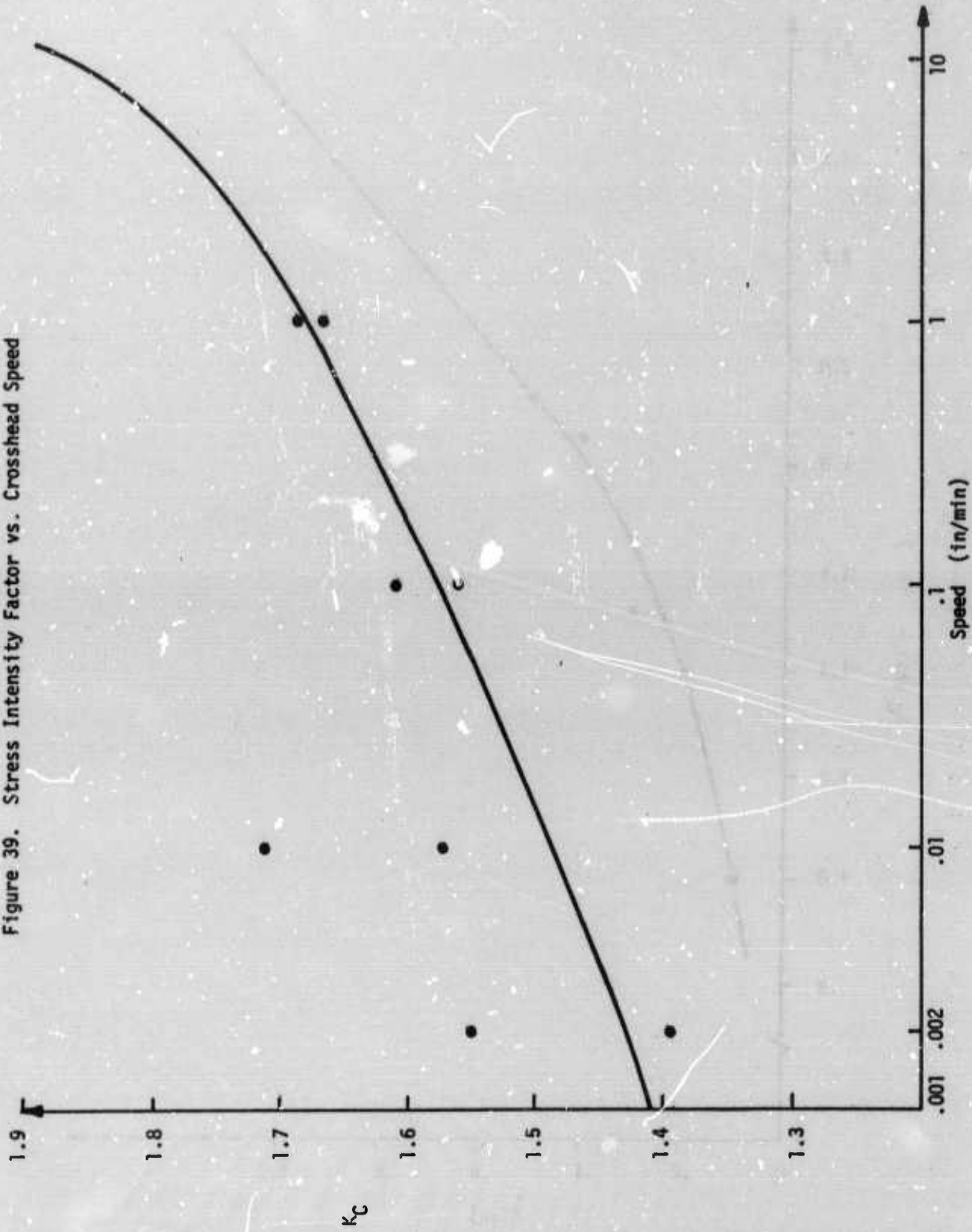


Figure 38. Stress Intensity Factor vs. Specimen Width

Figure 39. Stress Intensity Factor vs. Crosshead Speed



and testing a specimen this large make it prohibitive. Even though the data presented is not immediately useful in design, it may be helpful in understanding the phenomena of the plane stress fracture.

2. Crossplied specimens

Preliminary investigations have been done on crossplied specimens of varying fiber orientation. Figure 40 shows the plot of K vs. fiber angle orientation α is the plus and minus fiber angle orientations from the direction of crack propagation (see Figure 40 insert). Isotropic stress intensity factor analysis has been used although theory shows this not to be valid for the general anisotropic case. Further studies similar to those performed on the unidirectional specimens are planned for this specimen.

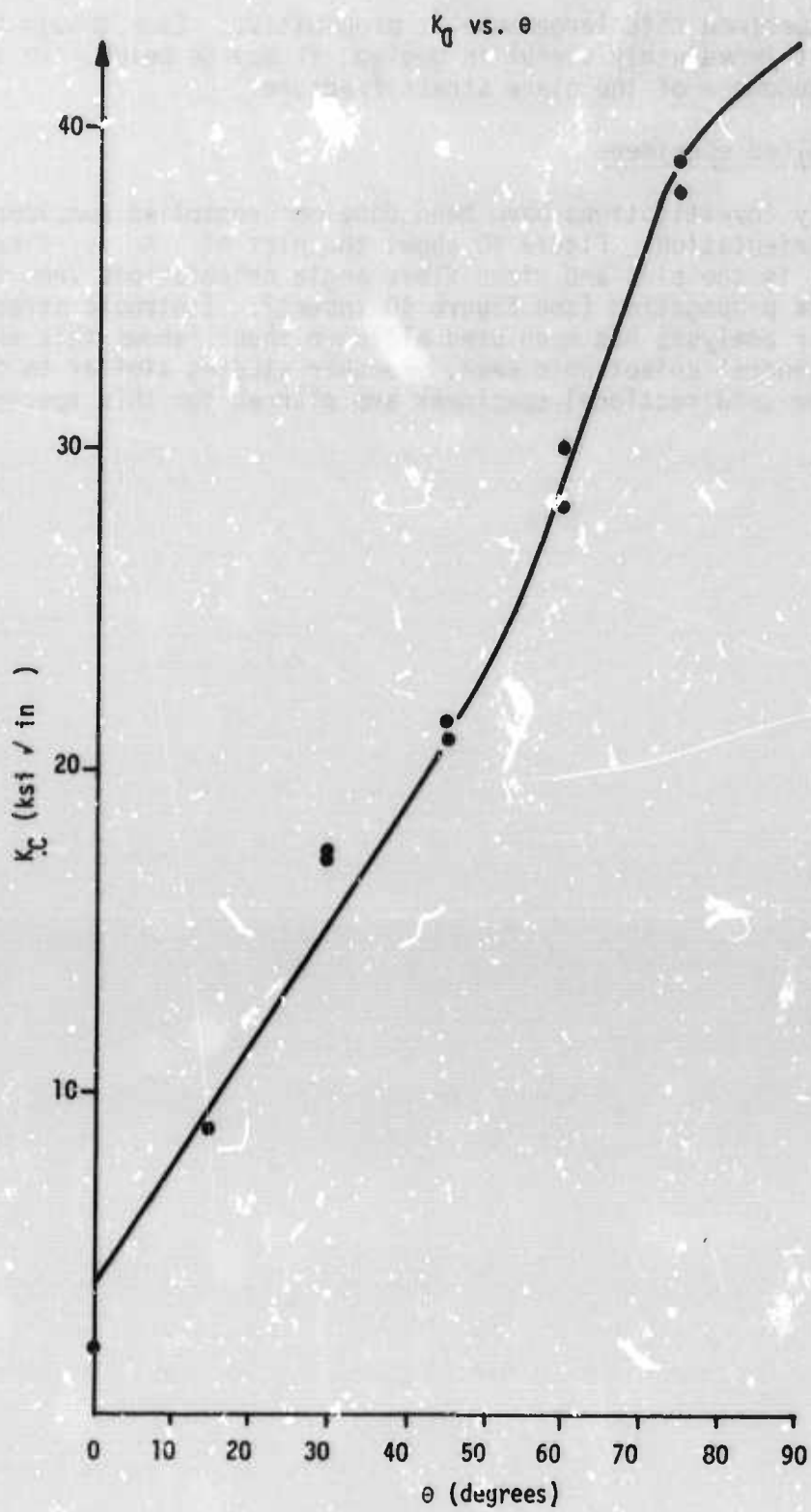


Figure 40. Stress Intensity Factor vs. Ply Angle

C. Time Dependent Properties of Fiber Composites
(Dr. R. E. Smith, Union Carbide)

Orthogonal ply graphite-fiber, epoxy-matrix composites are frequently found to have small cracks running through each ply even prior to testing. (2, 34) An example of these cracks is seen in Figure 41. Although these cracks appear to have little influence on the composite ultimate strength or Young's modulus in the directions of the fibers, their effect on time dependent properties (fatigue, creep, or stress rupture), on resistance to corrosive environment, or on off-axis static properties has not been studied in detail. Since plies with cracks are sometimes considered to have already failed, the effective utilization of graphite-fiber composites may depend on a thorough understanding of the interaction of these cracks with the stress state of the composite.

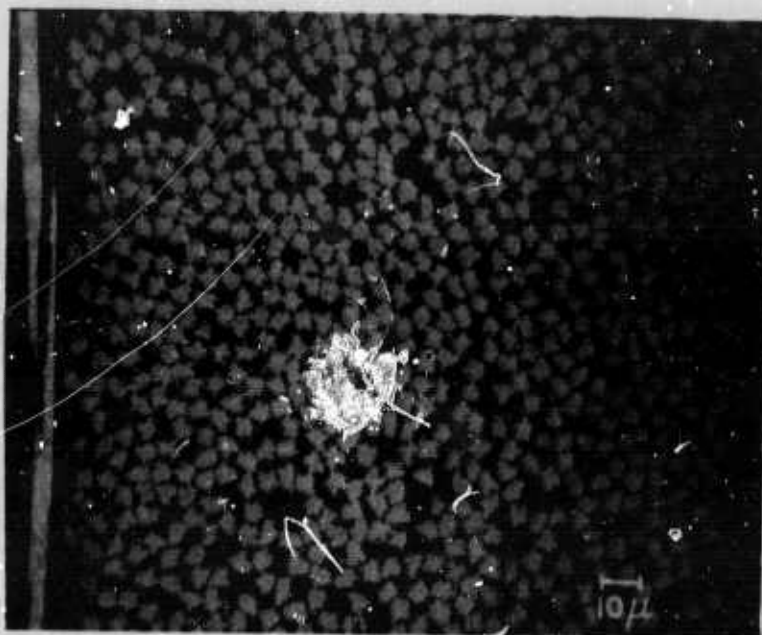


Figure 41. Cracks in an "As Fabricated" "Thornel" 50 Plate.

N-22511

Doner and Novak (34) have studied the crack network under conditions of repetitive loading of composites of "Thornel" 50 in various resin matrices. Their work was limited to fewer than 1.4×10^3 cycles on material that, because of the low bonding strength of resin to untreated fiber, had a large number of cracks in the as-fabricated state. The goal of this project was to extend our knowledge of composite cracking by using "Thornel" 50S yarn which had been treated to provide strong fiber-matrix bonding, and by extending the range of test conditions to sustained loading of up to 1000 hrs and to fatigue cycling for up to 1×10^6 cycles. It was hoped that the better bonding character of the treated yarn would give an essentially crack-free composite with which to study the growth and multiplication of cracks under stress. It was expected that degradation of the composite tensile strength and initial modulus with repeated stress could be correlated with the increased cracking in a useful way.

The composite plates fabricated for this program were 12" square flat panels with 7 plies of "Thornel" 50S, ERLA 4617/MPDA in a 0° - 90° orthogonal layup with the 0° direction corresponding with the fiber direction of four of the plies. The properties of the plates and plate constituents are listed in Table IX. Two sample geometries were used, one for sustained loads and one for fatigue loads. Samples for sustained loading were 1 1/2 inches wide, necked to 1/2 inch, and 10 1/4 inches long. Reinforcing doubler plates cut from stock sheet steel were bonded to the samples, and the sandwich was drilled for pin loading. The samples for fatigue loading were 9 inches long and 1/2 inch wide with fiber glass doublers.

TABLE IX
PHYSICAL PROPERTIES OF PLATES AND CONSTITUENTS

Property	Plate					
	1	2	3	4	5	6
Tensile Strength (ksi)						
Yarn	220	220	220	220	220	200
Resin	19	19	19	19	19	19
Plate (0° direction)	55	66	68	62	67	72
Initial Modulus (10^6 psi)						
Yarn	52	52	52	52	53	58
Resin	.78	.78	.78	.78	.78	.78
Plate (0° direction)	15.2	15.3	14.5	15.7	18.8	17.3
Shear Strength (ksi)						
Yarn	8.2	8.2	8.2	8.2	8.0	7.3
Resin	15	15	15	15	15	15
Yarn Volume Content (%)	52	56	52	56	60	57

The sustained load tests were conducted on Satec, Model D, creep rupture testers. Specimens had strain gages on each side which monitored the strain as the test progressed. The specimens were loaded to different stresses for 1000 hours with the exception of three specimens from which the load was removed at 2, 20, and 200 hours. Fatigue cycling was carried out on a Gilmore Universal Testing machine which is of a servo-controlled hydraulic design. Tests were run in a tension-tension mode at 6 cycles/sec with the minimum load approximately 1/10 of the maximum load.

For purposes of determining desired stress levels in sustained load or in fatigue and as a basis for comparison of the effects of dynamic loads, it was necessary to know the tensile strength and modulus to be expected of each specimen; however, the limited number of specimens obtainable from each plate precluded a statistical evaluation of the tests in this program. The tensile strength of the plates used in the sustained load tests were estimated by stressing one specimen from each plate to failure. More measurements of modulus were included to determine the effect of stress on modulus. In the fatigue program, more specimens were available, and baseline strength and modulus were determined from the average of three tests. Optical counting of cracks was chosen to provide straightforward comparison with existing data. (34) The results of optical crack counting are presented in this report in terms of the "crack density," which is defined here as the number of cracks observed in a section of the specimen divided by the product of the length of the specimen and the number of plies being examined. The crack density will be given in units of cracks/mm/ply. So that the major source of error in optical counting might be minimized, i. e., finding a representative cross-section, each specimen was cut into several sections. Sections were taken near each end of the gage section and from the center. This method of sectioning permitted us to determine the degree of uniformity of the crack distribution.

Experimental Results. One of the prime goals of this program was to study the onset of cracking in an initially crack-free composite. Other studies (34) had found cracks in all composites of "Thornel" 50 and resins which were cured at high temperatures. All of the plates fabricated by Union Carbide for this program were essentially crack-free, a condition which is unusual for cross-ply graphite-fiber composites and is probably due both to the high shear strength of the yarn (7 ksi vs. 4 ksi in Reference 34) and to the fabrication technique. Many sections of the plates were checked metallographically, and some porosimetry work was also carried out, but no measurable cracking was found. The microstructure of the plates was excellent; the fiber distribution was uniform, and there were no cracks and no voids. The plates were further characterized by measurements of the ultimate tensile strength (UTS) and the modulus (E) and by scanning electron microscopy (SEM) of fracture surfaces. Table IX shows the UTS and E values for the six plates used. The stress-strain curves for all specimens were nonlinear and appeared to consist of two linear regions. At low stresses (<10 ksi), there was a linear region with modulus E_1 , the initial modulus; at high stresses (>20 ksi), there was a second linear region with a modulus $E_2 > E_1$.

In order to provide a basis for comparison for long term and cyclic loading, the crack density was measured in several specimens after they had been taken to various stresses applied in the 0° direction and returned to zero stress. These "single cycle" crack densities are presented in Table X and Figure 43. Table X shows that the crack densities correlate well with the single cycle "strain" calculated from the applied stress and the average initial modulus. The "strain" thus calculated is merely indicative, since it does not take into account the variability of sample properties or the nonlinearity of the stress-strain curve. There appears to be a threshold for crack creation in the neighborhood of a "strain" of .30 percent. Below this value, the crack density is at or below the threshold of detectability; above .30 percent, the crack density increases rapidly with increasing strain. Table X shows the cracking only in the 90° plies; the crack density in the 0° plies, where the stress is not oriented so as to open cracks, was generally below the detectability threshold and is not listed. The nature of the cracking is shown in Figure 42, which is a cross-section of a sample listed in Table X which had seen a stress of 93 percent UTS with a "strain" of .37 percent. The cracking induced by stress appears in every way similar to that which occurs during fabrication.

TABLE X
CRACKING DUE TO SINGLE CYCLE STRESS

Plate No.	Single Cycle Stress (% of UTS) (ksi)	Single Cycle Strain (%)	Crack Density in 90° plies (cracks/mm/ply)
4	58	36	.23
	93	58	.37
	99	61.5	.39
3	74	50	.35
	83	56	.39
5	80	54	.29

Figure 43 presents the crack density results for the sustained stress samples. The samples were tested in two groups. The first group was started in August 1969 and the second group in December 1969. There is a marked difference in the crack density of the two groups. The four samples from the first group show "normal" crack densities compared with the single cycle stress samples and are presented in Figure 43. The crack densities are higher for a given strain, which might be interpreted as additional damage due to the sustained loading. The trend of crack density with strain is the same. The results from the second group were completely unexpected.



Figure 42. Cracks in Plate No. 4 Due to One Cycle Stress of 93 Percent UTS.

N-22509

The crack densities were much too low in comparison with samples from the same plate in the first group and with the single cycle stress samples and are not shown in Figure 43. The strain during the sustained loading was monitored and shows a rapid initial permanent deformation in the first few hours with very little deformation thereafter. The permanent deformation was small, approximately 60μ inches/inch at stress levels of 50 ksi (75 percent UTS), and showed no differentiation among groups of samples. The change in modulus due to sustained load was measured and found to be insignificant.

The results of fatigue cycling for 1×10^5 cycles at various stresses are also presented in Figure 43 and the results of cycling for a range of number of cycles at constant stress are presented in Table XI. There is a tendency for increased stress or increased number of cycles to produce increased crack density, but there are two anomalous features which limit the validity of any conclusions. First, some samples show unusually low crack counts for the stress and cycle conditions, just as in the sustained load samples. Second, there is frequently a large discrepancy between the crack densities of samples subjected to essentially identical stress-cycle conditions.

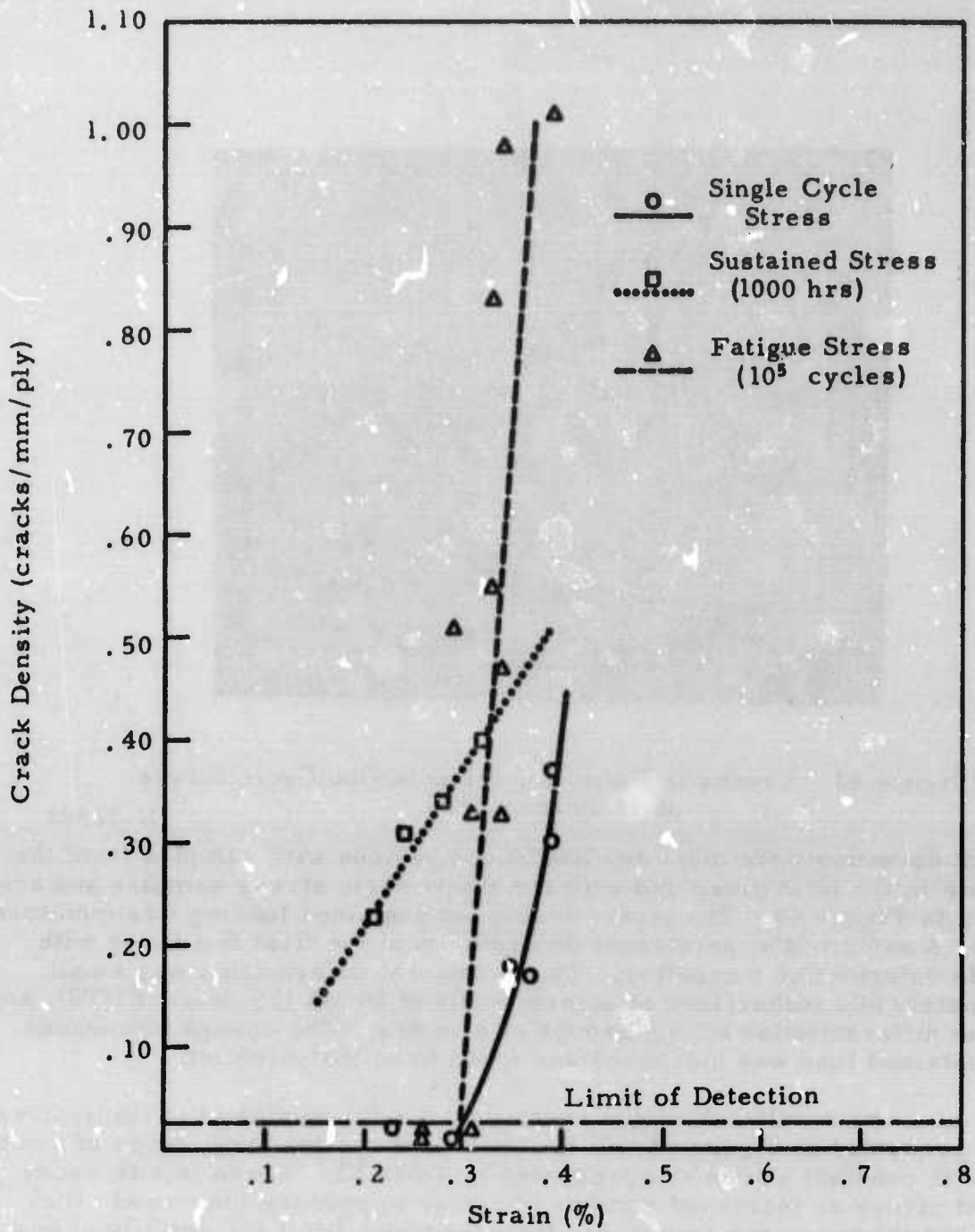


Figure 43. Crack Density Produced by Various Strain-Time Conditions.

G-700137

TABLE XI
CRACKING DUE TO FATIGUE CYCLING AT CONSTANT STRESS

Specimen	Maximum Stress (ksi)	Maximum Strain (%)	Number of Cycles	Crack Density (cracks/mm/ply)
5-13	54	.29	1	.01
5-19	54	.29	10	.11
5-16	54	.29	1×10^3	0.0
5-8	54	.29	1×10^4	.04
5-7	54	.29	1×10	.51
5-11	54	.29	1×10^6	.67
6-2	57.5	.33	10	.03
6-14	57.5	.33	10	.03
6-1	57.5	.33	1×10^3	.12
6-7	57.5	.33	1×10^2	.39
6-15	57.5	.33	1×10^4	.25
6-9	57.5	.33	1×10^4	.20
6-10	57.5	.33	1×10^5	.55
6-12	57.5	.33	1×10^5	.83
6-4	57.5	.33	1×10^6	1.65
6-16	57.5	.33	1×10^6	.69

The tensile strength and modulus are not much affected by fatigue cycling, as shown in Table XII. There may be a modest decrease in UTS for the high strain cycling and an increase for the lower strain conditions. The small number of samples tested makes the apparent increase in UTS for Plate 5 after fatigue statistically inconclusive, but the result is consistent with that of other investigators. (35) In any case, fatigue cycling does not adversely affect the tensile strength of the composite.

TABLE XII
MODULUS AND STRENGTH OF FATIGUED SPECIMENS

Plate No.	Number of Cycles	Maximum Stress (ksi)	Maximum Strain (%)	Tensile Strength (ksi)	Initial Modulus (10^6 psi)
3					
baseline	---	---	---	68	14.5
fatigue	1×10^5	56	.39	66	15.3
5					
baseline	---	---	---	65, 67, 69	18.8
fatigue	1×10^4	58	.31	69, 71, 74	19.0
	1×10^5	58	.31	66, 68, 71	18.2
	1×10^6	58	.31	72, 75, 76	19.3

In an attempt to evaluate the crack density of samples which had failed, we found that fractured specimens had a very nonuniform crack count. The crack density was very high near the point of fracture and fell off steadily as a function of distance from the fracture. Intact specimens from the sustained loading and fatigue cycling occasionally also showed striking nonuniformities of crack density, varying by a factor of 2, but there was no consistent trend for cracking to be high near the grips, for instance.

The problems of abnormally low crack densities, lack of reproducibility of crack densities, and nonuniformity of crack densities make difficult the meaningful interpretation of data generated during this program. These three problems are very likely due to one or more of the following causes: intrinsic sample variability, sample preparation, variability in test conditions, or variability in post-test examinations. No single explanation seems entirely sufficient. Testing conditions were monitored as carefully as possible. Sample preparation and examination, which might create cracks, would hardly generate crack densities which vary smoothly with test strain. Sample variability is inadequate to explain the low cracking in all of the second group of sustained load specimens.

The lack of reproducibility of crack densities in samples fatigued under the same nominal conditions may be easier to explain. Although the samples were loaded to a constant maximum stress, Table XII indicates that a constant maximum strain is more relevant to cracking. The rapid variation of crack density with strain coupled with the normal sample-to-sample variation in modulus (and, hence, strain for a given stress) could well account for the lack of reproducibility of crack density. A crude estimate from Figure 43 indicates that a variation in strain of 10 percent is capable of producing a variation of a factor of two in the crack density for single cycle stress and, presumably, also in the fatigue-induced crack density.

The nonuniformity of crack densities in fractured samples can be explained in two ways. In fracture, the elastic strain energy is released suddenly as a shock wave which propagates down the sample, gradually diminishing in intensity. The cracking would be indicative of the shock amplitude. The principal problem with this interpretation is that the crack densities far from the fracture were observed in most cases to be lower than those expected from Table X. This condition would seem to indicate that the crack density can build up locally, around a stress concentrating defect, for instance, and relieve the strain in the 90° layers elsewhere in the sample. The nonuniformities of the crack density of intact fatigue specimens may be related to this effect and may indicate the probable region of ultimate failure of the specimen.

In view of the crack anomalies, there is little in the way of analysis that can be done on the cracking due to sustained loads. Samples may or may not have cracking for reasons which may only be guessed. The primary effect of the sustained stress seems to be to lower the apparent threshold strain for crack creation from .3 percent for single cycle stress to less than .2 percent for sustained stress. Since cracking varies with strain rather than stress, it is not possible to specify the crack density for a plate at a given stress, such as the design limit of 2/3 UTS; however, for a plate typical of this program

(68 ksi UTS and 18×10^6 psi modulus), the crack density after 1000 hours at $2/3$ UTS would be approximately .30 cracks/mm/ply (or fewer, if the unknown conditions causing low crack densities are met). The permanent deformation in these composite specimens is small and correlates reasonably well with either strain or stress. In particular, there are no obvious anomalies in the second group. This fact would appear to indicate that the permanent deformation is not related to the creation of cracks.

Fatigue cycling does not appear to have a strong effect on the threshold strain for crack creation but does strongly affect crack density above the threshold. Thus, for the "typical" specimen discussed above, fatigue for 10^5 cycles at $2/3$ UTS would create few cracks. This result was inadvertently verified early in the program when the fatigue machine failed to follow the set load and a run was made at a stress $\leq 2/3$ UTS. No cracks were found in this specimen.

The trend in crack density in this program may be discussed in comparison with the results of Doner and Novak. (34) They find that crack density increases with stress but that the density is not the same for different plates for the same stress as a percentage of UTS. This result is consistent with the finding of this program that cracking is related to strain. Doner and Novak also find that cracking occurs mainly during the first cycle, whereas this study shows that cracking increases steadily with number of cycles. This disagreement is probably due largely to the different materials involved. In this study, the crack density at 10^6 cycles and a stress of 80 percent UTS was less than that which Doner and Novak found after one cycle at 40 percent UTS in their lower shear strength material. In any case, cyclic loads at stresses up to 85 percent UTS and for up to 10^6 cycles appear to produce no degradation of tensile properties (Table XII and references 34 and 35). In fact, there may even be a slight strengthening effect of fatigue, perhaps due to the relief of thermal stresses.

The crack inducing character of fatigue differs from that of sustained stress (Figure 43). Within the limits already discussed, the sustained stress appears to lower the threshold strain for crack creation but does not affect the slope of the crack density-vs-test strain curve much. Fatigue for 10^5 cycles, however, does not appear to affect the crack threshold, but it does appear to increase the slope of the cracking-strain curve dramatically.

D. Notch Sensitivity of Fiber Composites
(Dr. R. E. Smith, Union Carbide)

The objective of this work was a comparative evaluation of the notch sensitivity of "Thornel" 50S, ERLA 4617 epoxy and P-1700 polysulfone composites. Since polysulfone resins are tougher and have much higher elongations to failure than the relatively brittle epoxies, it was expected that the polysulfone composites would be less notch sensitive. Polysulfone composite plates became available only at the very end of this program; thus, only a small number of experiments were performed.

A 12-inch square 7-ply (0° , 90°) plate of "Thornel" 50S/ERLA 4617/MPDA composite was cut into seven specimens according to standard specifications (MIL-Handbook-17, pg. 2-29). The specimens were 1 1/2 inch wide, necked to 1/2 inch by arcs of 4 inch radius. A 1/8 inch hole was drilled into the center of the necked section in four of the specimens. The failure stress was calculated from the failure load, and the remaining cross-sectional area was determined from a micrometer measurement of neck width, thickness, and hole diameter. Reinforcing doublers similar to those used in the fatigue-cracking program were employed. In addition, a 12-inch square 7-ply ($\pm 45^\circ$) plate was prepared from the same prepreg and cut similarly to test the variation of notch sensitivity with ply orientation. The fabrication of polysulfone plates is reported in Volume I (Materials Research) of this Report. Since it was difficult to prepare large polysulfone plates, it was not possible to cut standard specimens. We decided to try samples 8 inches long by 1/2 inch wide, similar to the fatigue samples, with the same doublers as in the fatigue program. One plate (PS-08270) of "Thornel" 50S/polysulfone was chosen for this work, based on this microstructural examination (Figure 44). Six specimens were cut from this 12-inches by 4-inches plate. Three of these samples had holes drilled into the center of the gage section. So that this change in specimen geometry could be evaluated, three "Thornel" 50S, ERLA 4617 specimens of this straight-sided geometry were also tested for notch sensitivity. These samples were cut from fatigue Plate No. 6. (Table IX, Section VI-C of this report).

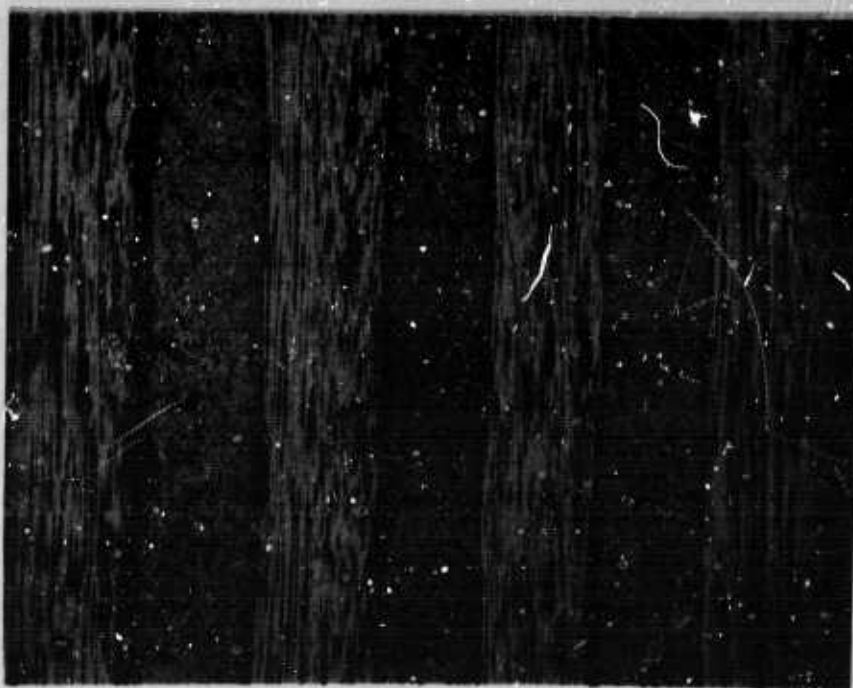


Figure 44. Microstructure of Plate PS-08270.

P700158

Table XIII presents the results of the notch sensitivity testing. The necked epoxy composite specimens lost 30 percent of their strength when tested along a ply direction and less than 2 percent of their strength when tested at 45° to the ply directions. The straight-sided geometry epoxy composite specimens tested along a ply direction lost 18 percent of their strength. All of the epoxy specimens failed in a "normal" manner: the 0° failures were brittle with irregular failure surface and the 45° failures failed along the fibers leaving a sawtooth surface. The polysulfone composites appear to have no notch sensitivity when tested along a ply direction, a conclusion which is somewhat tentative because the unnotched (baseline) specimens all failed in the grips; thus, the reported baseline failure stress is only a lower limit. However, the failure stress of 64 ksi of the notched specimens is close to that expected on a rule-of-mixture basis.

TABLE XIII
COMPOSITE NOTCH SENSITIVITY

Specimen	Control		Notched		
	Strength (ksi)	No. of Tests	Strength (ksi)	No. of Tests	Strength Loss (%)
Epoxy					
Necked (0°, 90°)	51	3	35.2	4	31
Necked (±45°)	14.6	3	14.4	4	2
Straight (0°, 90°)	71.9	3	59.1	3	18
Polysulfone					
Straight (0°, 90°)	61.2	3	64.3	3	0

E. Influence of Defects on Composite Properties
(Dr. T. Weng, Union Carbide)

Earlier in this program (3), four 12-inch square panels which contained a variety of known intentional defects were fabricated for use in evaluating nondestructive test methods. The panels were made from "Thornel" 40/ERL 2256/MPDA and had a balanced orthogonal lay-up. Two panels were made with four plies and two panels were made with 12 plies. Defects consisted of Mylar and off-axis yarn inclusions between plies, butt joints, lap joints, and resin-rich and resin-starved areas. These defects were thought to be representative of those which might occur in composite fabrication.

After nondestructive testing was carried out at AVCO Corporation (36), test specimens were cut from these plates to evaluate the effects of these defects on the tensile, flexural, and compression strength of the composite. The sonic modulus of the specimens was also measured prior to the static destruction tests. The test results are listed in Table XIV.

Butt joints and lap joints reduced the tensile strength by approximately 25 percent. Double yarn inclusion had no apparent effect on tensile strength. Butt joints and lap joints appear to have only a minor degrading effect on flexural strength, but caution may still be required because the effects on flexural strength depend not only on the type of defect but also on its location. The defects in the flexural specimens were located at approximately one-fourth of the thickness from a surface, but it was not known whether they were located in the tensile or compressive region of the specimens. The effect of defects on compressive strength was smaller than that on tensile strength. It is probable that stress concentration from the defects are smaller under compressive loads than under tensile loads.

TABLE XIV
EFFECT OF KNOWN DEFECT ON COMPOSITE STRENGTH

Plate Number	Test	Defect	Sonic Modulus (10 ⁶ psi)	Strength (psi)	Strength Retention (%)
3 4 ply (0°, 90°)	Tension	Control (2) (a)	11.6	64,200	100.0
		Butt Joint (2)	11.6	46,700	72.7
		Double Inclusion Yarn (1)	11.8	61,300	95.4
2 12 ply (0°, 90°)	Tension	Control (1)	11.4	59,000	100.0
		Lap Joint (2)	11.0	46,200	78.3
1 12 ply (0°, 90°)	Flexural (b)	Control (1)	9.5	67,500	100.0
		Lap Joint (2)	9.2	65,200	96.5
2 12 ply (0°, 90°)	Flexural (b)	Control (1)	11.6	78,400	100.0
		Resin Starved (1)	12.1	83,100	105.9
		Butt Joint (1)	10.7	72,400	92.3
4 4 ply (0°, 90°)	Compression (c)	Control (1)	10.7	42,400	100.0
		Butt Joint (1)	10.3	39,200	92.4
		Lap Joint (2)	12.3	37,400	86.2
		Mylar Inclusion (1)	9.6	36,300	85.6

(a) Number in parentheses is number of test sample.

(b) Single-Point loading.

(c) Fed. Test Method Std. No. 406.

F. Fracture Strength of Composite Cylinders Under Combined Stresses
(Dr. T. Weng, Union Carbide)

Experimental data on the stress-strain properties and fracture strengths of composites under combined stress loading are needed for evaluating the accuracy of various theories of fracture for fiber-reinforced composites. These data are not readily available to date on graphite fiber composites. Therefore, an experimental investigation was conducted to generate fracture data under combined stresses with which the various theories of fracture may be compared.

The fracture strength under uniaxial, torsional, and combined stresses and the stress-strain properties of "Thornel" 50S/ERLB 4617/MPDA composites have been determined. The composites were of four-ply (90°, 0°, 0°, 90°) construction, with a fiber content of 55 to 58 volume percent.

Torsional and combined stress tests were conducted on cylindrical specimens in the combined stress test apparatus described in a previous report. (5) The lay-up pattern of the cylindrical specimens was such that the 90° direction coincided with the tangential direction of the cylinder. The ends of the specimens were reinforced with fiber glass prepreg cloth and were attached to the steel fixtures with epoxy adhesive as shown in Figure 45. The dimensions of the specimens were: inside diameter, 2.01 in.; outside diameter, 2.08 in.; gauge length, 2.50 in.; and total length, 7.0 in.

Ten cylindrical specimens were fabricated with material from the same prepreg run. Two specimens were tested in pure torsion and eight were tested under combined loadings. The load conditions were selected to permit a determination of the approximate shape of the fracture strength surface encompassing the shear-tensile-tensile stress states. The results of the torsion and combined stress tests on the cylindrical specimens are given in Table XV.

In addition to the combined stress tests, the uniaxial tensile and compressive properties along the 0° direction were measured with (90°, 0°, 0°, 90°) and (0°, 90°, 90°, 0°) composite plates, and the short beam shear strength was measured with a fourteen-ply unidirectional composite plate. The results of these tests are summarized in Table XVI. Strength data given in Tables XV and XVI, except the short beam shear strength, are plotted in a three-dimensional graph with coordinates of shear, tangential, and longitudinal stresses shown in Figure 46. The uniaxial strength data are denoted with the shaded circles and combined strength data are denoted with the open circles. Curves shown in Figure 46 were drawn to indicate the probable fracture strength surface of the composite.

One cylindrical specimen (09140-1) was tested under internal pressure and axial compressive load. The objectives of this test were to simulate the condition of a hoop tensile test, where the magnitudes of the longitudinal and radial stresses are very small in comparison to the tangential stress and to examine the effects of end constraints on the specimen.

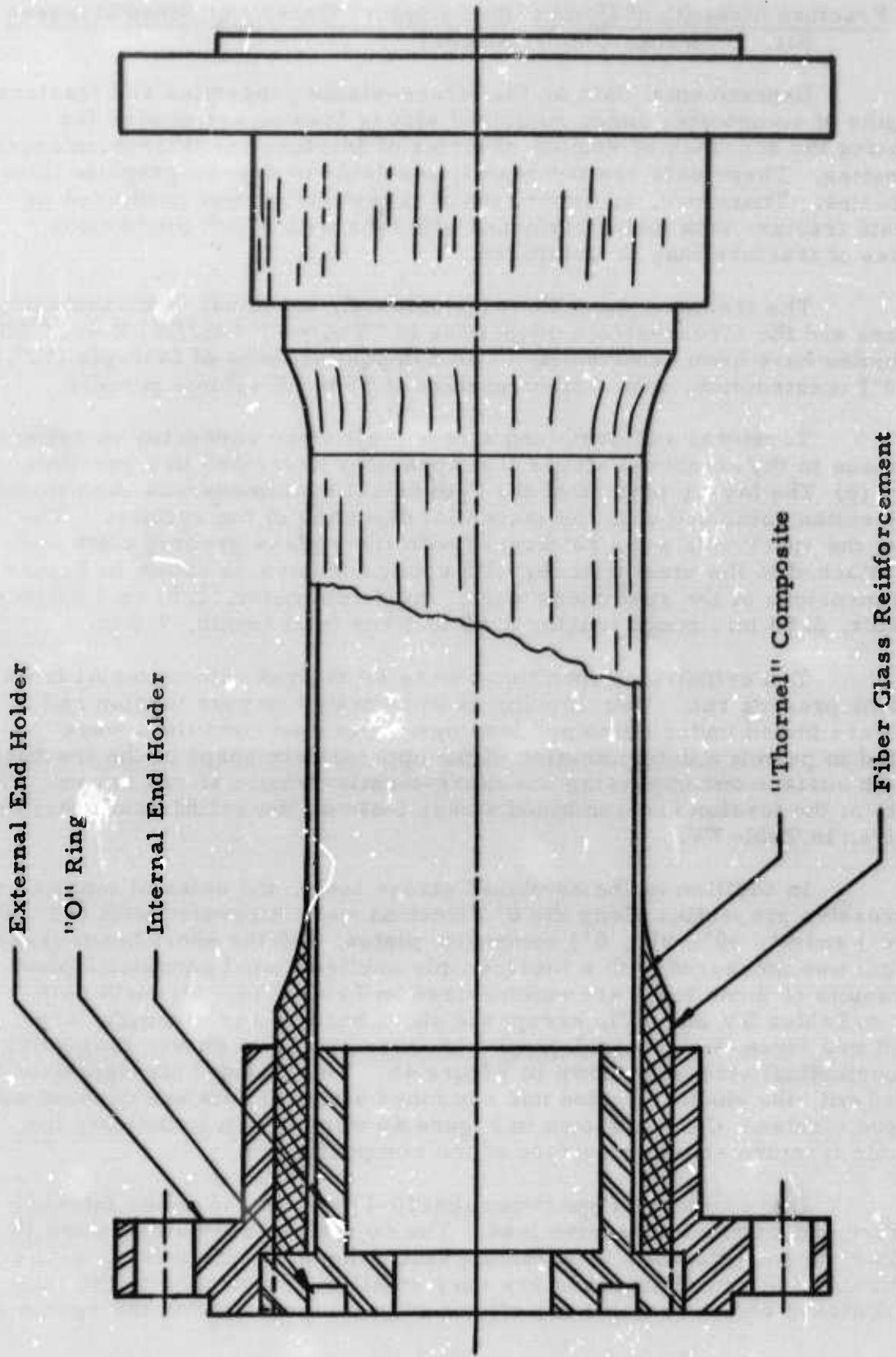


Figure 45. Combined Stress Test Specimen Assembly. G-710025

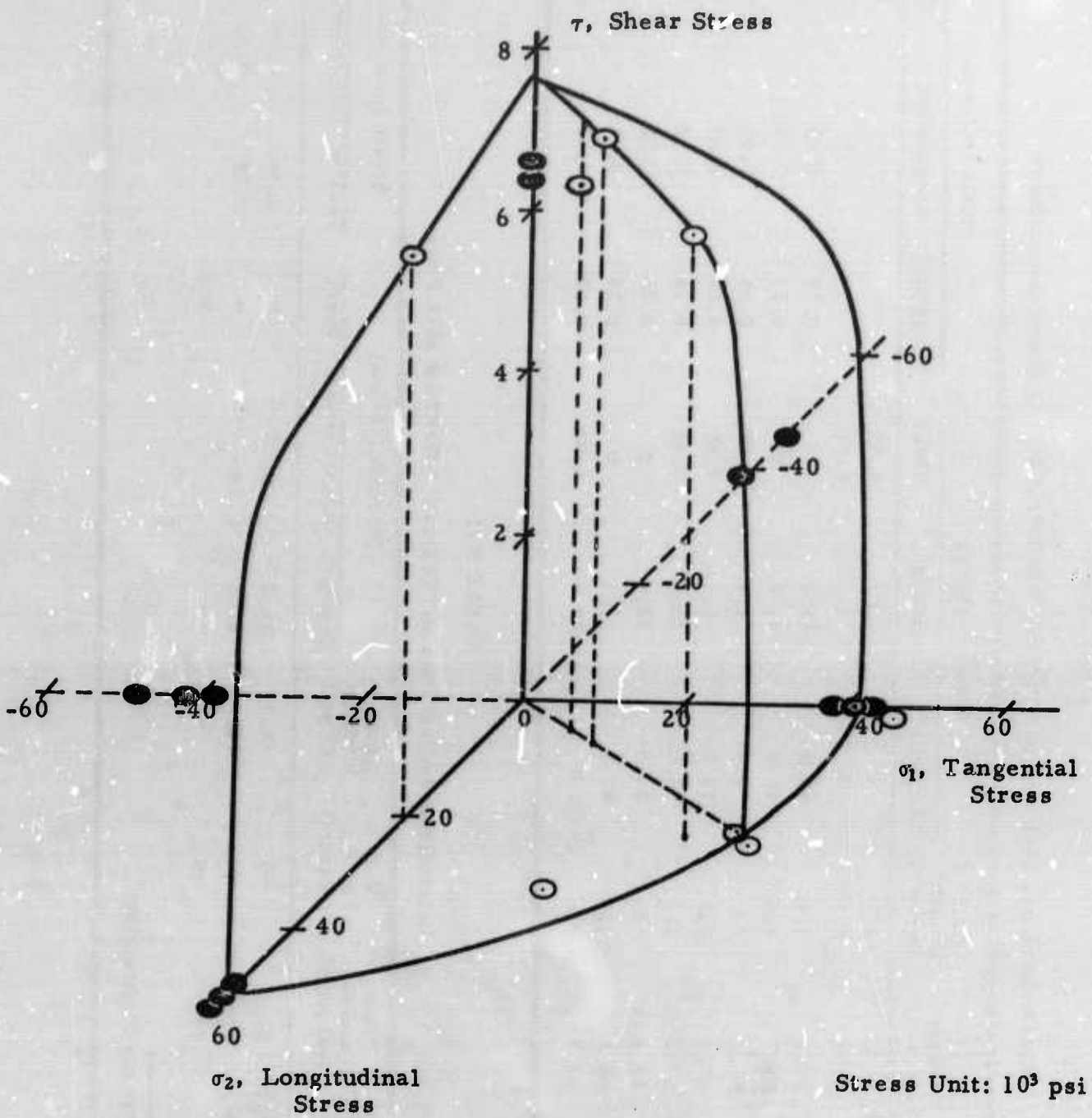


Figure 46. Fracture Strength Surface for Four-Ply ($90^\circ, 0^\circ, 0^\circ, 90^\circ$) "Thornel" 50S/ERLB 4617 Composite.

G-710026

TABLE XV

Combined Stress Test Data on "Thornel" 50S/ERLB 4617 Cylindrical Specimens

Specimen	Fiber Volume (percent)	Void Content (percent)	Strength (10^3 psi)			Strain (percent)		
			Tangential	Longitudinal	Shear	Tangential	Longitudinal	Shear
08100-1	55.2	3.1	0	0	6.58	~	~	1.22
08120-1	55.8	0.7	0	0	6.71	~	~	1.56
08310-1	55.7	1.4	45.6	23.2	0	0.27	0.13	~
08310-2	55.7	1.4	43.8	21.2	0	0.27	0.13	~
08260-1	57.4	~0	9.9	4.8	6.75	0.05	0.02	1.18
08260-2	57.9	0.5	13.1	6.4	7.55	0.06	0.05	1.45
09080-1	57.2	1.1	36.1	22.5	7.35	0.18	0.10	1.69
09080-2	58.3	~0	26.0	32.9	0	0.16	0.18	~
09140-1	56.2	0.8	47.7	1.1	0	0.28	0.02	~
09140-2	57.2	~0	0	21.0	6.85	-0.02	0.12	1.64

TABLE XVI

Uniaxial Stress Test Data on "Thornel" 50S/ERLB 4617 Plates

Plate	Fiber Volume (percent)	Void Content (percent)	Young's Modulus (10^6 psi)	Strength (10^3 psi)			Strain (percent)	
				Tensile*	Compressive*	Shear	Tensile	Compressive
90°, 0°, 0°, 90°	61.5	~0	15.7	51.4	42.7	~	0.34	0.35
0°, 90°, 90°, 0°	60.6	~0	16.0	41.2	43.3	~	0.25	0.30
1*(0°)	57.3	~0	~	~	~	9.2	~	~

*Tested in the 0° direction.

The specimen was first subjected to an internal pressure of 480 psi prior to the simulation of the hoop tensile condition. Tangential and longitudinal strains at the center of the gauge section and at the edge of the fiber glass reinforcement were measured. The magnitude of the tangential strain at the end was about 95 percent of that at the center. At fracture under internal pressure and axial compressive load, the tangential stress was 47,700 psi and the longitudinal stress was 1100 psi; therefore, the condition of the hoop tension was approximately obtained. Tangential strains at the center and end of the gauge section were found to be approximately the same at fracture. Therefore, the existing end constraints appeared to have no significant effect on the fracture strength of the composite since the tangential stress of 47,700 psi was about 15 percent greater than the uniaxial tensile strength determined in the 0° direction with the (0°, 90°, 90°, 0°) plate.

The strengths of the pure torsion specimens were low in comparison with the remaining combined stress test data. These specimens had some wrinkles on the outside surface in the gauge section and these defects could have affected their strength. A more realistic value of the shear strength has been estimated for the cylindrical specimens by extrapolation of the fracture strength of the cylindrical specimens tested under combined stress loadings to the condition of pure torsion (to the limit of zero axial load and zero internal pressure). The extrapolated fracture surface is shown in Figure 46, and the estimated shear strength was 7600 psi. However, this estimated value of shear strength is still lower than the shear strength value of 9200 psi which was measured by the short beam shear test on the fourteen-ply unidirectional plate. It is not known whether these two shear strength values should be identical, but this discrepancy could be due partially to the difference in the qualities of the cylindrical specimens and the plate. Microphotographs of the pure torsion cylindrical specimens, a typical cylindrical specimen subjected to combined stresses, and the fourteen-ply unidirectional plate are shown in Figures 47 to 50. Figure 47 is a microphotograph of specimen 08100-1 taken along the tangential direction of the cylinder. Figure 48 is a microphotograph of specimen 08120-1 taken along the longitudinal direction of the cylinder. Figure 49 shows a microphotograph of specimen 08260-2 taken along the tangential axis of the cylinder; this microphotograph illustrates the quality of the typical combined stress test cylinders. Figure 50 is a microphotograph of the fourteen-ply unidirectional plate. These microphotographs indicate that the quality of the cylindrical specimens has been improved markedly from that described previously. (5) In the pure torsion cylinders, there were more resin rich areas, voids between plies, and cracks within plies than desired. The typical combined stress test cylinders contained only a small amount of these defects. The quality of the fourteen-ply unidirectional plate was excellent. It is known that there are inconsistencies among the shear strength values measured by short beam shear test and pure torsion tests on tubular specimens and small solid rods, and this problem should be investigated further.

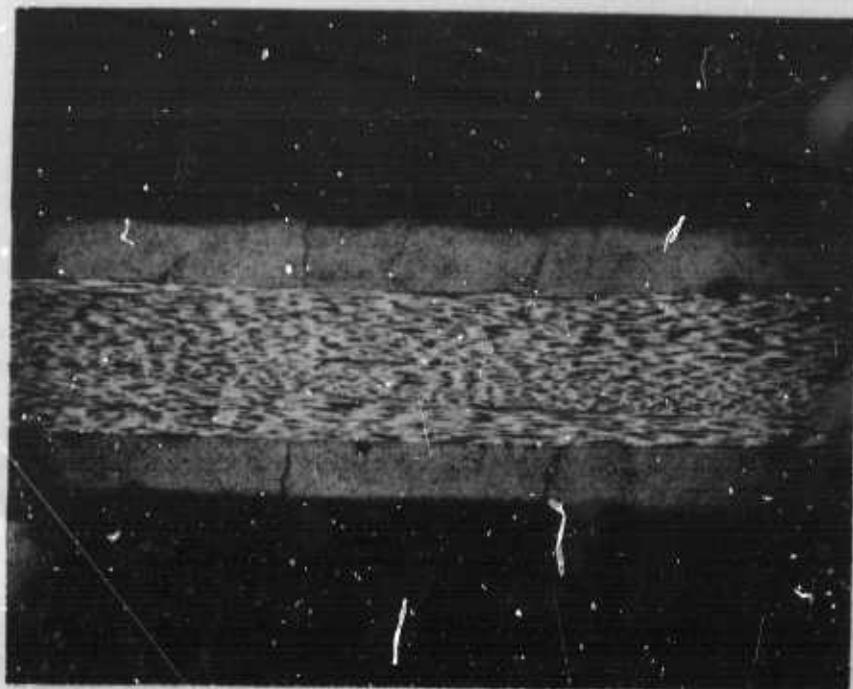


Figure 47. Microphotograph of Pure Torsion Test Cylinder (08100-1), Tangential View. (50X Magnification)



Figure 48. Microphotograph of Pure Torsion Test Cylinder (08120-1), Longitudinal View. (50X Magnification)

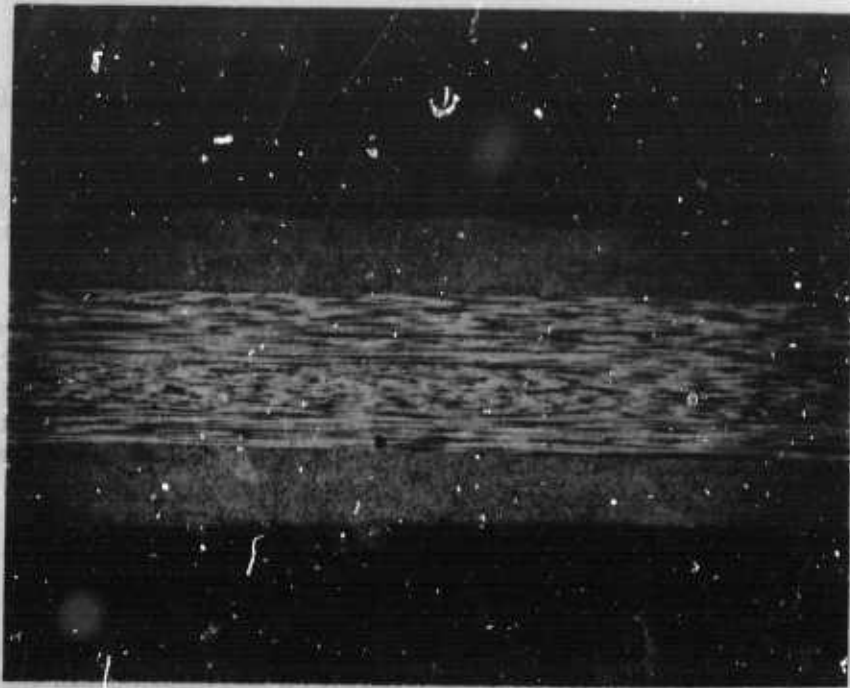


Figure 49. Microphotograph of Combined Stress Test Cylinder (08260-2), Tangential View. (50X Magnification)

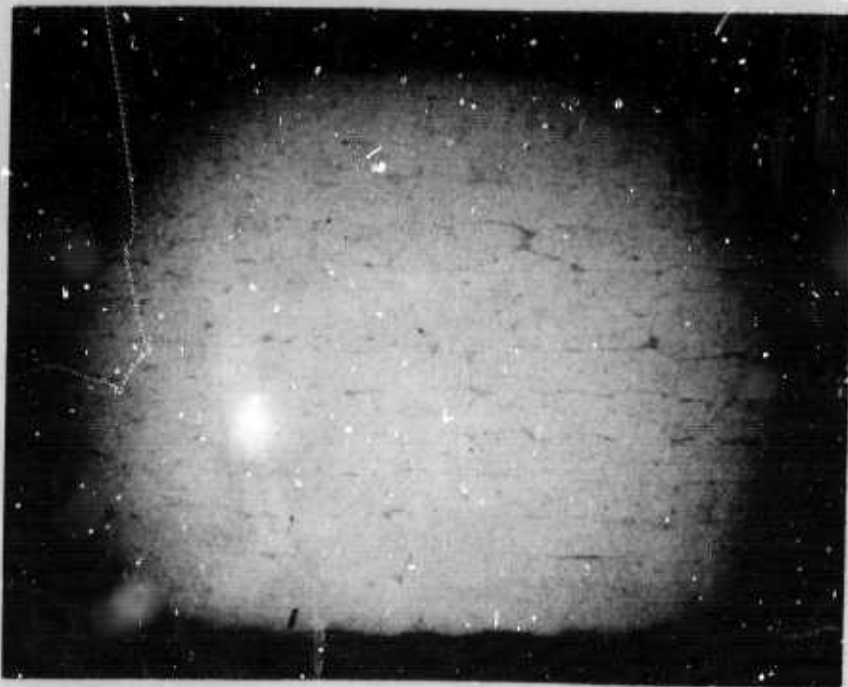


Figure 50. Microphotograph of 14(0°) Unidirectional Plate (T50S-09100-1). (30X Magnification)

The preliminary fracture surface shown in Figure 46 indicates that the ability of the composite cylinders to withstand torsional loads simultaneously with internal pressure and axial tension did not decrease appreciably until the magnitudes of the internal pressure and axial tension became relatively large. This characteristic of the composite is believed to be an inherent characteristic of the lay-up pattern.

Photographs of typical fractured specimens are shown in Figure 51. Shear failure in and between plies often occurred under pure torsional load. A longitudinal crack occurred, as expected, when a specimen was subjected to internal pressure. A fracture mode similar to that under pure torsional load was obtained for a specimen tested under torque and internal pressure, because the specimen was tested under a condition in which torque was dominant. The fracture mode for specimens tested under combinations of internal pressure, torque, and axial load differed and depended upon which loading was dominant in the test.

In future experiments, the fracture strength in other stress states, the effects of loading paths on fracture strength, and other lay-up patterns should be investigated. It was not possible within the remaining time of the contract to compare the fracture surface determined in the present experiments with fracture surfaces predicted analytically by current theories of failure, but the data should be of interest for such comparisons.

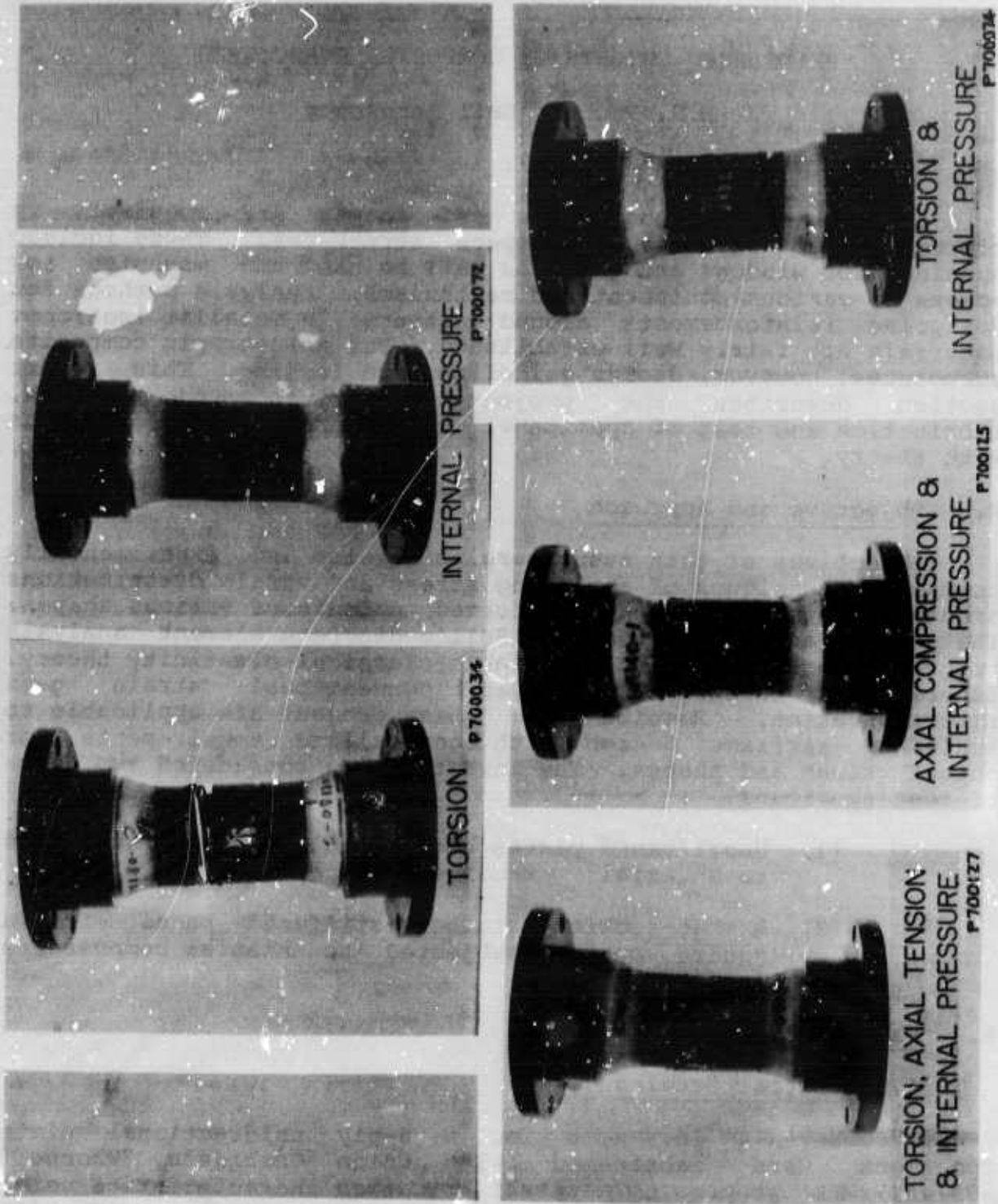


Figure 51. Fractured Cylindrical Specimens Subjected to Pure
 Torsion and to Combined Stresses.

SECTION VII

REINFORCED CUTOUTS IN COMPOSITE STRUCTURES

L.H. Kocher, Bell Aerospace

Cutouts of various sizes and shapes are required in virtually all airframe and space structures. These include openings for windows and doors as well as hand and manholes for access to various equipment and mechanisms. Analysis methods for designing reinforcements around cutouts in metallic isotropic materials are fairly well established. For anisotropic composite structures, however, design guidelines are lacking. This report section describes the project objectives and approach, fabrication and test of specimens, and correlation of results with theory.

A. Objective and Approach

Objectives of this study were to develop and experimentally correlate techniques of analyzing stress and strain distributions around unreinforced and reinforced cutouts of various shapes. The primary analytical tool was Bell's discrete element analysis program supplemented by available classical elasticity theory. Experimental techniques employed conventional strain gage instrumentation. Results from this project are applicable to scaled-up airframe design with generalized requirements for cutout sizes and shapes. The investigation considered two types of test specimens:

- (1) Unstiffened plates with circular cutouts subjected to uniaxial tensile loading, and
- (2) A hat-section stringer-stiffened panel with a square cutout subjected to uniaxial compressive loading.

B. Fabrication

1. Initial Studies

Seven 4 in. x 6 in. x 6-ply unidirectional plate specimens were fabricated with Union Carbide's "Thornel" 50S/4617/MPDA prepreg to assess fabrication characteristics using a variety of bleeder systems. Measurements at Union Carbide

Corporation on the prepreg indicated the following average characteristics:

Fiber	56.8	percent by weight
Resin	41.3	percent by weight with no volatiles
Finish	0.7	percent by weight
Volatiles	1.2	percent by weight
	<u>100.0</u>	

Yarn strand strength	247×10^3	psi
Yarn strand modulus	51.6×10^6	psi
Yarn density	1.724	g/cc
Yarn area/end	6.24×10^{-5}	in. ²
Resin density	1.27	g/cc = 0.0458 lb/in.
No. of ends/inch	72	
Torsion rod shear strength	6.3×10^3	psi

Measurements at Bell on the prepreg indicated 43.5 percent resin by weight and volatiles averaged 3.3 percent. The difference between UCC and Bell volatile contents was subsequently traced to a difference in test techniques. (Union Carbide: 15 minutes at 100° C in still air oven; Bell: 15 minutes in still air oven at 160° C.) The 4 x 6 in. panels were subsequently tested for in-plane notch shear and transverse tensile strengths(37). Table XVII summarizes the test data, Table XVIII defines the bleeder systems investigated. In all cases Union Carbide Corporation's recommended cure schedule was used:

Heat up to 200°F in not less than 15 minutes.
Hold 200-210°F for 60 minutes under pressure.

Increase temperature to 240°F in not less than 15 minutes, hold 240-250°F for 90 minutes.

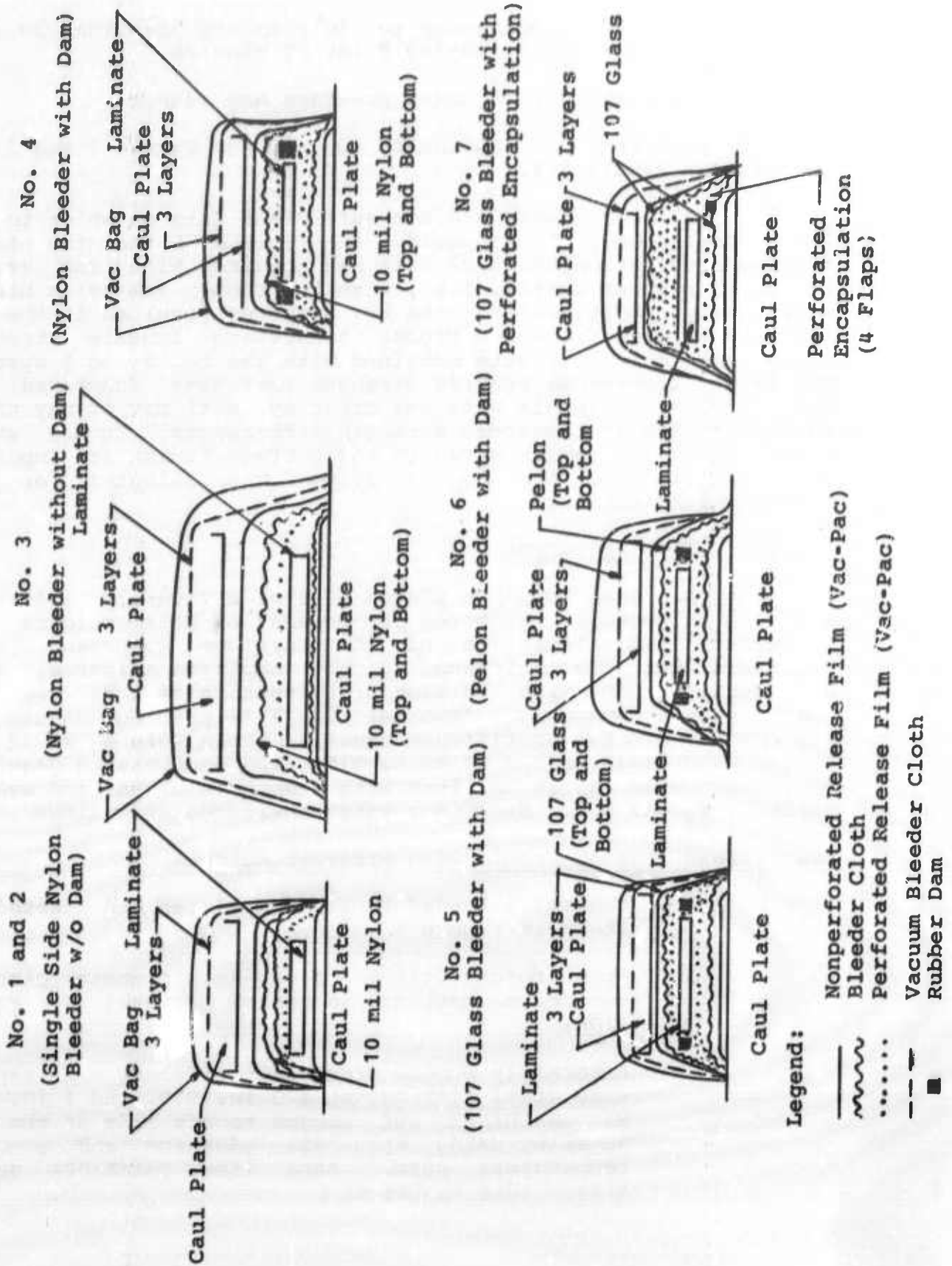
TABLE XVII

TEST RESULTS OF "THORNEL" 50S UNIDIRECTIONAL LAMINATES

Panel No.	Notch Shear Strength* (ksi)	Avg.	Transverse Tensile Strength (ksi)	Avg.	Avg. V _F (%)	Avg. V _V (%)	Thickness (in.)
1	2.72 3.25 4.45	3.48	-	-	55.5	3.14	0.049
2	4.06 3.47	3.77	3.50 4.28 4.08	3.95	55.6	3.74	0.047
3	4.75 5.66	5.22	4.27 2.71 3.13	3.37	57.8	3.50	0.045
4	3.76 3.54	3.65	-	-	56.1	3.09	0.048
5	3.69 3.64	3.66	4.16 2.39 3.62	3.39	56.4	3.22	0.045
6	3.69 3.44	3.57	3.09	3.09	55.8	3.73	0.046
7	5.13 4.30	4.71	3.94 4.60 4.23	4.25	57.5	3.09	0.048

* The notch shear stress concentration factor is 1.6. Therefore, "true", in-plane material shear strengths with this test range from 5.5 to 8.2 ksi corresponding to the values 3.48 and 5.22 ksi given in Table XVII.

TABLE XVIII
BLEEDER SYSTEM INVESTIGATION



Increase temperature to 330°F in not less than 30 minutes, hold 330-340°F for 90 minutes.

Cool to ambient under pressure and vacuum.

The cure pressures were nominally 400 psi for Panels 1 and 2 and 100 psi for Panels 3-7.

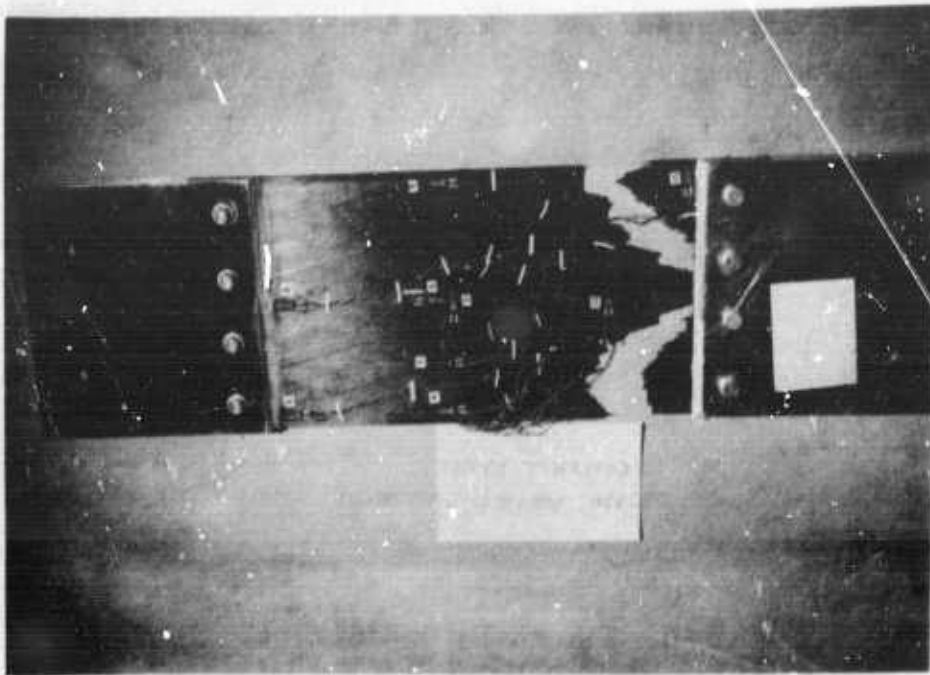
Although there are not sufficient data on which to base firm comparisons, it appeared in Table XVII that the highest average shear strength (5.22 ksi) was obtained with the use of the No. 3 bleeder system, i.e., with the rubber dam/nylon bleeder materials. Additionally, the No. 3 system resulted in the best laminate surface finish. Higher transverse tensile strengths (3.95 and 4.25 ksi) were obtained with the No. 2 and 7 systems. The latter transverse tensile strength increases (compared with the 3.1-3.4 ksi levels with the other systems) may or may not be as significant as the shear strength differences. In any event, since composite shear strength and surface finish are important in cutout studies, the No. 3 system was selected for test specimen fabrication.

2. Test Specimens

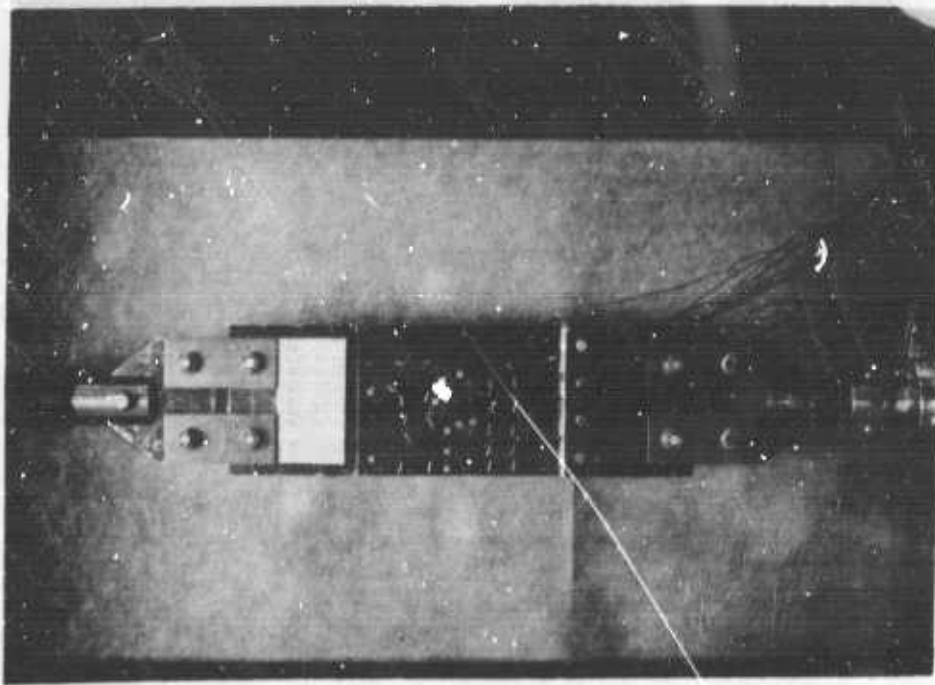
All test specimen plates were of a five-ply ($\pm 15^\circ$, $\mp 15^\circ$) construction, selected for reasons of balance (cured flat laminates) and simulation of the fuselage component skin. Stringers for the stiffened panels employed a four-ply ($\pm 10^\circ$, $\mp 10^\circ$) construction, with the same cross-section as that used for the fuselage component. "Thornel" 50S/4617 prepreg was used for all specimens. The unstiffened tensile panels were 6 x 12 in. plates with measured V_F s of 55 to 57%. The compression panel was 14.6 in. wide x 24 in. long with a skin V_F of 55% and average stringer V_F was 60%. Specimens were fabricated as follows.

Unstiffened Tension Panels with Circular Cutouts

- (a) Control - Bonded to loading plates and tested as shown in Figure 52(a).
- (b) Unreinforced Cutout - A one-inch diameter circular cutout was machined in center of panel (See Figure 52(b)).
- (c) Externally Bonded Steel Reinforcement - A tapered 4130 steel disk having a 3 in. O.D. and 1 in. I.D. was machined and bonded to one side of the test panel by using Epon 921 adhesive and a room temperature cure. Bond line thickness was 10 mils. (See Figure 53.)



a. Control



b. Unreinforced Cutout

Figure 52. Control and Unreinforced Cutout Test Panels.

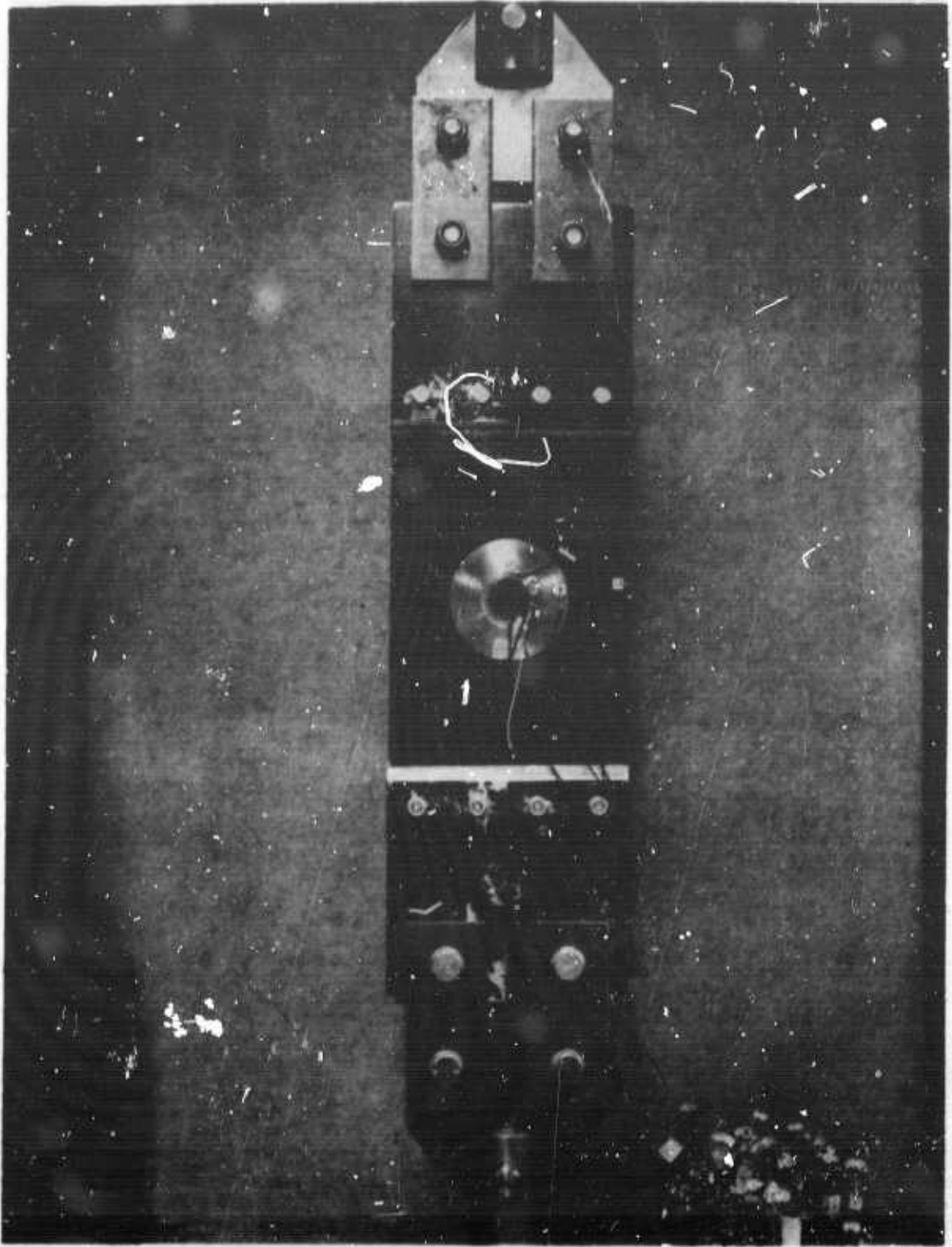


Figure 53. Externally Bonded Steel Reinforced Cutout Panel.

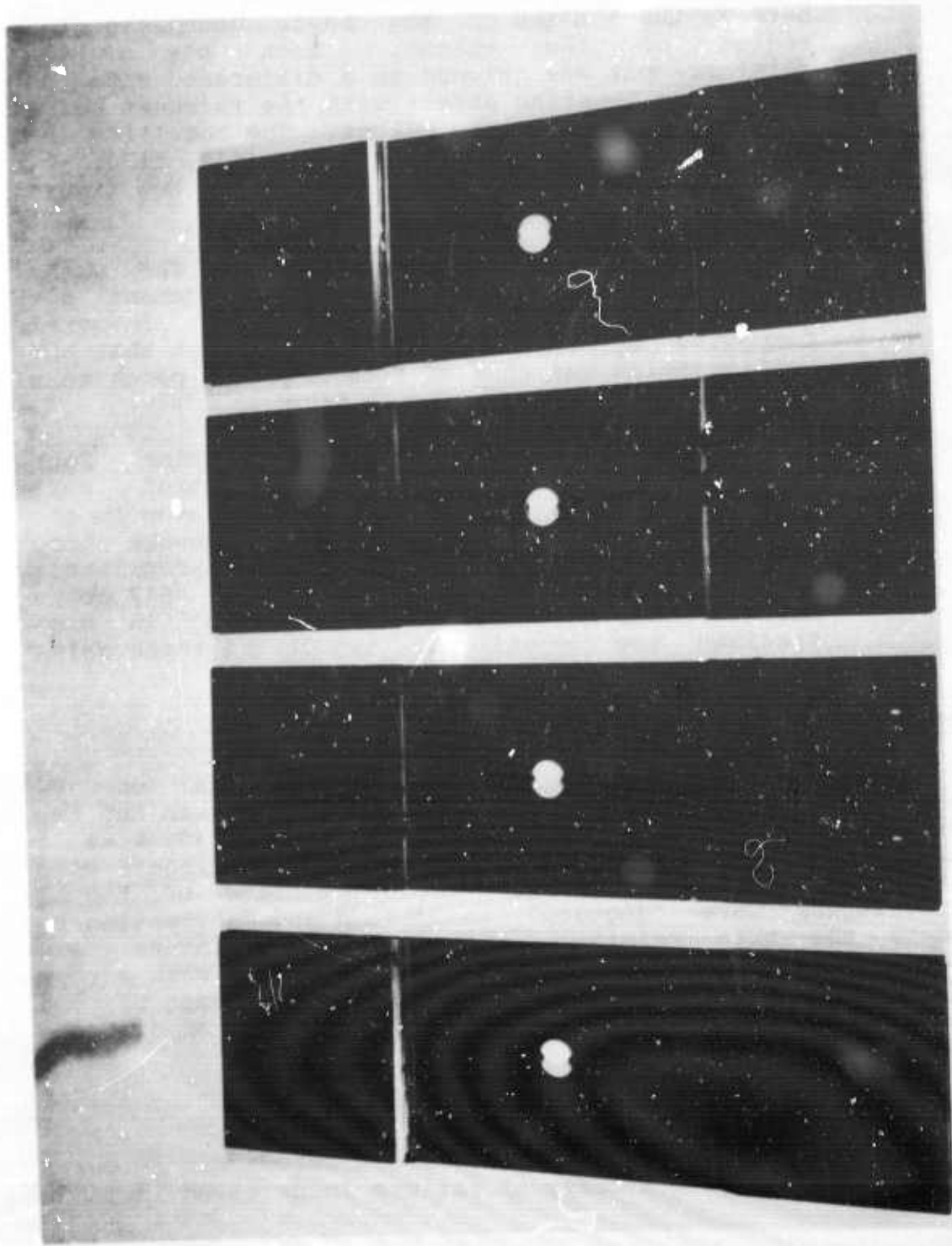
- (d) Integral Composite, Specimen (1) - Ten additional plies of graphite prepreg were interspersed between the 5 plies of the basic panel in the region of the cutout. Each ply of the reinforcement was trimmed to a different size to achieve a tapering effect with the thickest point nearest the edge of the cutout. The resulting 15-ply orientation at the cutout was ($\pm 15, \pm 30, 0, 90, 0, 90, 0, 90, 0, \mp 30, \mp 15^\circ$). See Figure 54(a).
- (e) Integral Composite Specimen (2) - The same fabrication procedure and reinforcement ply orientations were used as in the integral Composite Specimen (1) design, except that the configuration was changed from a square patch to a "butterfly" type. See Figure 54(b).
- (f) Integral Titanium and Stainless Steel Shims - Four shims of titanium and stainless steel were inserted between the basic 5-ply layup in the specimens shown in Figure 54(c and d). To ensure bond integrity, the metallic shims were appropriately cleaned and coated with a thin layer of 4617 epoxy before insertion into the laminate. In each specimen two 16-mil and two 20-mil thick shims were used.

Stiffened Compression Panel

The cutout reinforcement consisted of 3 parts: one 8-ply ($\pm 45, 0, 0, 0, 0, \mp 45^\circ$) which was bonded to the skin and two stringer cap load transfer plates of a 4-ply ($\pm 45, \mp 45$) configuration. See Figure 55. Seven hat-shaped stringers were used with a stringer spacing of 2.25 in. The legs of the 3 center stringers were "joggled" in design and fabrication to accommodate the skin reinforcement plate. Stringers and reinforcements were bonded using Epon 921 adhesive with a room temperature cure to minimize thermal stresses. The shape of the cutout was representative of an access opening in an airframe structure.

C. Test Results

Photographs of the panels after test are shown in Figures 52(a), 56 and 57 with a summary of failure loads given in Table XIX.



d. Integral
Stainless Steel

c. Integral
Titanium

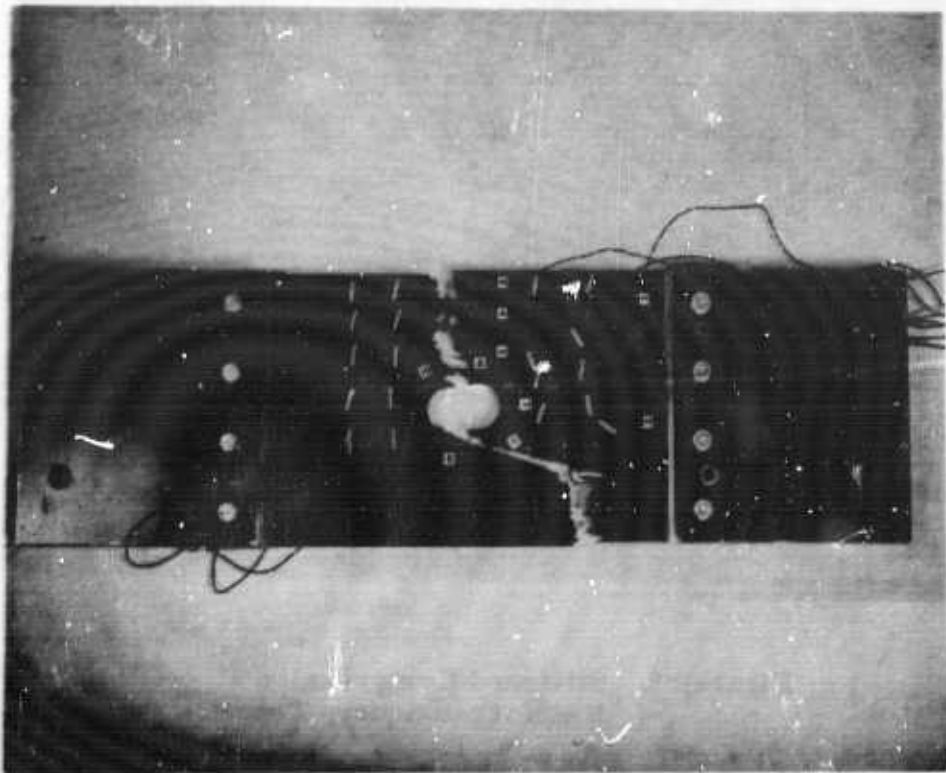
b. Integral
Composite(2)

a. Integral
Composite(1)

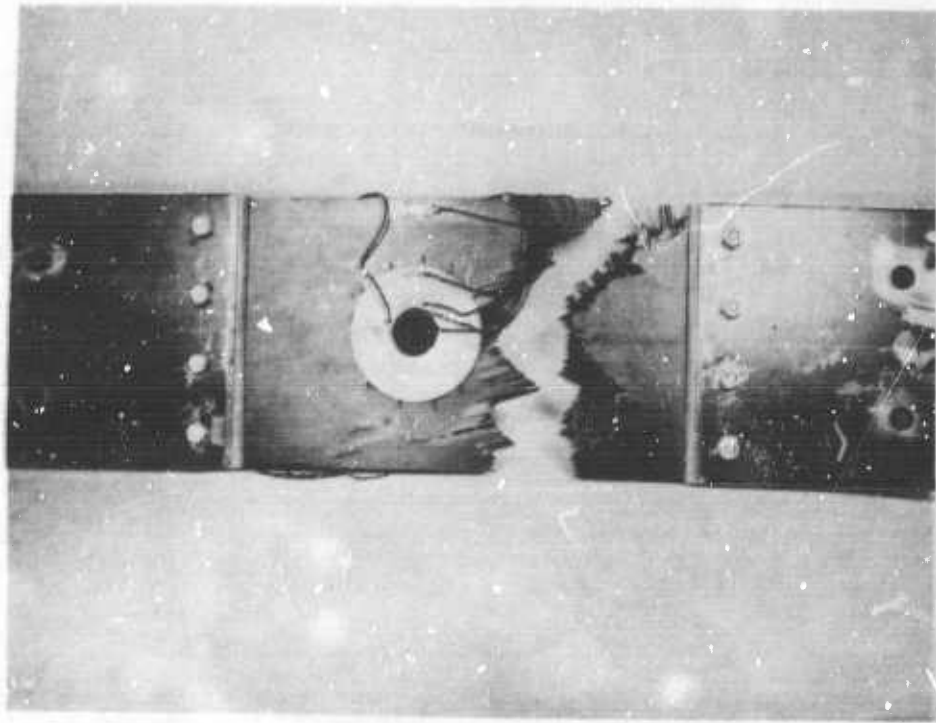
Figure 54. Reinforced Cutout Panels.



Figure 55. Stiffened Compression Panel with Reinforced Square Cutout.

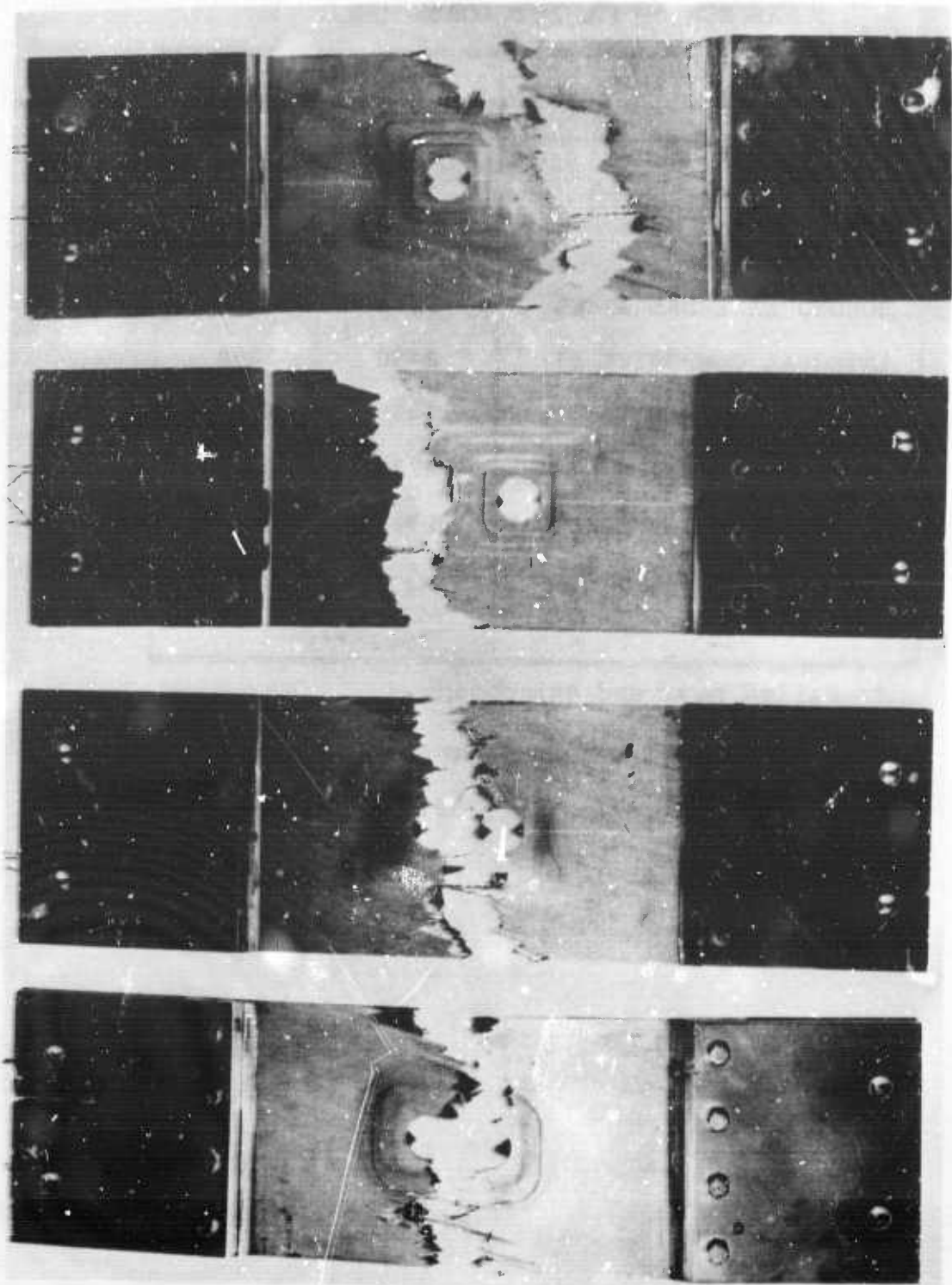


a. Unreinforced Cutout



b. Bonded External Steel

Figure 56. Cutout Panels after Test.



a. Integral Composite(1) b. Integral Composite (2) c. Integral Titanium d. Integral Stainless Steel

Figure 57. Reinforced Cutout Panels after Test.

TABLE XIX
COMPARISON OF FAILURE LOADS (LB/IN.)

Panel	Predicted	Measured
CONTROL	3240	2420*
UNREINFORCED	1350	1300
BONDED EXTERNAL STEEL	2200	2250
INTEGRAL COMPOSITE (1)	2480	2260
INTEGRAL COMPOSITE (2)	2480	2200
INTEGRAL TITANIUM	2920	2020
INTEGRAL STAINLESS STEEL	2760	1990
STIFFENED COMPRESSION	1430**	1610
	3900***	

* Failed near end attachment.

** Southwell prediction for critical buckling load.

*** Compression strength prediction.

With reference to control panel failure at 75% of predicted strength as shown in Table XIX, it must be noted that failure did not occur in the gage section; see Figure 52(a). Analysis had shown that a complex biaxial stress state exists in the corner of the panel near the end attachments as a result of clamped boundary conditions. The analysis in this region indicated that failure should initiate at \sim 83% of ultimate laminate tensile strength. This analytical value is in reasonable agreement with the experimental value of 75% considering, as well, that nominal material properties were used previously.

Considerable strain gage instrumentation was used on the control panel as seen in Figure 52(a). All load-strain curves were linear to failure and showed excellent strain uniformity across the panel midsection with negligible bending. Predicted and measured results of the control panel test are summarized in Table XX.

TABLE XX

CONTROL PANEL TEST RESULTS
 "THORNEL" 50S/4617, (± 15 , 90, ∓ 15)

Property	Predicted	Measured
X T (ϵ) 1 ult	95.5	69.5*
(μ in./in.)	4100	2970
E 1	23.2	23.4
ν_{12}	0.259	0.222
V F	Same	57.4
V V	-	0

*Failure near end attachment

Table XXI summarizes predicted unidirectional data for the "Thornel" 50S/4617 system and complete properties for the test laminate. The unidirectional properties have been corrected as noted based on tests of a 5-ply unidirectional panel. The latter data are presented in Table XXII .

The unreinforced cutout panel failed at 54% of the load that the control panel carried as may be seen from Table XIX. Although failure was catastrophic and sudden, it was believed that tensile failure first took place at the left side of the hole followed by crack propagation out toward the free left edge. See Figure 56(a). Eccentric loading and bending would then have resulted in failure at the right side of the hole which propagated upward and to the right. Almost all strain gages were linear with increasing load up to 1000 lb/in. Above this load, nonlinearities were pronounced, especially in the vicinity of the hole. Typical strain responses are shown in Figure 58. Gage 9 shown therein measured the highest strain, $3700 \mu \text{ in./in.}$

It can also be seen from Table XIX that the reinforced cutout panels failed at no less than 82% and as high as 93% of the load carried by the control panel. Of these the highest failure load was achieved with the composite (1) design. As shown in Figure 57 failures occurred at the ends of the metallic reinforced specimens and were $\sim 30\%$ less than predicted values. These failure modes were attributed to the fact that the metal shims, although 0.016 in. thick, ended abruptly and caused local stress concentrations which initiated failure. With the graphite reinforced panels, this problem was minimized by curing the reinforcements and panels simultaneously, thus obtaining smoother transitions. Failures of the graphite reinforced panels occurred in the predicted regions.

A comparative failure load and reinforcement weight analysis is shown in Figure 59. The failure loads have been normalized to that of the control panel and the normalized weights were computed as total reinforcement weight divided by weight of material removed by the cutout. This comparison shows that a considerable weight savings can be achieved while maintaining load-carrying capability by the use of graphite reinforcements in contrast to metal reinforcements.

A curious anomaly occurred in each of the flat panel tension tests. Either one or both of the free edges of the panel delaminated as shown in Figure 60 before panel failure. The delamination shown extended to a depth of ~ 0.5 in. into each of the panels and was observed during test at a nominal stress of 43,000 psi or 62% of ultimate. Visual inspection revealed a

TABLE XXI
PREDICTED "THORNEL" 50S/4617 PROPERTIES

Property	Unidirectional Laminate	Test Laminate 5 ($\pm 15, 90, \mp 15^\circ$)
V_F (%)	Same ←	57
t (in.)	-	0.034
E_1 } E_2 } G_{12} } ν_{12} ν_{21} } (10 ⁶ psi)	33.4 (1) 1.0 0.5 0.304 0.012	23.2 7.5 2.1 0.259 0.084
X_T } X_C } Y_T } Y_C } T } (ksi)	128 (2) 100 2.5 28.0 6.3	95.5 75.2 25.6 22.5 21.2

- (1) $E_1 = 1.13 \times$ rule of mixtures value }
 (2) $X_T = 0.895 \times$ rule of mixtures value } See Table XXII

TABLE XXII
PREDICTED AND MEASURED "THORNEL" 50S/4617 UNIDIRECTIONAL PROPERTIES

Property	Predicted ⁽¹⁾	Measured
X_T (ksi)	161.0	144.0
E_1 (10 ⁶ psi)	32.0	36.1
V_F (%)	Same ←	65
V_V (%)	-	0.5

- (1) Based on rule of mixtures with $V_F = 65\%$, $\sigma_{\text{Fiber}} = 245$ ksi (yarn strength) and $E_F = 48 \times 10^6$ psi per Union Carbide data this lot.

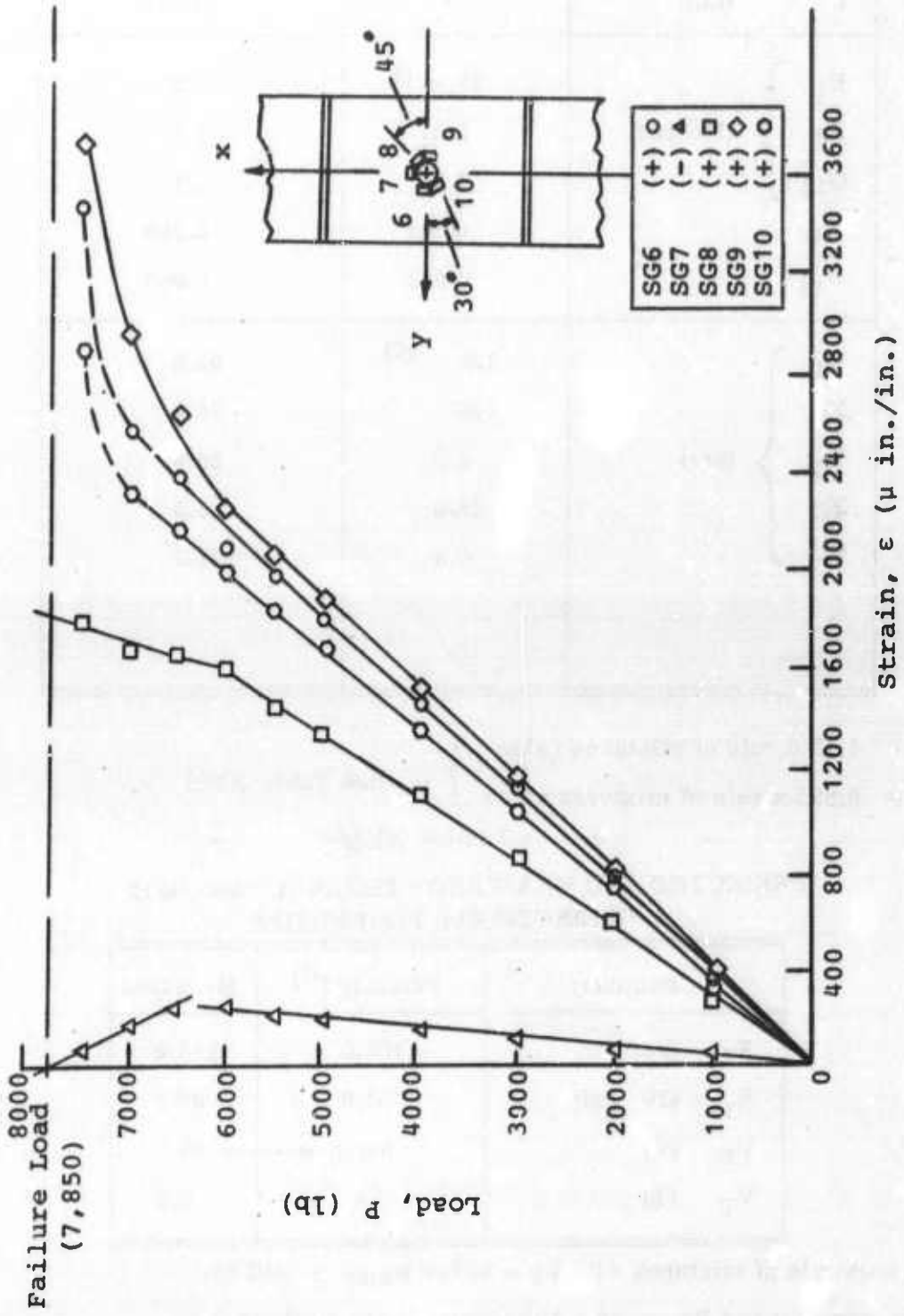


Figure 58. Typical Strain Responses from Cutout Panel Test

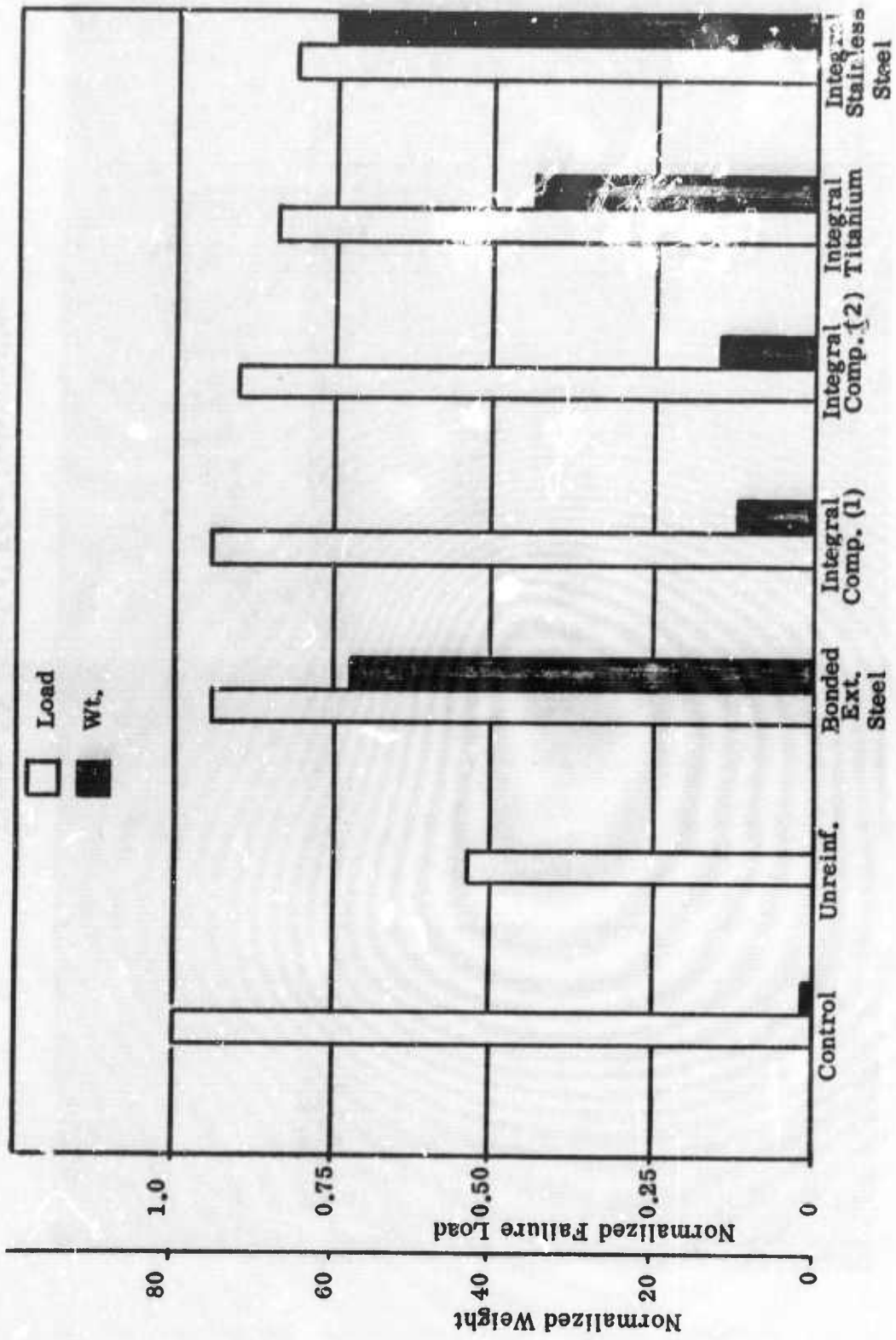


Figure 59. Comparison of Failure Loads and Reinforcement Weights for "Thornel" 50S/4617 Specimens

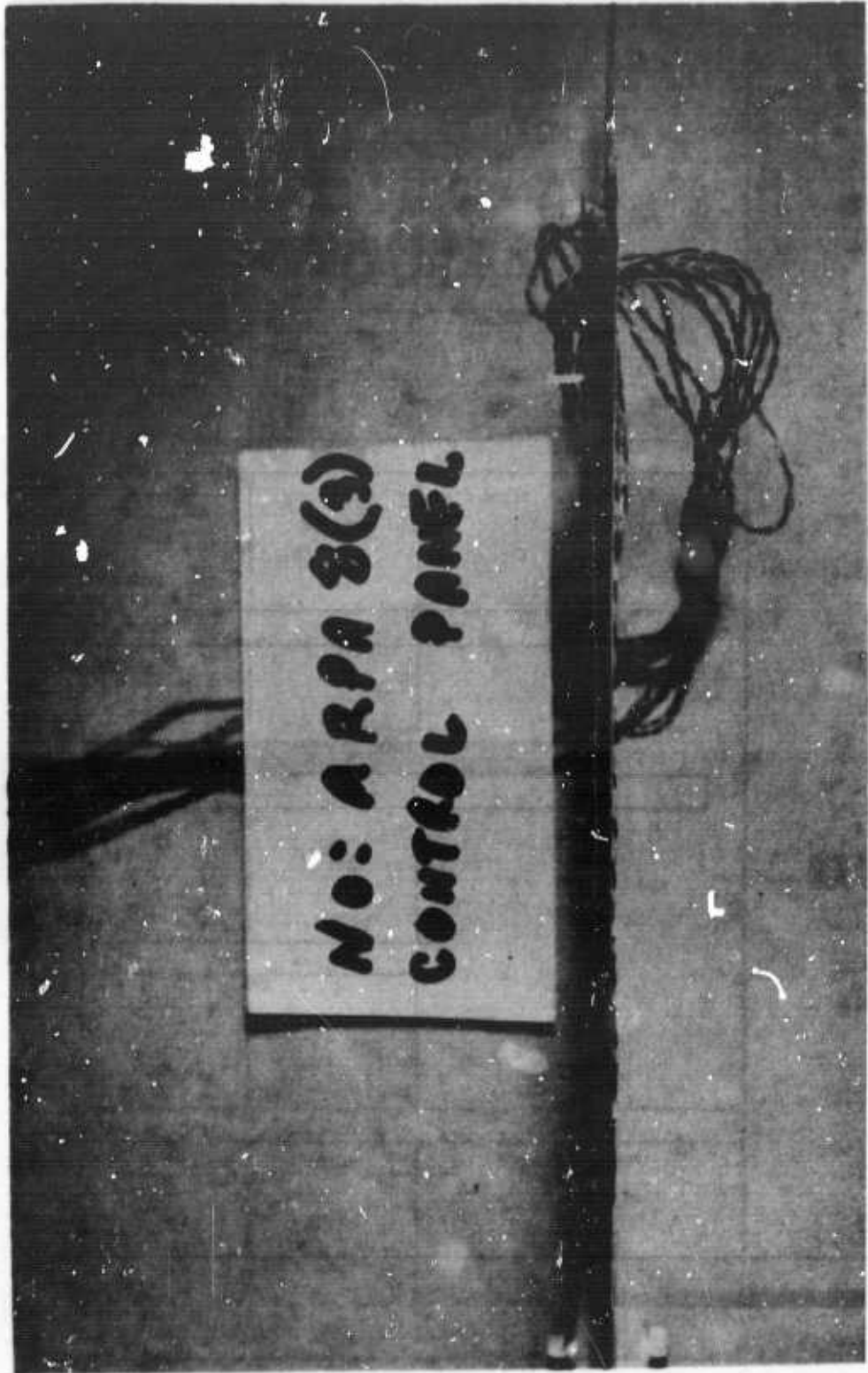


Figure 60. Typical Edge Delamination

failure approximately in the center of the 90° ply and normal to the plates. Strain gage data did not show evidence of this delamination. Due to the antisymmetry of the $\pm 15^\circ$ plies, the panel edges were observed to curl after test as shown in Figure 60.

Ends of the compression panel were potted to simulate clamped end conditions during test. The failure load was 1610 lb/in. as compared to 3900 lb/in. predicted for a pure compressive failure. A Southwell plot of the panel's midpoint transverse deflection indicated the panel to be buckling critical at a load of 1430 lb/in. This load was reasonably close to the measured failure load. Failure did not occur in the reinforced region, rather it was a combination shear/compressive type traversing across the panel approximately 1 in. above the reinforced region.

D. Test-Theory Comparisons

A discrete element analysis was performed for each of the unstiffened panels tested. Due to symmetry of the plate and loading, only one quadrant of the plate was analyzed, and symmetric boundary conditions were imposed along two axes.

The plate was idealized as a two-dimensional (plane stress) assemblage with 39 quadrilateral plate elements. To simulate uniaxial tensile test conditions, a uniform displacement (u_0) was imposed in the pulled direction while restraining displacements in the transverse direction.

A margin of safety analysis was performed for each panel, and the predicted ultimate loads were calculated. A comparison of the predicted and measured failure loads was given in Table XIX showing fair-to-good agreements. Figure 61 shows a comparison of predicted and measured strain response for the unreinforced cutout panel showing excellent agreement between discrete element and measured strains. Similar agreements were obtained for the other panels. Analytically predicted stress and strain concentrations at the edge of an unreinforced circular cutout on an infinite plate are shown in Figure 62. These concentrations are equal with a value of 4.75 at $\theta = 90^\circ$ and 0.02 at $\theta = 32^\circ$ for the test panel orthotropy ratio ($E_1/E_2 = 3.09$). Elsewhere around the hole, stress and strain "K" factors are unequal in contrast to those for the isotropic material.

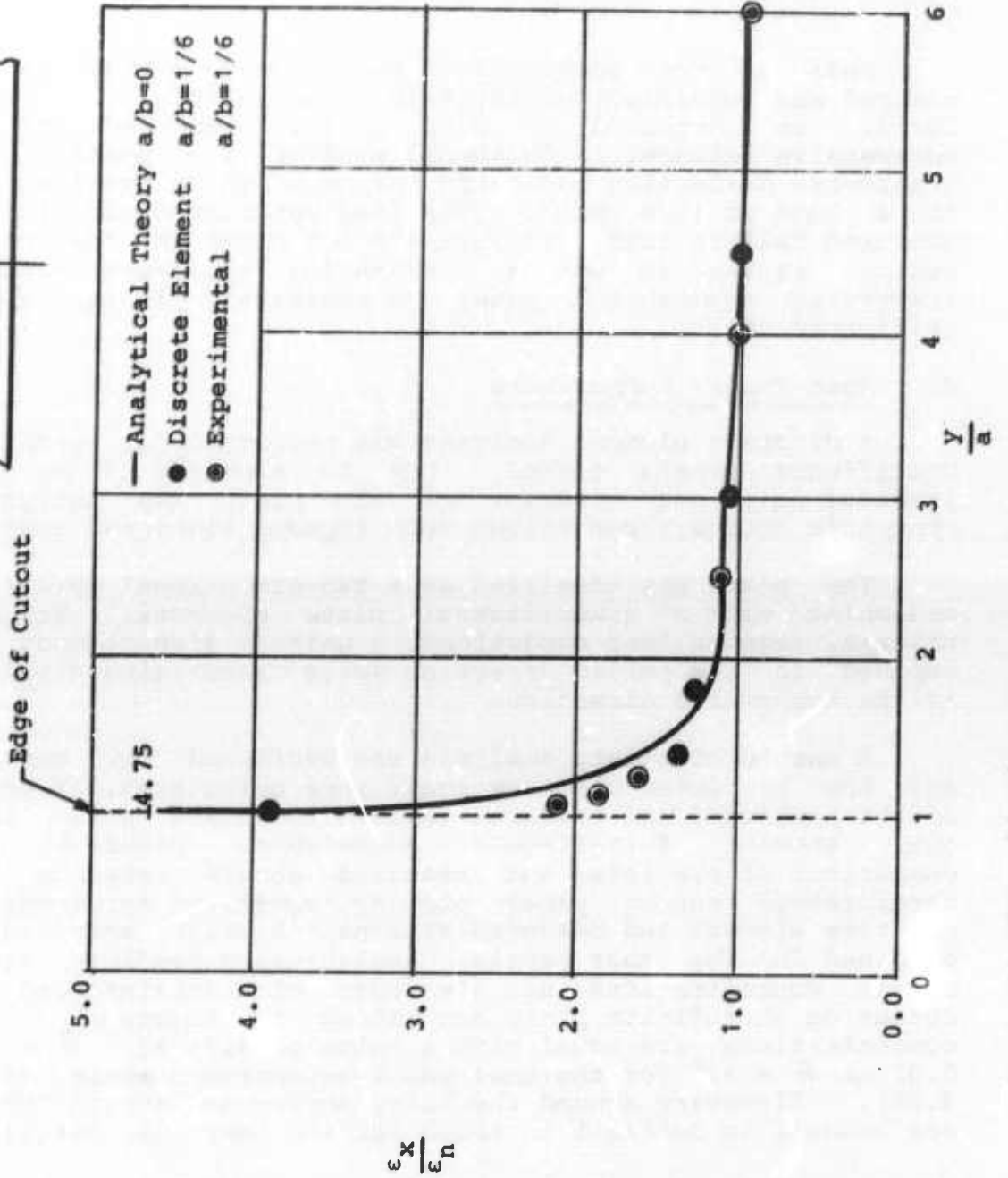
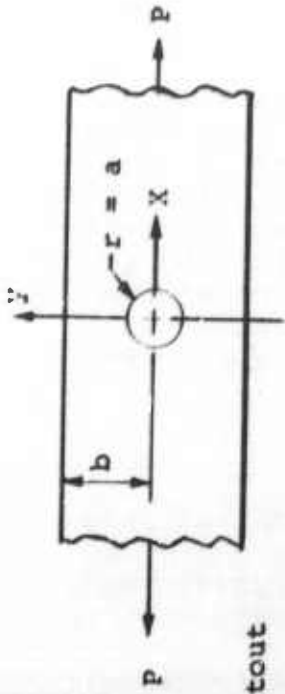


Figure 61. Normalized Strain ϵ_x/ϵ_n vs. y/a for Unreinforced Cutout Panel

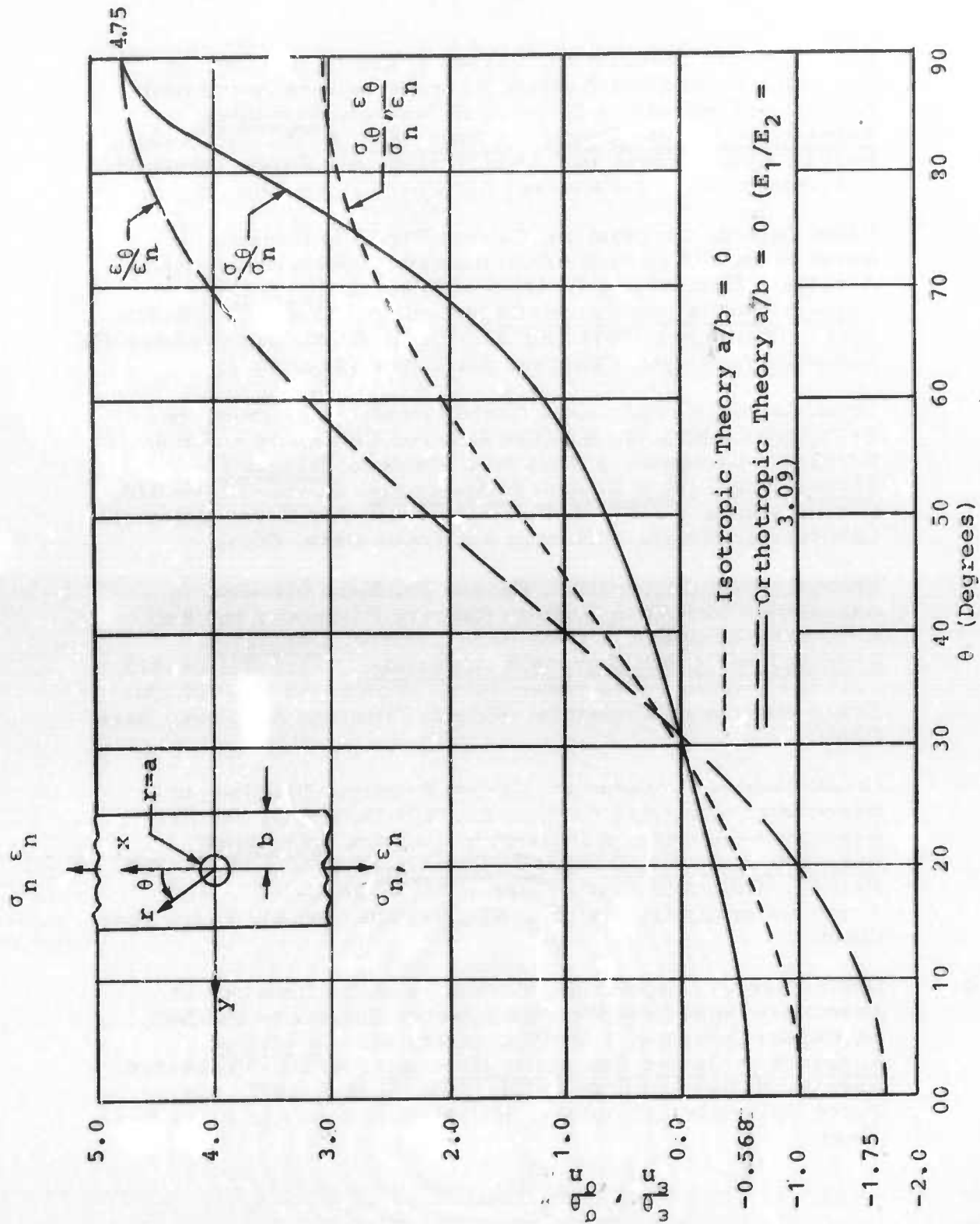


Figure 62. Normalized Tangential Stress and Strain Vs. Angle at $r = a$

REFERENCES

1. Union Carbide Corporation, Carbon Products Division, in Association with Case Western Reserve University and Bell Aerospace Company, a Division of Textron, Integrated Research on Carbon Composite Materials, AFML-TR-66-310, Part I (October 1966) (AF 33(615)-3110, Air Force Materials Laboratory, Wright-Patterson Air Force Base, Ohio).
2. Union Carbide Corporation, Carbon Products Division, in Association with Case Western Reserve University and Bell Aerospace Company, a Division of Textron, Integrated Research on Carbon Composite Materials, AFML-TR-66-310, Part II (December 1967) (AF 33(615)-3110, Air Force Materials Laboratory, Wright-Patterson Air Force Base, Ohio).
3. Union Carbide Corporation, Carbon Products Division, in Association with Case Western Reserve University and Bell Aerospace Company, a Division of Textron, Integrated Research on Carbon Composite Materials, AFML-TR-66-310, Part III (January 1969) (AF 33(615)-3110, Air Force Materials Laboratory, Wright-Patterson Air Force Base, Ohio).
4. Union Carbide Corporation, Carbon Products Division, in Association with Case Western Reserve University and Bell Aerospace Company, a Division of Textron, Integrated Research on Carbon Composite Materials, AFML-TR-66-310, Part IV, Volume I (September 1969) (F33615-68-C-1077, Air Force Materials Laboratory, Wright-Patterson Air Force Base, Ohio).
5. Union Carbide Corporation, Carbon Products Division, in Association with Case Western Reserve University and Bell Aerospace Company, a Division of Textron, Integrated Research on Carbon Composite Materials, AFML-TR-66-310, Part IV, Volume II (April 1970) (F33615-68-C-1077, Air Force Materials Laboratory, Wright-Patterson Air Force Base, Ohio).
6. Union Carbide Corporation, Carbon Products Division, in Association with Case Western Reserve University and Bell Aerospace Company, a Division of Textron, Integrated Research on Carbon Composite Materials, AFML TR-66-310, Part IV, Volume III (July 1970) (F33615-68-C-1077, Air Force Materials Laboratory, Wright-Patterson Air Force Base, Ohio).

7. Schmit, L. A., "Structural Design by Systematic Synthesis," Proc. 2nd Natl. Conf. on Elec. Computation, Str. Div., ASCE, 1960, pp. 105-132.
8. Schmit, L. A., Kicher, T. P., and Morrow, W. M., "Structural Synthesis Capability for Integrally Stiffened Waffle Plates," AIAA Journal, Vol. 1, No. 12, Dec. 1963.
9. Kicher, T. P., "Structural Synthesis of Integrally Stiffened Cylinders," J. of Spacecraft and Rockets, Vol. 5, No. 1, Jan. 1968.
10. Schmit, L. A., Morrow, W. M., and Kicher, T. P., "Structural Synthesis Capability for Integrally Stiffened Cylindrical Shell Shells," AIAA/ASME 9th Structures, Str. Dynamics and Material Conf., Palm Springs, Calif., April 1968.
11. Timoshenko, S. P. and Gere, J. M., Theory of Elastic Stability, McGraw-Hill Book Co., Inc., New York, 1961.
12. Donnell, L. H., "Stability of Thin-Walled Tubes under Torsion," NACA Rept. 479, pp. 95-115 (1933).
13. Chamis, C. C., "Micro and Structural Mechanics and Structural Synthesis of Multilayered Filamentary Composite Panels," Case Western Reserve University, SMSMD Report 9 under Contract No. AF 33(615)-3110, Sept. 1967.
14. Chao, T. L., "Minimum Weight Design of Stiffened Fiber Composite Cylinders," Ph.D. Thesis, Case Western Reserve University, September 1969.
15. Bogner, F., Fox, R., and Schmit, L., "A Cylindrical Shell Discrete Element," AIAA Journal, Vol. 5, No. 4, 1967.
16. Sendekyj, G. P., "Longitudinal Shear Modulus of Filamentary Composite Containing Curvilinear Fibers," Fibre Science and Technology, Vol. 2, (1970), pp. 211-222.
17. Sendekyj, G. P., "Multiple Circular Inclusion Problems in Longitudinal Shear Deformation," submitted for publication to Elasticity.
18. Hill, R., "Elastic Properties of Reinforced Solids: Some Theoretical Principles," J. Mech. Phys. Solids, Vol. II (1963), p. 357.

19. Adams, D. F. and Doner, D. R., "Longitudinal Shear Loading of a Unidirectional Composite," Journal of Composite Materials, Vol. 1 (1967), p. 30.
20. Chen, C. H., "Fiber-Reinforced Composites under Longitudinal Shear Loading," Journal of Applied Mechanics, Vol. 37 (1970), pp. 199-201.
21. Sendekyj, G. P., "Elastic Inclusion Problems in Plane Elastostatics," International Journal of Solids and Structures, in press.
22. Reissner, E., "On the Variation Theorem for Finite Elastic Deformations," Journal of Mathematics and Physics, Vol. 32, pp. 129-135, 1953.
23. Lekhnitskii, S. G., Theory of Elasticity of an Anisotropic Elastic Body, translated by Fern, P., (Holden-Day, Inc. 1963).
24. Washizu, K., Variational Methods in Elasticity and Plasticity, (Pergamon Press Ltd. 1968).
25. Minich, M. D., "Discrete Element Analysis by Combined Method Formulation," Ph.D. Thesis, SMSMD Case Western Reserve University, Cleveland, Ohio, 1967.
26. SMSMD, Case Western Reserve University, Development in Discrete Element Finite Deflection Structural Analysis by Function Minimization, AFFDL-TR-68-126, September 1968.
27. Bogner, F. K., "Finite Deflection, Discrete Element Analysis of Shells," Ph.D. Thesis, SMSMD Case Institute of Technology, Cleveland, Ohio, 1967.
28. Melosh, R. J. and Bamford, R. M., "Efficient Solution of Load Deflection Equations," Journal of the Structural Division, ASCE, Vol. 95, No. ST4, April, 1969, pp. 661-676.
29. Koeneman, J. B., "Interface Failure of Composite Materials," Report No. 38, Division of Solid Mechanics, Structures, and Mechanical Design, School of Engineering, Case Western Reserve University, Cleveland, Ohio, 1969.
30. Brown, W. F., Jr. and Strawley, J. E., "Plane Strain Crack Toughness Testing of High Strength Metallic Materials," ASTM Special Technical Publication No. 410, 1966.

31. Sih, G. C., Paris, P. C., and Irwin, G. R., "On Cracks in Rectilinearly Anisotropic Bodies," International Journal of Fracture Mechanics, Vol. 1, No. 3, 1965, pp. 189-203.
32. Wu, E. M., "Application of Fracture Mechanics to Orthotropic Plates," T & AM Report No. 248, University of Illinois, June, 1963.
33. Gross, B. and Strawley, J. E., "Stress Intensity Factors for Single-Edge-Notch Specimens in Bending or Combined Bending and Tension by Boundary Collocation of a Stress Function," Technical Note D-2603 NASA, January 1965.
34. Doner, D. R. and Novak, R. C., "Structural Behavior of Laminated Graphite Filament Composites" in 24th Annual Technical Conference, 1969 Reinforced Plastics/Composites Division, The Society of the Plastics Industry, Inc.
35. Rao, P. N. and Hofer, K. E., "An Investigation of Fatigue Behavior of Reinforced Plastics for Primary Aircraft Structures." IIT Research Institute. Contract N00019-69-C-0282, (Final Report, Jan. 1-Dec. 31, 1969), (IITRI-D6010-FR).
36. Zirbrick, J. R., Development of Nondestructive Tests for Predicting Elastic Properties and Component Volume Fractions in Reinforced Plastic Composite Materials, AFML-TR-68-233, AVCO Corporation, Space Systems Division.
37. Elkin, R. A., Fust, G., and Hanley, D. P., "Test Methods for Characterization of Graphite Fiber/Resin Matrix Composites," ASTM Conference on Composite Materials: Testing and Design, New Orleans, Louisiana, February 11-13, 1969.

UNCLASSIFIED

Security Classification

DOCUMENT CONTROL DATA - R & D

(Security classification of title, body of abstract and indexing annotation must be entered when the overall report is classified)

1. ORIGINATING ACTIVITY (Corporate author) Union Carbide Corporation Case Western Reserve University Bell Aerospace Company		2a. REPORT SECURITY CLASSIFICATION Unclassified	
		2b. GROUP	
3. REPORT TITLE INTEGRATED RESEARCH ON CARBON COMPOSITE MATERIALS, Part V Volume II - Structural Mechanics			
4. DESCRIPTIVE NOTES (Type of report and, inclusive dates) Summary Technical Report July 1969 to September 1970			
5. AUTHOR(S) (First name, middle initial, last name) Union Carbide Corporation, Carbon Products Division, in Association with Case Western Reserve University and Bell Aerospace Company, a Division of Textron			
6. REPORT DATE January 1971	7a. TOTAL NO. OF PAGES 141	7b. NO. OF REFS 37	
8a. CONTRACT OR GRANT NO. F33615-68-C-1077	9a. ORIGINATOR'S REPORT NUMBER(S)		
8b. PROJECT NO. ARPA Order No. 719 Program Code 7D10	9b. OTHER REPORT NO(S) (Any other numbers that may be assigned this report) AFML-TR-66-310, Part V. Volume II		
10. DISTRIBUTION STATEMENT: This document is subject to special export controls and each transmittal to foreign governments or foreign nationals may be made only with prior approval of the Nonmetallic Materials Division, AFML/LN, Air Force Materials Laboratory, Wright-Patterson AFB, Ohio 45433.			
11. SUPPLEMENTARY NOTES		12. SPONSORING MILITARY ACTIVITY Air Force Materials Laboratory Wright-Patterson AFB, Ohio	
13. ABSTRACT The work presented in Volume II is concerned with the structural mechanics and synthesis of graphite-fiber reinforced composite materials. Optimization studies (minimum weight design) of stiffened cylinders similar to the fuselage component were carried out by two different techniques. The behavior of composite structural elements was investigated in plate-buckling and post-buckling studies, buckling of stiffened plates with cut-outs, and application of shell theory to anisotropic cylinders. Micromechanics studies of fibrous composites included development of a photoelastic technique for analyzing frozen stresses, a discrete element microstress analysis of uni- directional fiber composites, an application of the theory of physically non- linear elastic solids to composite materials, and an investigation of the multiple circular inclusion problem in plane elastostatics. Failure of composite structural elements was investigated through studies of the failure mechanism for off-axis composites, the fracture toughness of composites, the effect of fatigue and sustained loads of cross-plyed composites, the notch sensitivity of cross-plyed composites, and the effect of a variety of known intentionally interjected defects on the fracture strength. Further studies were concerned with multiaxial stress testing of composite cylinders. The effects of circular and square cut-outs in flat panels and in a stiffened panel, and methods of reinforcement of cut-outs were investigated and correlated with predictions based on discrete element analysis. ()			

